Politecnico di Milano

School of Industrial and Information Engineering

Department of Electronics, Information and Bioengineering

A thesis submitted in fulfillment of the requirments for the degree of Master of Science in Biomedical Engineering

Blood flow in cerebral aneurysms: comparison among 4D flow guided-CFD, FSI and 3D variational data assimilation

Supervisor:
Alberto Redaelli, PhD
Cosupervisors:
Alessandro Caimi, PhD
Simone Saitta, MSc

Author:
Riccardo Munafò
ID: 920837

Academic Year 2020/2021

Acknowledgments

Vorrei anzitutto ringraziare il Prof. Alberto Redaelli per avermi dato l'oppurtunità di poter svolgere la tesi presso il laboratorio di Biomecanica Computazionale del Politecnico di Milano. Ringrazio Simone per avermi proposto l'argomento della tesi e per avermi seguito durante tutto il mio percorso. Durante questi mesi ho potuto apprendere grazie a lui nuove conoscenze tecniche che ora fanno parte del mio background e mi aiuteranno nel proseguimento della mia carriera. Ringrazio Alessandro per il tempo da lui dedicato a seguire tutti i tesisti e per i preziosi consigli durante i primi mesi. Infine, vorrei ringraziare la mia famiglia e miei genitori per avermi dato l'opportunità di poter studiare lontano da casa e per avermi sempre sostenuto durante tutti questi cinque anni.

Contents

Sommario

Introduzione

Gli aneurismi cerebrali sono patologie cerebrovascolari in cui, a causa di un indebolimento delle fibre muscolari della parete, il vaso sanguigno si dilata o protrude verso l'esterno [1]. La rottura di un aneurisma cerebrale determina un'emorragia subaracnoidea, un'emergenza neurovascolare con elevata mortalità [2]. La maggior parte degli aneurismi cerebrali non causa nessun sintomo e solitamente è scoperto incidentalmente. Per questo motivo predire la rottura di un aneurisma è di fondamentale importanza per guidare il medico specialista nel determinare il miglior percorso per il trattamento dell'aneurisma.

Diversi fattori di rischio per la rottura degli aneurismi sono stati definiti e sono attualmente usati in clinica. Età e ipertensione sembrano avere un grande impatto nella rottura degli aneurismi, così come la loro dimensione, posizione e morfologia [2, 3]. Specifici parametri morfologici sono stati definiti per classificare gli aneurismi intracranici, tra i quali aspect ratio (AR), size ratio (SR), flow angle (FA) e height-width ratio (H/W), e alcuni di questi sono stati esplicitamente associati con la rottura degli aneurismi [4]. La diagnosi e il monitoraggio degli aneurismi cerebrali fanno affidamento sulla valutazione tramite immagini cliniche, quali la fluoroscopia (DSA), la tomografia computerizzata (CTA) e la risonanza magnetica (MRA) [3]. La diagnosi basata su immagini è fondamentale per la stratificazione del rischio di rottura degli aneurismi cerebrali, permettendo di valutarne l'evoluzione morfologica. La risonanza magnetica 4D flow (abbreviato 4D flow), è una tecnica di imaging innovativa e non invasiva con cui è possibile misurare il flusso sanguigno e valutare l'emodinamica [5]. Il 4D flow è già stato applicato efficacemente per la valutazione dell'emodinamica in diversi distretti anatomici [5], tra cui anche gli aneurismi cerebrali [6, 7, 8]. Questo tipo di analisi permette di associare la morfologia degli aneurismi con i parametri emodinamici, arricchendo così la valutazione del rischio di rottura per gli aneurismi cerebrali. Tuttavia, la scarsa risoluzione spaziale e temporale limitano l'applicabilità del 4D flow, soprattutto nel calcolo dei wall shear stress

(WSS), i quali si ritiene abbiano un ruolo importante nello sviluppo e nella rottura degli aneurismi cerebrali.

I modelli numerici permettono di simulare il flusso sanguigno, fornendo un'esauriente valutazione emodinamica in diversi distretti cardiaci, compresi gli aneurismi cerebrali [9, 10]. Le simulazioni CFD permettono di analizzare, in domini rigidi, l'emodinamica all'interno degli aneurismi in maniera quantitativa e qualitativa. Aneurismi cerebrali con un alto AR ($>$ 2.2) sono stati associati, mediante analisi CFD, a flussi a bassa velocità, bassi TAWSS, bassi WSS al picco sistolico e alti OSI [11]. Aneurismi con un alto SR sono stati, invece, associati a flussi secondari e instabili in [12]. In due studi correlati, Cerebral et al. [13, 14], hanno dimostrato mediante simulazioni CFD pazienti-specifiche che flussi instabili, zone ridotte di impatto tra sangue e parete, e getti stretti in ingresso all'aneurisma sono fattori emodinamici discriminanti per la rottura degli aneurismi cerebrali. Nella stima dei WSS le analisi CFD sono attualmente lo strumento di riferimento. In particolare, Meng et al. hanno proposto che alti WSS hanno un ruolo rilevante nella iniziazione e crescita degli aneurismi cerebrali, mentre bassi valori di WSS sono determinanti nella loro rottura. Sebbene le analisi CFD hanno dimostrato di essere un valido strumento per la valutazione emodinamica, l'ipotesi di pareti rigide su cui si basano può limitare l'affidabilità di questo approccio. Le simulazioni fluido-struttura (FSI) tengono conto dell'interazione tra sangue e parete, tuttavia solo pochi studi di questo tipo sono stati affrontati per valutare l'emodinamica all'interno di modelli di aneurismi cerebrali pazienti-specifici [15, 16, 17, 18]. In generale, in questi studi è stato notato che le analisi CFD sovrastimassero i WSS rispetto alle analisi FSI, anche se la velocità del sangue non sembrava alterata [15]. Gli spostamenti della parete del vaso sono stati ritenuti non trascurabili per l'aneurisma, soprattutto assumendo un assottigliamento patologico di quest'ultimo, in quanto determinava una riduzione dei WSS [17] e una migliore correlazione tra la distribuzione degli stress e le zone di rottura della parete [18]. Attualmente, i modelli CFD e FSI sono i metodi di riferimento per la valutazione emodinamica dei principali distretti cardiovascolari. Tuttavia, l'affidabilità di questi metodi dipende da scelte modellistiche, quali per esempio i modelli costitutivi del sangue o le condizioni al contorno, che possono ostacolare la loro applicazione in clinica. Geometrie pazienti-specifiche e condizioni al contorno possono essere estratte da immagini cliniche con un accettabile livello di affidabilità. Per esempio, il 4D flow consente di acquisire affidabili misure del flusso sanguigno da applicare come condizioni al contorno per i modelli numerici (4D flow guided-numerical models). In [19, 20], un buon accordo è stato trovato tra le misure fornite dal 4D flow del flusso sanguigno e la

sua ricostruzione tramite 4D flow guided-CFD, soprattutto durante la fase sistolica del ciclo cardiaco. Tuttavia, come mostrato in [21], il 4D flow sottostima i WSS rispetto alla CFD anche se la relativa distribuzione è stata trovata consistente tra i due metodi. Le differenze tra queste due metodologie sono principalmente dovute alle sopracitate limitazione del 4D flow [22], ma anche al movimento del vaso sanguigno di cui le misure tengono conto [23]. Una promettente soluzione potrebbe essere quindi incorporare i dati di velocità estratti dal 4D flow nei modelli numerici, tramite la data assimilation (DA). La DA è un approccio matematico, già utilizzato nel campo delle previsioni metereologiche [24], che mira a combinare i risultati ottenuti tramite i modelli numerici con i dati delle misurazioni. In emodinamica, i dati estratti dal 4D flow possono quindi essere incorporati nelle simulazioni numeriche migliorando l'accuratezza e la correttezza fisica delle misure di velocità con la DA. Una delle più utilizzate strategie per la DA è la Variational DA (abbreviata Var, o nella sua specifica implementazione 3D, 3DVar). In Var la DA è formulata come un problema di ottimizzazione, vincolato con una equazione differenziale alle derivate parziali (l'equazione di Navier-Stokes per l'emodinamica), per l'identificazione di una variabile di controllo $\mathbf{c}$, che minimizzi un funzionale dipendente dalla differenza fra la velocità misurate $\mathbf{u}_m$ e la velocità stimata $\mathbf{u}$.

$$\begin{aligned} \min_{\mathbf{c}} J(\mathbf{u}, \mathbf{c}) &= dist(f(\mathbf{u}), \mathbf{u}_{\mathrm{m}}) + R(\mathbf{c}) \\ \text{s.t.} \qquad & F(\mathbf{u}, \mathbf{c}) = 0 \end{aligned} \tag{1}$$

L'efficacia della Var in emodinamica è stata studiata in [25, 26, 27] da Elia et al. valutandone l'accuratezza nella ricostruzione del flusso sanguigno e nel calcolo dei WSS da misure sintetiche in modelli vascolari idealizzati 2D [25, 26] e 3D [27]. In [28] la 3DVar è stata applicata per la prima volta su un modello reale di un aneurisma cerebrale sacciforme per ricostruire ottimali condizioni al contorno in ingresso e in uscita ma assumendo condizioni stazionarie di flusso e usando dati sintetici. In [29] Koltukluoğlu et al., hanno proposto una formulazione 3DVar assimilando dati di 4D flow acquisiti sulla riproduzione in vetro di una aorta e assumendo condizioni stazionarie del flusso sanguigno. I risultati ottenuti hanno rivelato una migliore consistenza con le misure estratte dal 4D flow rispetto a una simulazione CFD. In [30], per la prima volta, sono state considerate condizioni di flusso transitorie in una formulazione 3DVar per la ricostruzione del flusso sanguigno in un modello di aneurisma cerebrale canino. La soluzione assimilata ha mostrato una migliore somiglianza con le misure estratte dal 4D flow rispetto a una simulazione CFD ad alta risoluzione spaziale eseguita sul medesimo modello. In conclusione, la DA è un promettente approccio per combinare i modelli numerici con il

4D flow, aumentando la risoluzione e l'accuratezza delle misure, con un importante risvolto nel migliorare la valutazione del rischio di rottura degli aneurismi intracranici. Questo studio presenta una formulazione innovativa della 3DVar per ricostruire le condizioni di flusso in aneurismi cerebrali a partire da dati 4D flow.

Materiali e metodi

Un modello di aneurisma cerebrale sacciforme è stato ricostruito da una acquisizione 4D MRI. La geometria estratta è stata processata ottenendo un modello finale contenente un aneurisma posizionato in prossimità della biforcazione tra la carotide interna e la giunzione dell'arteria comunicante anteriore e l'arteria cerebrale media (Fig. 1). Sono state eseguite una simulazione a pareti rigide (CFD) e una a pareti deformabili (FSI) sul modello processato in SimVascular. Parallelamente una formulazione della 3DVar è stata implementata in FEniCS assumendo condizione stazionarie di flusso per l'equazione di Navier-Stokes. I risultati di entrambe le procedure sono stati confrontati per valutare l'efficacia e la precisione della 3DVar implementata nella stima dell'emodinamica all'interno dell'aneurisma.

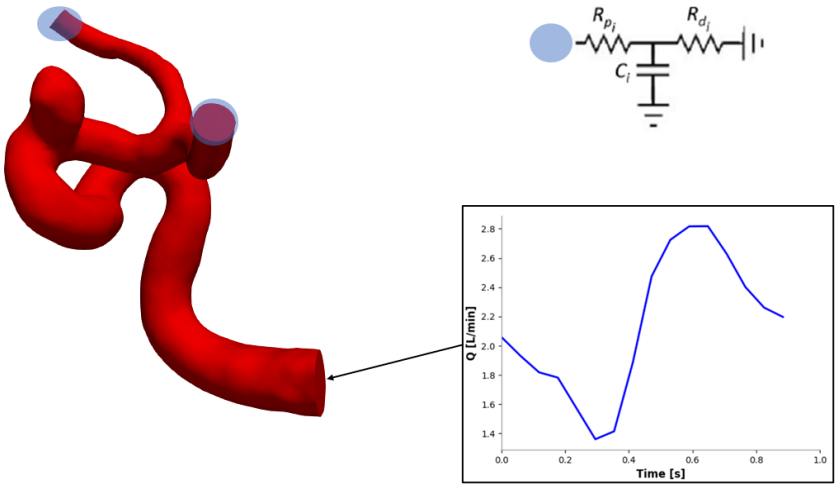

Figure 1: Rappresentazione del modello computazionale e descrizione delle condizioni al contorno; una portata paziente-specifica e un modello di Windkessel a 3 elementi (3-EWK) sono stati prescritti rispettivamente in ingresso e nelle due uscite.

Simulazioni numeriche

Analisi di sensitività

La geometria in Fig. 1 è stata discretizzata mediante il tool TetGen incorporato all'interno di SimVascular. Un'analisi di sensitività è stata eseguita su tre mesh con un numero di elementi gradualmente crescente, mediante simulazioni stazionarie, rappresentanti l'istante di tempo di massima portata. La velocità è stata valutata lungo un piano perpendicolare al collo dell'aneurisma ed è stato calcolato il Grid Convergence Index (GCI) [31] per ognuna delle tre mesh. La mesh media con ~ 4 milioni di elementi tetraedrici, ottenuta assumendo un *Global Max Edge Size* di 0.152 mm, è stata scelta per le successive simulazioni.

Simulazioni 4D flow guided-CFD e FSI

Il sangue è stato modellato come fluido Newtoniano in accordo con [32], assumendo un densità $\rho = 1.06 g/cm^3$ e una viscosità $\mu = 0.004$Poise. La simulazione a pareti rigide (CFD) è stata inizializzata con i parametri di default impostati in SimVascular. Invece, per la simulazione a pareti deformabili (FSI), è stato definito un Initial Condition (IC) file così come richiesto dal Coupled Momentum Method (CMM) su cui la FSI implementata in SimVascular si basa [33]. Il flusso è stato considerato stazionario, poiché il numero di Reynolds stimato lungo un piano perpendicolare al collo dell'aneurisma era uguale a 202 («2000). In inlet è stata impostata una curva di portata tempo variante estratta dal 4D flow. In ogni uscita, invece, sono stati calibrati dei modelli di Windkessels a 3 elementi seguendo l'approccio descritto in [34], in modo da tener conto del sistema vascolare distale e ottenere portate e curve di pressione fisiologiche (Fig. 1).
In SimVascular sono state eseguite una simulazione a pareti rigide (4D flow guided-CFD) e due a pareti deformabili (4D flow guided-FSI, Uniform-FSI e NonUniform-FSI). In Uniform-FSI, il vaso è stato modellato come elastico con un modulo di Young E=1MPa e uno spessore costante di $\zeta = 300\mu$m. In NonUniform-FSI, invece, è stato considerato intorno all'aneurisma un assottigliamento della parete pari a $\zeta = 100\mu$m, in accordo a [16]. Le simulazioni in SimVascular sono state eseguite per tre cicli cardiaci affinché si raggiungesse la desiderata convergenza dei residui e la periodicità della soluzione.

DA framework

La Var DA è stata implementata in FEniCS, un software open-source per la risoluzione dell'equazioni differenziali alle derivate parziali [35], e definita come un problema di ottimizzazione vincolato dall' equazione di Navier-Stokes (vedi Eq. 1), seguendo l'approccio riportato in [30]. La formulazione debole dell'equazione di Navier-Stokes è stata modificata, aggiungendo una forzante fittizia **c**, che agisse come variabile di controllo nella procedura di ottimizzazione. La formulazione debole si presenta quindi come segue:

$$\begin{aligned} F(\mathbf{u}^{k+1}, \mathbf{v}, p^{k+1}, q, \mathbf{c}) = (\frac{\mathbf{u}^{k+1} - \mathbf{u}^{k}}{\delta t}, \mathbf{v})_{\Omega} + ((\mathbf{u}^{k+\theta} \cdot)\nabla \mathbf{u}^{k+\theta}, \mathbf{v})_{\Omega} + \\ (p^{k+1}, \nabla \mathbf{v})_{\Omega} - (\nu \nabla \mathbf{u}^{k+\theta}, \nabla \mathbf{v})_{\Omega} - (q, \nabla \mathbf{u}^{k+1})_{\Omega} + \\ (\chi \mathbf{c}, \mathbf{v})_{\Omega} \quad \forall \mathbf{v} \in V, \forall q \in Q \end{aligned} \tag{2}$$

con **u** velocità, p pressione e **v** e q adeguate funzioni test. Il ruolo della variabile di controllo **c** era di forzare il campo di velocità ad assomigliare ad una soluzione target. Il framework complessivo dell'approccio implementato può essere sintetizzato in tre steps:

1. Risoluzione di una simulazione stazionaria a pareti rigide (The Tape)
2. Problema di ottimizzazione
3. Risoluzione di una simulazione stazionaria a pareti rigide con i parametri ottimizzati.

La formulazione debole dell'equazione di Navier-Stokes è stata discretizzata nel tempo e nello spazio. La simulazione è stata trattata come transitoria anche se sono state fornite condizioni al contorno stazionarie. Questa tecnica numerica è stata adottata per stabilizzare il termine convettivo. Un profilo di velocità, estratto dal 4D flow, è stato prescritto in ingresso mentre una pressione nulla è stata imposta all'uscita. Il sangue è stato modellato come fluido Newtoniano con gli stessi parametri reologici utilizzati per le simulazioni effettuate in SimVascular. L'obiettivo della ottimizzazione è di trovare un'approssimazione della variabile di controllo **c** che minimizzi un funzionale J definito come segue:

$$J(\mathbf{u}) = || \mathbf{u} - \mathbf{u}_{obs} ||_{L^2(\Omega)} \tag{3}$$

con $\mathbf{u}_{obs}$ soluzione target per la DA. Il problema adjoint, derivante dalla procedura di ottimizzazione, è stato risolto mediante il tool per la differenziazione algoritmica `dolfin-adjoint` [36]. La Var DA implementata è stata testata su due modelli 2D con

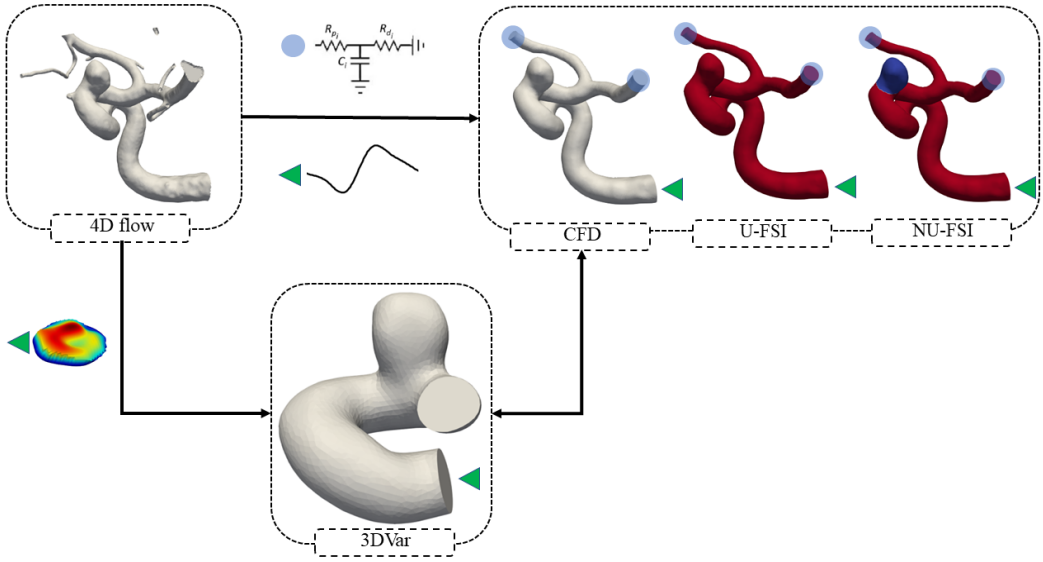

Figure 2: Rappresentazione schematica di tutto il lavoro affrontato specificando le condizioni al contorno e le ipotesi di modello adottate nelle simulazioni. La 3DVar è stata implementata per ricosturire il flusso sanguigno all'interno dell'aneurisma a partire da dati 4D flow e confrontata con una simulazione CFD a flusso transitorio.

osservazioni "sintetiche" per quantificare la qualità della soluzione assimilata e l'influenza del parametro di regolarizzazione R. Successivamente, la 3DVar è stata implementata per ricostruire il flusso sanguigno da misure estratte dal 4D flow all'interno di un modello 3D di un aneurisma cerebrale, ottenuto clippando il modello in Fig. 1 per ridurre il costo computazionale. Per la 3DVar è stato usato solo il time frame del 4D flow corrispondente al picco di portata. Nella 3DVar, l'algoritmo di ottimizzazione implementato nella libreria di FEniCS ha fallito a causa di problemi di convergenza. Quindi, un algoritmo iterativo basato sulla discesa del gradiente è stato implementato ad-hoc per convenire a questo problema. L'efficacia della 3DVar è stata validata confrontando la soluzione assimilata con i dati 4D flow e con la simulazione 4D flow guided-CFD all'istante di tempo di massima portata. La Fig. 2 mostra una rappresentazione sintetica di tutto il lavoro affrontato.

Risultati

Innanzitutto, sarà analizzato il ruolo delle simulazioni 4D flow guided-CFD e FSI nella valutazione dell'emodinamica degli aneurismi cerebrali. In seguito, saranno valutati gli esperimenti numerici eseguiti per testare la Var DA. Particolare considerazione sarà data alla 3DVar formulata per ricostruire le condizioni di flusso in un modello realistico di aneurisma cerebrale a partire dal 4D flow.

Simulazioni 4D flow guided-CFD e FSI

Confronto fra 4D flow, CFD e NonUniform-FSI

I risultati della CFD e NonUniform-FSI sono stati confrontati con il 4D flow per quantificare la similarità tra i risultati numerici e le misurazioni. Un'accettabile corrispondenza è stata trovata tra le portate tempo-dipendenti in uscita tra 4D flow, CFD e NonUniform-FSI. Le portate in uscita stimate da CFD e NonUniform-FSI erano 0.92 L/min e 0.94 L/min per l'Outlet Small, 1.20 L/min e 1.17 L/min per l'Outlet Large, rispettivamente. Le mappe a colori della velocità estratte lungo due piani perpendicolari all'interno dell'aneurisma hanno mostrato che sia la CFD che la NonUniform-FSI replicano la formazione del vortice apprezabile dal 4D flow (Fig. 3). Tuttavia, questo confronto ha mostrato che CFD e NonUniform-FSI forniscono campi di velocità molto simili, con una differenza massima nel modulo della velocità di 5 cm/s e solo in una regione molto ristretta dell'aneurisma.

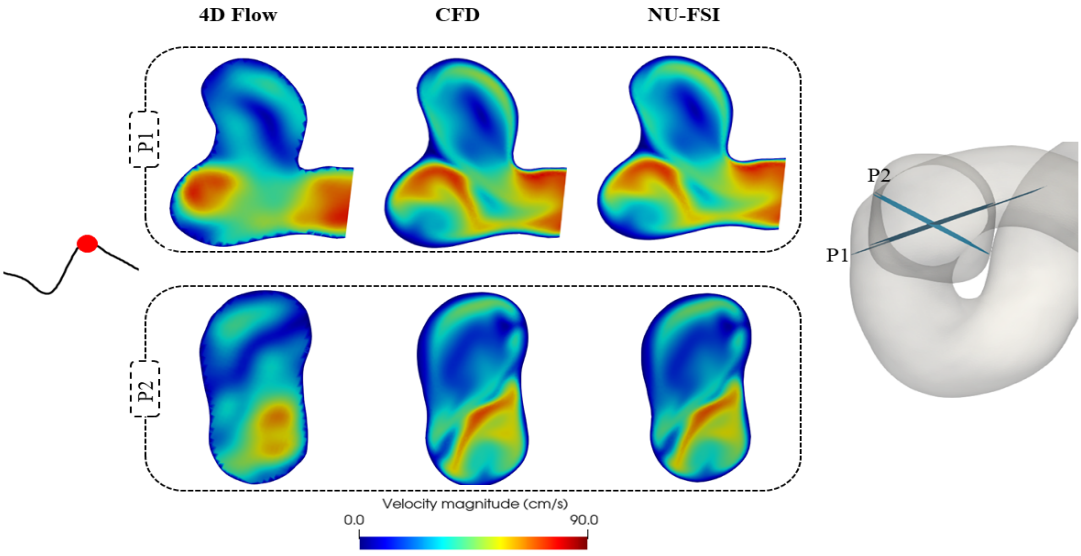

Figure 3: Mappe a colori della velocità estratte da due piani perpendcolari all'interno dell'aneurisma da 4D flow, CFD e NonUniform-FSI (NU-FSI) all'istante di massima portata.

CFD, Uniform-FSI e NonUniform-FSI: un confronto qualitativo e quantitativo

Il confronto tra CFD e FSI (Uniform- e NonUniform-FSI) ha permesso di analizzare l'incidenza della deformabilità del vaso sulla valutazione dell'emodinamica nelle simulazioni numeriche. Il confronto fra i due approcci si è focalizzato sulla pressione. La pressione mediata sull'area superficiale dell'aneurisma è stata valutata su tutto il ciclo cardiaco come mostrato in

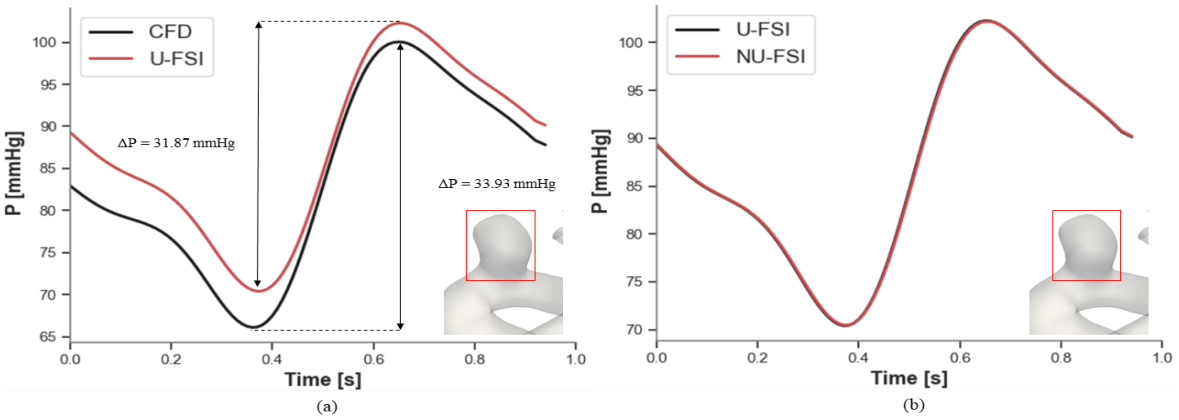

Figure 4: Pressione mediata sull'area dell'aneurisma nel tempo. (a) Confronto tra CFD e Uniform-FSI (U-FSI) con particolare attenzione al $\Delta P = P_{Max} - P_{Min}$. (b) Confronto tra Uniform-FSI e NonUniform-FSI (NU-FSI).

Fig. 4. La figura (Fig. 4a), evidenzia una massima differenza di pressione $\Delta P = P_{Max} - P_{Min}$ minore in Uniform-FSI (31.87mmHg) rispetto alla CFD (33.93mmHg). Lo stesso confronto, per Uniform- e NonUniform-FSI non mostra nessuna differenza significativa nella distribuzione della pressione lungo la superficie dell'aneurisma (Fig 4b).
Tuttavia l'entità degli spostamenti della parete dell'aneurisma è raddoppiata in NonUniform-FSI per l'intero ciclo cardiaco (Table 1). Di conseguenza, l'assottigliamento della parete, di cui la NonUniform-FSI tiene conto, ha determinato un incremento medio nel tempo di $\sim 47\%$ nella deformazione massima principale come mostrato in Tabella 1.

Valutazione dell'emodinamica nell'aneurisma cerebrale: WSS e OSI

WSS, TAWSS e OSI sono stati estratti dai risultati della CFD. In questa analisi, i risultati delle simulazioni FSI sono stati esclusi dato che non hanno fornito nessuna informazione aggiuntiva sulla distribuzione della velocità all'interno dell'aneurisma. La Fig. 5 mostra le mappe a colori per il WSS in tre significativi istanti temporali del ciclo cardico, e le mappe a colori per TAWSS e OSI. L'aneurisma protrude da una regione soggetta ad alti WSS. Diversamente, i WSS sono per lo più bassi sulla superficie dell'aneurisma. La mappa a colori per il TAWSS è consistente con la distribuzione del WSS durante il ciclo cardiaco. Inaspettatamente, l'OSI è circa zero lungo tutta la superficie dell'aneurisma. Il 95^{th} percentile

		T1	T2	T3
Uniform-FSI				
Displacement				
	Maximum [cm]	0.029	0.034	0.042
	95^{th} percentile [cm]	0.026	0.024	0.033
Strain				
	Maximum [%]	10.1	11.6	14.9
	95^{th} percentile [%]	7.57	8.69	11.0
NonUniform-FSI				
Displacement				
	Maximum [cm]	0.057 (+49%)	0.065 (+48%)	0.082 (+48%)
	95^{th} percentile [cm]	0.040 (+44%)	0.046 (+43%)	0.058(+43%)
Strain				
	Maximum [%]	28.0 (+64%)	32.2 (+64%)	42.5 (+65%)
	95^{th} percentile [%]	14.3 (+47%)	16.4 (+47%)	21.1 (+47%)

Table 1: Massimo e $95th$ percentile dello spostamento e della deformazione massima principale calcolati lungo le superfici dell'aneurisma e del vaso prossimale ad esso. Confronto fra Uniform-FSI e NonUniform-FSI in 3 distintivi istanti temporali del ciclo cardiaco (T1, T2, T3). Gli incrementi percentuali dello spostamento e dalla deformazione per la NonUniform-FSI rispetto alla Uniform-FSI sono riportati tra parentesi.

del modulo del WSS calcolato lungo tutta la superficie del modello varia significativamente durante il ciclo cardiaco, oscillando tra un valore minimo di 10.51 Pa e un massimo di 22.22 Pa. Lungo la parete dell'aneurisma, il massimo modulo del WSS ottenuto all'istante di massima portata era 16.60 Pa.

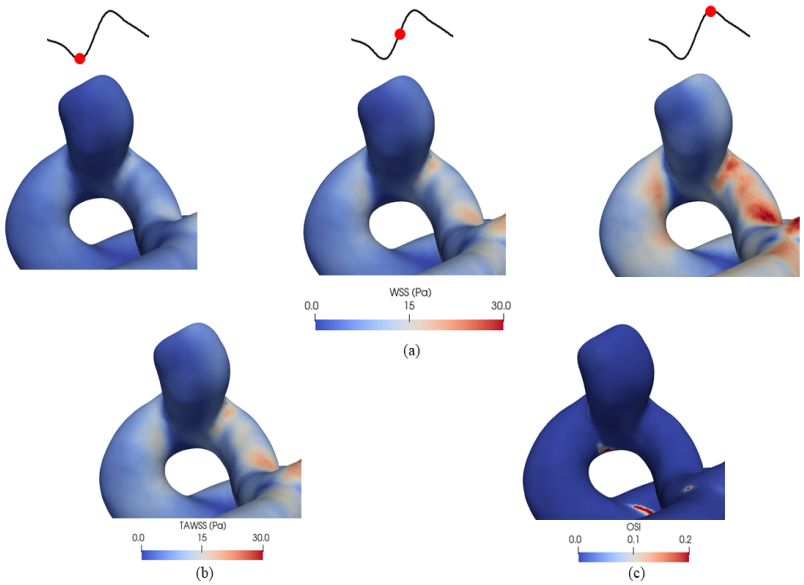

Figure 5: La figura mostra le mappe a colori per il modulo del WSS in tre significativi instanti temporali (a) e per il TAWSS (b) e per l'OSI (c) lungo la superficice dell'aneurisma.

Data Assimilation

Esperimenti 2D

Nei due esperimenti bidimensionali (*2D-Ane* e *Hole*) è stata trovata una buona somiglianza tra la velocità assimilata e le osservazioni "sintetiche" per parametri di regolarizzazione α compresi tra 10^{-4} and 10^{-2}. Come mostrato in Fig. 6, il RMSE del modulo della velocità per la soluzione assimilata rispetto alle osservazioni migliora per $\alpha = 10^{-4}$ del 41% e 43% in *2D-Ane* and *Hole*, rispettivamente, se confrontato con la velocità stimata dalla CFD (soluzione a $it = 0$). Tuttavia, la variabile di controllo introduce degli artifatti numerici che appaiono come discontinuità nel campo di velocità lungo i bordi del dominio in cui la velocità è soggetta alla DA, sopratutto in *2D-Ane*. In particolare, è stato osservato che la variabile di controllo non ha operato uniformemente su tutto il dominio ma principalmente in specifiche regioni.

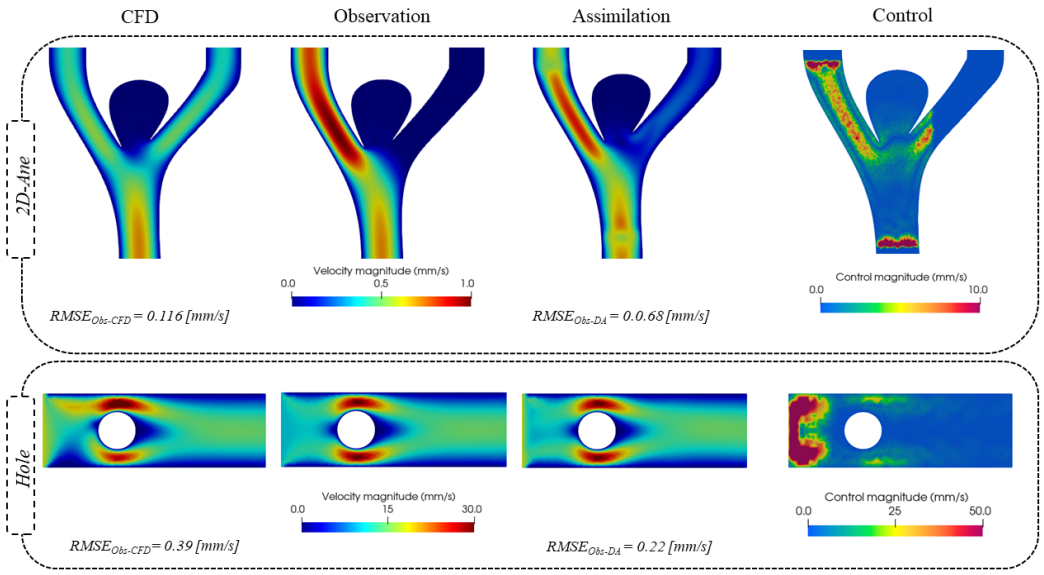

Figure 6: La DA negli esperimenti bidimensionali assumendo $\alpha = 10^{-4}$. Confronto tra la soluzione assimilata, le osservazioni e la CFD (soluzione a $it = 0$) in *2D-Ane* (prima riga) and *Hole* (seconda riga) insieme alle mappe a colori per la variabile di controllo su i due domini.

3DVar

LA 3DVar è stata applicata su tutto il dominio tridimensionale per riconstruire il flusso sanguigno all'istante temporale di massima portata a partire dal 4D flow. Una buona similarità è stata trovata tra la velocità assimilata all'ultima iterazione di ottimizzazione e il 4D flow come mostrato in Fig. 7. In accordo con gli esperimenti bidimensionali, la variabile

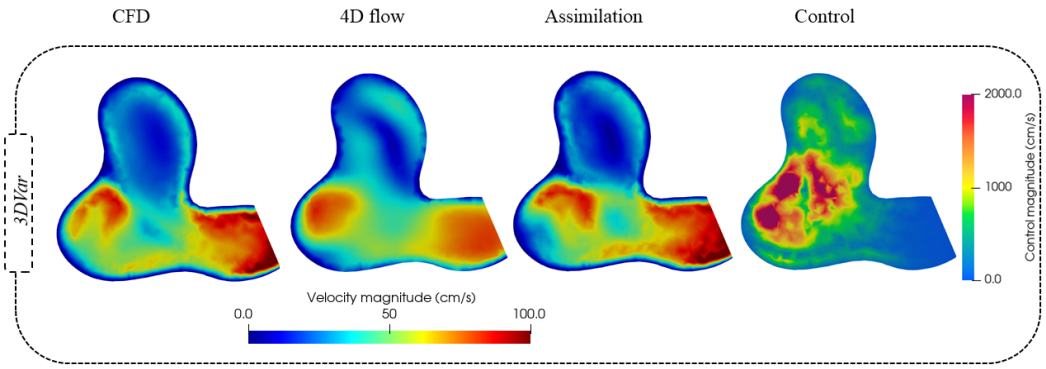

Figure 7: Confronto fra la soluzione assimilata nel modello tridimensionale con il 4D flow e la CFD (soluzione a *it=0*) mediante mappe a colori del modulo della velocità estratte su un piano perpendicolare all'aneurisma. Raffigurazione della mappa a colori della variabile di controllo lungo lo stesso piano.

di controllo (Fig. 7) ha operato principalmente su una regione ristretta del dominio. Come atteso, la 3DVar ha consentito di aumentare la risoluzione spaziale delle osservazioni. Tuttavia, grazie alla sua peculiare formulazione, la 3DVar implementata ha permesso di migliorare anche la risoluzione temporale del 4D flow. Infatti, formulando il problema di ottimizzazione come tempo-dipendente, la DA è eseguita per ogni iterazione di Navier-Stokes, incrementando l'informazione temporale tra due frame consecutivi del 4D flow. In Fig. 8, la 3DVar è confrontata con la simulazione 4D flow guided-CFD eseguita in SimVascular (High-resolution CFD). Sebbene, la mappa a colori del modulo della velocità appaiano meglio risolute e definite nella High-resolution CFD, l'andamento del flusso è consistente con la 3DVar, e entrambe le tecniche sono state in grado di catturare la formazione del vortice all'interno dell'aneurisma in accordo con il 4D flow. Il RMSE del modulo della velocità rispetto al 4D flow riportato in figura, evidenzia come la 3DVar si avvicini meglio alle osservazioni della CFD ad alta risoluzione spaziale. Complessivamente, il campo di flusso ottenuto con la 3DVar, si avvicina sia al 4D flow che alla High-resolution CFD.

Discussione e conclusioni

Come già affermato nei precedenti capitoli, caratterizzare l'emodinamica all'interno degli aneurismi cerebrali è un fattore determinante per predirne l'evoluzione e la possibile rottura.

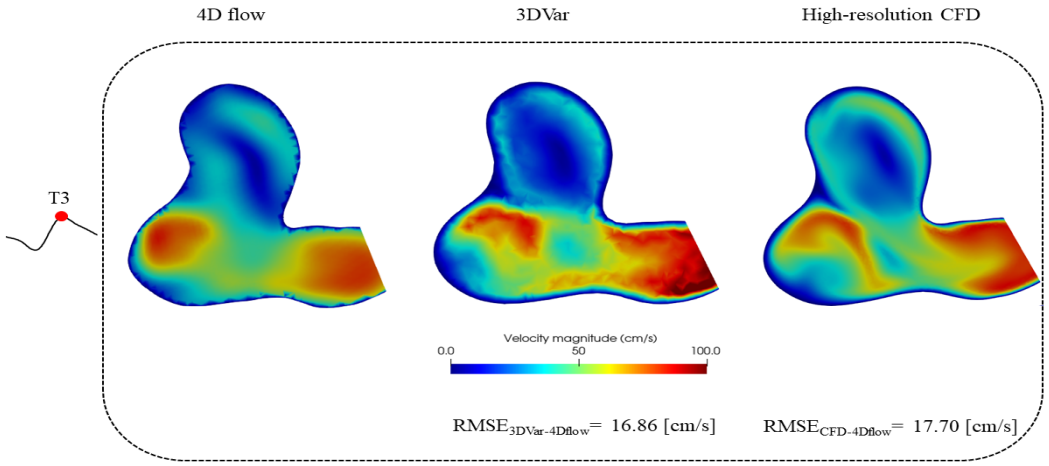

Figure 8: Mappe a colori estratte da un piano perpendicolare all'aneurisma per il 4D flow, la 3DVar e la High-resolution CFD con il RMSE del modulo della velocità per la 3DVar e la 4D flow guided-CFD rispetto al 4D flow.

Il flusso sanguigno può essere valutato o mediante le simulazioni numeriche, o servendosi delle tecniche di imaging. Purtroppo, entrambi gli approcci hanno delle limitazioni che possono osatacolare la loro applicazione in clinica. La DA è un approccio matematico innovativo che permette di combinare le simulazioni numeriche con le misure da 4D flow, migliorando l'accuratezza della stima del flusso e la valutazione emodinamica. In questo studio, è stato implementato un algoritmo di DA (3DVar), andando poi a valutare le capacità di quest'ultimo nel ricostruire il flusso sanguigno in un modello tridimensionale di un aneurisma cerebrale a partire dai dati forniti dal 4D flow. Parallelamente, è stato esaminato il ruolo dei modelli numerici nella valutazione dell'emodinamica degli aneurismi cerebrali. L'efficacia e l'accuratezza della 3DVar implementata è stata valutata confrontandola con i risultati ottenuti mediante una simulazione CFD le cui condizioni al controno sono state estratte dal 4D flow.

Simulazioni 4D flow guided-CFD e FSI: emodinamica degli aneurismi cerebrali

Le simulazioni CFD e FSI hanno dimostrato di essere metodi affidabili per la ricostruzione del flusso sanguigno mediante un confronto qualitativo e quantitativo con il 4D flow (massima accuratezza di $\sim 85\%$ nella stima della velocità). La massima accuretazza ottenuta era più alta di quella riportata in [19] e [20], confermando l'ottimo rendimento delle strategie di correzione [37] adottate per il 4D flow.

I risultati ottenuti dalla NonUniform-FSI non ha fornito alcuna informazione aggiuntiva nella stima del campo di velocità rispetto alla CFD. Anche se lo spostamento della parete è stato

significativo (massimo spostamento di 0.042cm al picco di flusso) e consistente con alcuni lavori precedenti [16, 17], il profilo di velocità all'interno dell'aneurisma è variato solo minimamente. D'altro canto, in [16] la deformabilità della parete ha alterato significativamente il profilo di velocità all'interno dell'aneurisma. Questa discrepanza può essere legata alle limitazioni della coupled-momentum method FSI implementata in SimVascular. In questa formulazione, il problema geometrico legato al movimento della parete non è risolto, in quanto la parete del vaso è considerata come una sottile membrana fortemente accoppiata al bordo del dominio fluido, in modo tale da ridurre il costo computazionale. Un'altra spiegazione per il modesto impatto della deformabilità della parete sul profilo di velocità all'interno dell'aneurisma può essere correlata alla forma e alla dimensione di quest'ultimo, come riportato in [15].
Tuttavia, le simulazioni FSI (Uniform- e NonUniform-FSI) hanno evidenziato lo smorzamento del flusso sanguigno dovuto alla deformabilità della parete, restituendo una minore differenza massima di pressione lungo la superficie dell'aneurisma durante il ciclo cardiaco. Come citato precedentemente, il campo degli spostamenti ottenuto in Uniform-FSI (Massimo spostamento = 0.042cm) è in accordo con [16] (Massimo spostamento = 0.035cm). In NonUniform-FSI, l'entità dello spostamento lungo l'aneurisma è raddoppiato rispetto alla Uniform-FSI come riportato in [17] in cui è stato considerato il medesimo assottigliamento della parete. Dai risultati della CFD è stata estratta la mappa a colori dei WSS. Il massimo WSS calcolato lungo la parete dell'aneurisma era $\sim$ 6% maggiore di quello ottenuto in [38] e in perfetto accordo con [39] e [40]. Inoltre, la distribuzione del WSS trovata può giustificare la posizione dell'aneurisma. Infatti, l'aneurisma protrude da una regione soggetta ad alti WSS, solitamente associati alla formazione e crescita degli aneurismi cerebrali [41].

Variational DA in 2D e 3D

L'aspetto innovativo della VarDA qui implementata è la sua formulazione. Nei precedenti lavori [28, 29, 30], la VarDA mirava a ottenere ideali condizioni di ingresso e di uscita dalle misure. In questo studio, invece, la DA è stata eseguita controllando una forzante fittizia aggiunta alla formulazione debole di Navier-Stokes. Questa forzante constringeva il flusso sanguigno a seguire una soluzione di riferimento. Negli esperimenti bidimensionali, la qualità della DA peggiorava con parametri di regolarizzazione $\alpha > 10^{-2}$ in accordo con [30]. Tuttavia, gli artifatti numerici introdotti dalla variabile di controllo per $\alpha = 10^{-4}$ evidenziano il rischio di overfitting delle osservazioni quando la VarDA è applicata su una restrizione del dominio. La 3DVar è stata implementata per simulazioni fluidodinamiche a regime stazionario

e eseguita su l'intero dominio per ricostruire il flusso sanguigno da 4D flow. Per la 3DVar, l'algoritmo di ottimizzazione implementato nella libreria `dolphin-adjoint` ha fallito a cause dell'incremento nella dimensionalità del problema rispetto agli esperimenti bidimensionali. L'algoritmo di optimizzazione è lo stesso usato da Funke et al. [30] nella 4DVar implementata per simulazione fluidodinamiche a regime transitorio. Tuttavia, la variabile di controllo applicata qui era dimensionalmente più grande e quindi più costosa dal punto di vista computazionale per la procedura di ottimizzazione. Ad ogni modo, l'algoritmo di ottimizzazione, basato sulla discesa del gradiente e implementato ad-hoc, ha garantito una sufficiente minimizzazione del funzionale e una accetabile similarità tra la soluzione assimilata e il 4D flow, confermando l'efficacia della 3DVar implementata. L'approccio ha permesso di ridurre il rumore e aumentare la risoluzione nel 4D flow. In particolare, la peculiare formulazione della 3DVar in questo studio permette di aumentare arbitrariamente la risoluzione temporale del 4D flow scegliendo liberamente il numero delle iterazioni temporali di Navier-Stokes da eseguire nel processo di ottimizzazione.

3DVar e High-resolution CFD nella ricostruzione del flusso sanguigno in aneurismi cerebrali

La 3DVar ha consentito di ottenere una migliore analogia con il 4D flow rispetto alla High-resolution CFD ($\sim -5\%$ nel RMSE del modulo della velocità) all'interno della regione d'interesse pur usando una mesh più lasca (700mila vs 1.3milioni di elementi). In generale, l'affidabilità nella stima della emodinamica per le simulazioni 4D flow based dipende dalla qualità della mesh, dall'acuratezza della stima delle proprietà meccaniche della parete (nel caso di simulazione FSI), e dalla corretta calibrazione delle condizioni al contorno in uscita che dipendono da stime di pressione difficilmente ottenibili per le arterie cerebrali. Dall'altra parte, la 3DVar ha dimostrato di essere un valido metodo per aumentare l'accuratezza dei modelli numerici nella stima dell'emodinamica all'interno degli aneurimi cerebrali, sfruttando interamente le misure fornite dal 4D flow. In aggiunta, la 3DVar è stata applicata solo all'istante temporale di massima portata. Tuttavia, estendendo la procedura su tutto il dataset del 4D flow, potrebbe essere possibile ricostruire la dinamica del sangue su tutto il ciclo cardiaco.

Conclusione

In conclusione, questo studio ha analizzato il ruolo delle simulazioni CFD e FSI 4D flow based nella valutazione dell'emodinamica degli aneurismi cerebrali, e ha proposto una formulazione euristica della 3DVar per ricostruire il flusso sanguigno all'interno degli aneurismi cerebrali a partire dai dati forniti dal 4D flow. Il metodo proposto ha dimostrato di essere efficace nel combinare simulazione numeriche e dati di 4D flow, garantendo una migliora accuratezza delle simulazione CFD. Questo metodo è molto interessante per l'analisi emodinamica dei distretti cardiovascolari in cui i parametri per la definizione del modello numerico, come la pressione o le proprietà della parete, sono difficili da ottenere, basandosi unicamente sulle acquisizioni 4D flow. Attualmente, non esistono in letteratura formulazioni della 3DVar di questo tipo. L'algoritmo qui implementato rappresenta uno sforzo verso un'efficace fusione dei modelli numerici e il 4D flow, con un importante risvolto nel migliorare la valutazione del rischio di rottura degli aneurismi intracranici.

Abstract

Clinical background and numerical approach

Cerebral or intracranial aneurysm (IA) is a cerebrovascular disorder in which a weakening of the inner muscle layer of the blood vessel causes abnormal dilatation or ballooning [1]. The rupture of cerebral aneurysms leads to subarachnoid haemorrhage (SAH), a relevant health problem with a mortality rate of about 60% within the first six months [2]. Most of the unruptured aneurysms are silent, often do not cause any symptoms and are usually discovered incidentally. Therefore, predicting aneurysm rupture becomes crucial to guide healthcare specialist in determining the best course of action in treating IAs.

Several risk factors for aneurysm rupture have been identified and are currently used in clinics. Age and hypertension seem to have a high impact in determining aneurysm rupture, together with size, location and morphology of the aneurysms [2, 3]. Specific morphological parameters were defined to characterized IAs as aspect ratio (AR), size ratio (SR), flow angle (FA) and height-width ratio (H/W), and some of them have been associated explicitly with aneurysms rupture [4]. Monitoring and supporting the diagnosis of IA relies on imaging evaluation, such as Digital Subtraction Angiography (DSA), Computed Tomography Angiography (CTA) or Magnetic Resonance Angiography (MRA) [3]. Traditional image-based diagnosis is crucial for aneurysm risk stratification, but allows only for a morphological evaluation of IAs. Four-dimensional (4D) magnetic resonance imaging (MRI), or 4D flow MRI, is an emerging, non-invasive technique that enables measurements of the blood flow and hemodynamics evaluation [5]. 4D flow MRI has been effectively applied for the assessment of arterial and venous hemodynamics in various anatomic regions in the human body [5], including IAs [6, 7, 8]. This type of analysis allows for associating aneurysm morphology with hemodynamics parameters, enriching aneurysm risk factor assessment. Nevertheless, low spatial and temporal resolution, and velocity sensitivity (VENC) are significant limiting factors for 4D flow, particularly in the computation of wall shear stress, which has been

suggested to play an important role in the development and rupture of cerebral aneurysms [42].

Numerical models have proved to be valuable for simulating blood flow, providing a comprehensive hemodynamics evaluation in several cardiac districts, including IAs [9, 10]. Computational fluid dynamics (CFD) allows to analyze, in rigid domains, intra-aneurysmal hemodynamics in both qualitative and quantitative ways. By CFD analyses, high AR ($>$ 2.2) cerebral aneurysms have been associated with lower speed flow, lower TAWSS, lower WSS at peak systole and higher OSI [11]. High SR aneurysms were found to be related to multiple and complex flow patterns in [12], making SR a discriminant factor between ruptured and unruptured aneurysms [43]. In two related works, Cerebral et al. [13, 14], by carrying patient-specific CFD simulations, assessed that disturbed flow patterns, small impingement regions, and narrow jet are discriminant factor for ruptured aneurysms. CFD analysis are the gold standard for WSS estimation. In particular, Meng et al. argued that high WSS have a major role in IAs initiation and growth, while low WSS are crucial in rupture. Despite CFD has proven to be a powerful tool for assessing blood flow-related parameters, the rigid-wall assumptions limits the fidelity of this approach. Fluid-structure interaction (FSI) simulations allow to account for vessel-blood interaction and a few studies have performed FSI analyses on patients specifics aneurysms models [15, 16, 17, 18]. In general, CFD was found to overestimate WSS with respect to FSI simulations even if blood flow velocities did not seem altered [15]. Wall displacements was found non-negligible on the aneurysm wall, mostly assuming a pathological wall thinning, resulting in a reduction in WSS absolute value [17] and better correlation of stress distribution with rupture sites [18]. Currently, CFD and FSI models are the gold standard in hemodynamic assessment. However, the reliability of numerical models depends on hypothesis and measurements, such as geometry reconstruction, blood constitutive model and boundary conditions (BCs) that may hamper their clinical implementation. Patient-specific geometry and BCs can be extracted by clinical images with an acceptable level of reliability. For example, 4D flow MRI enables reliable measurements of blood flows to apply as inlet and outlet BCs for numerical models (4D flow based-numerical models). In [19, 20], a good agreement in blood flow reconstruction between 4D flow MRI and 4D flow based-CFD was found, especially in systolic phase. Nevertheless, as shown in [21], 4D flow MRI-derived WSS was found lower in magnitude than CFD-derived WSS even if the relative distribution was similar. The discrepancies between these two techniques are mainly due to the aforementioned limitations of 4D flow [22], but also to the accounted vessel

motion in the measurements [23]. A promising remedy could be hence to incorporate the available data (4D flow measurements) and control parameters in a simulation framework, using data assimilation (DA). DA is a mathematical approach, well established in numerical weather predictions [24], that aims at optimally combining results from numerical models with observation. In hemodynamics, noisy and uncertain 4D flow data can be incorporated into numerical simulations improving the accuracy and physical correctness of the measured velocity fields with DA. One of the most used strategy to perform DA is the Varational DA (shortly Var, or in its specific 3D implementation 3DVar). In Var the DA technique reads as an optimization problem, constrained by a partial differential equation (Navier-Stokes equations in hemodynamics), for the identification of a control variable $\mathbf{c}$, which minimizes a functional defined as a misfit between the computed velocity $\mathbf{u}$ and the velocity measure $\mathbf{u}_m$, with R regularisation term for the well-posedness of the problem.

$$\begin{aligned} \min_{\mathbf{c}} J(\mathbf{u}, \mathbf{c}) = \mathit{dist}(f(\mathbf{u}), \mathbf{u}_{\mathrm{m}}) + R(\mathbf{c}) \\ \text{s.t.} \qquad F(\mathbf{u}, \mathbf{c}) = 0 \end{aligned} \tag{4}$$

The effectiveness of Var in hemodynamics has been investigated in [25, 26, 27] by Elia et al. evaluating the accuracy of the procedure in reconstructing blood flow and computing WSS from synthetic noisy measurements in 2D [25, 26] and 3D [27] idealized models. Here, particular attention was paid to the mathematical formulation. In [28] a 3DVar was applied for the first time on a 3D real geometry of a saccular brain aneurysm for Dirichlet and Neumann boundary control but steady-state flow condition and synthetic data were assumed. In [29], Koltukluoğlu et al. proposed a steady-state 3DVar using *in vitro* 4D flow acquisition on a aorta glass replica, obtaining an optimized solution qualitatively and quantitatively closer to 4D flow measurements than the predictions from CFD. In [30], for the first time, a 3DVar in transient flow conditions (4DVar) was proposed in a realistic 3D canine aneurysm as optimization problem for identification of optimal boundary conditions to recover 4D flow measurements. The difference between the assimilated solution and the measurements was minimal and mostly due to the noise which affected the data, while high-resolution CFD provided a lower similarity with the observation.

Overall, DA is a promising approach to combine numerical models with 4D flow MRI, enabling super-resolution and noise reduction in 4D flow measurements which could have a high impact in IAs risk stratification. This work will present an innovative 3DVar approach for IA blood flow reconstruction from 4D flow data.

Materials and methods

A saccular IA model was extracted from 4D MRI data. The vascular geometry was then cut, smoothed (via shape-preserving interpolation) and remeshed. The final 3D model comprises the internal carotid artery (ICA) and the side-wall saccular aneurysm located at the bifurcation of ICA and the anterior communicating-middle cerebral arteries (ACA-MCA) junction (Fig. 9). 4D flow guided-CFD and FSI simulations were carried in SimVascular on the 3D IA model. A 3DVar formulation was implemented in FEniCS for the steady-state Navier-Stokes equations on the same model. Results from both procedures were compared to assess the efficacy and the accuracy of the implemented 3DVar in estimating intra-aneurysmal hemodynamics.

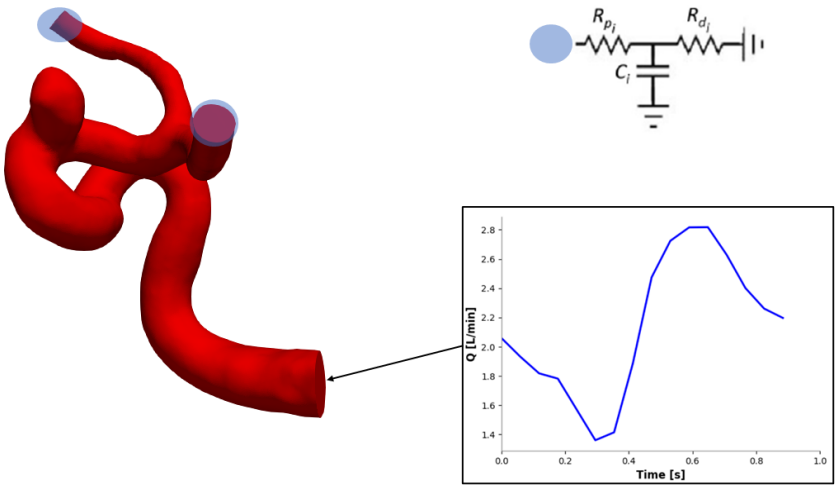

Figure 9: Representation of the model and description of boundary conditions used in the numerical simulations; patient-specific transient flow rate was imposed at the inlet, while 3-element Windkessels (3-EWK) were set as outlet boundary conditions.

Numerical simulations

Mesh sensitivity analysis

The geometry in Fig. 9 was meshed using the SimVascular embedded meshing tool TetGen, estimating a proper *Global Max Edge Size*. A mesh sensitivity analysis was performed by running steady flow simulations, representing the peak flow rate instant, on three meshes of gradually increased number of elements. Velocity magnitude contours were evaluated on a cross section within the aneurysm neck and the Grid Convergence Index (GCI) [31] was

estimated. The medium mesh of $\sim$ 4 millions of tetrahedral elements, obtained by using a *Global Max Edge Size* of 0.152 mm, was chosen for the final simulations.

4D flow guided-CFD and FSI simulations

Blood was modelled as Newtonian fluid according to [32], with a density of $\rho = 1.06 g/cm^3$ and a viscosity of $\mu = 0.004$Poise. Default initial conditions ($\mathbf{u}$=(0,0,0), p=0) were used to initialize the rigid wall (CFD) simulation. Instead, for the FSI simulation, a suitable Initial Condition (IC) file was provided as requested by the Coupled Momentum Method (CMM) algorithm on which the FSI implemented in SimVascular realises [33]. The blood flow regime was assumed laminar since the Reynolds number was equal to 202 ($\ll$ 2000) along a plane crossing the aneurysm neck. A time-varying flow rate curve extracted from 4D flow data was prescribed as inlet boundary condition. At each outlet, instead, 3-EWK models were set as boundary condition following the approach described in [34], in order to account for the effect of distal vasculature and obtain physiological flow rate and pressure curves (Fig. 9).
One rigid-wall simulation (CFD) and two deformable-wall simulations (Uniform-FSI, NonUniform-FSI) were carried out in SimVascular. In Uniform-FSI, the vessel wall was modelled as elastic with Young's modulus E=1MPa and a constant wall thickness $\zeta = 300\mu$m. Instead, in NonUniform-FSI, a thinning of the vessel wall around the aneurysm, $\zeta = 100\mu$m, was assumed according to [16].
CFD, Uniform-FSI and NonUniform-FSI were run for 3 cardiac cycles in order to reach the desired convergence residual and obtain periodicity of the solution.

DA framework

The Var DA formulation was implemented in the FEniCS finite element framework [35], and defined as an optimisation problem constrained by the Navier-Stokes equations (see Eq. 4), following the approach reported in [30]. The weak form of the Navier-Stokes equations was modified, adding a fictitious source term $\mathbf{c}$, which acts as control variable in the optimization procedure. The weak form reads then as follows:

$$\begin{aligned} F(\mathbf{u}^{k+1}, \mathbf{v}, p^{k+1}, q, \mathbf{c}) = (\frac{\mathbf{u}^{k+1} - \mathbf{u}^{k}}{\delta t}, \mathbf{v})_\Omega + ((\mathbf{u}^{k+\theta}\cdot)\nabla \mathbf{u}^{k+\theta}, \mathbf{v})_\Omega + \\ (p^{k+1}, \nabla \mathbf{v})_\Omega - (\nu \nabla \mathbf{u}^{k+\theta}, \nabla \mathbf{v})_\Omega - (q, \nabla \mathbf{u}^{k+1})_\Omega + \\ (\chi \mathbf{c}, \mathbf{v})_\Omega \quad \forall \mathbf{v} \in V, \forall q \in Q \end{aligned} \tag{5}$$

with $\mathbf{u}$ velocity, p pressure and $\mathbf{v}$ and q suitable test functions. The role of the control variable $\mathbf{c}$ was to force the velocity field to resemble a target solution. The overall implemented framework can be synthesized in three steps:

1. Solution of a steady-state, rigid-wall simulation (The Tape)

2. Optimization problem

3. Solution of a steady-state rigid-wall simulation with optimized parameters.

The weak form of the Navier-Stokes equations was discretized in time and space. The simulation was treated as transient even if steady boundary conditions were provided. This numerical technique was used to stabilize the convective term. A velocity field, extracted from the 4D flow data, was prescribed in inlet and pressure zero was assumed as outlet boundary condition. Blood was modelled as Newtonian fluid with same rheology parameters used for the CFD and FSI simulations in SimVascular. The optimization problem was defined as Eq. 4 and solved with a gradient-descent algorithm. The objective of the optimization is to find an approximation of the control variable $\mathbf{c}$ which minimizes a functional J defined as follows:

$$J(\mathbf{u}) = || \mathbf{u} - \mathbf{u}_{obs} ||_{L^2(\Omega)} \tag{6}$$

with $\mathbf{u}_{obs}$ target solution for DA. The adjoint problem, derived from the optimisation algorithm, was solved via the algorithmic differentiation tool `dolfin-adjoint` [36]. The implemented Var DA formulation was tested on two 2D set-ups with synthetic numerical observation in order to quantify the quality of the assimilated solution and the effect of the regularisation term R. Then, a 3DVar was implemented to reconstruct the blood flow from 4D flow measurements within a 3D cerebral aneurysm model, obtained by clipping the model in Fig. 9 in order to reduce the computational cost. Only the highest flow time frame of 4D flow data was used for the 3DVar. Basically, the velocity measurements were extracted from the 4D flow data and interpolated over the computational mesh. The optimization algorithm implemented in FEniCS libraries failed in the 3DVar formulation. Therefore, a custom iterative gradient descent-like algorithm was implemented to overcome this issue.
The 3DVar efficacy in reconstructing the blood flow in the IA model was validated against the 4D flow data, and the assimilated solution was compared with the transient CFD solution at the peak flow rate time instant. Fig. 10 shows a synthetic representation of the total workflow carried out.

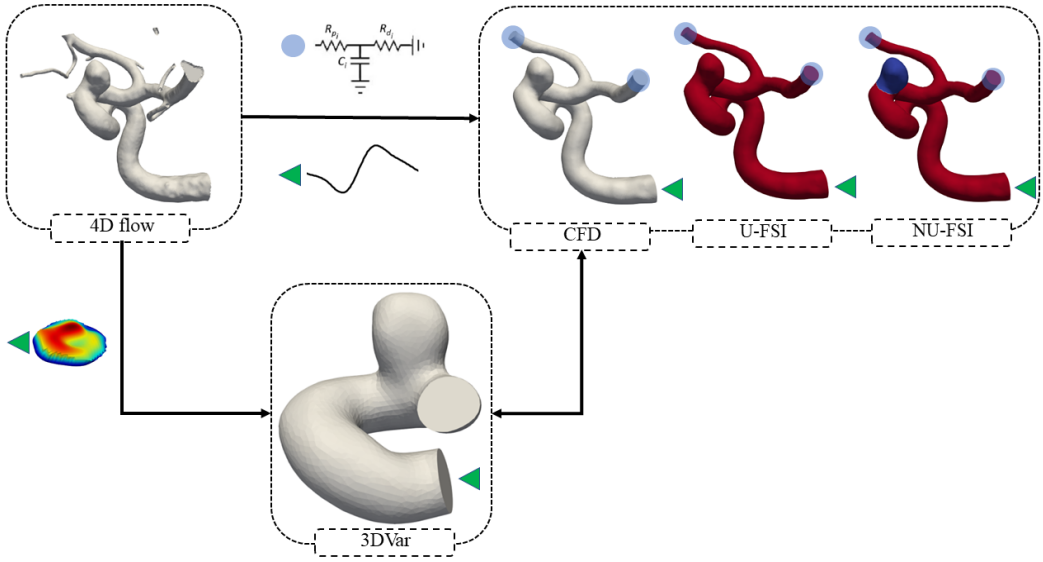

Figure 10: Schematic representation of the total workflow carried out. 4D flow based-CFD and FSI (Uniform-FSI and NonUniform-FSI) simulations were performed applying BCs extracted from 4D flow measurements. In NonUniform-FSI a thinning of the aneurysm wall was assumed (blue region). 3DVar was performed to reconstruct blood flow from the highest flow rate time frame of 4D flow, applying in inlet a velocity profile extracted from the measurements. The assimilated solution was compared with the transient-CFD.

Results

The role of CFD and FSI simulations in assessing IA hemodynamics will be first investigated. Then, the numerical experiments carried to test the Var DA will be analysed. Special consideration will be given to the 3DVar formulated to reconstruct the flow conditions in a real IA from 4D flow data.

4D flow guided-CFD and FSI simulations

Validation against 4D flow data

CFD and NonUniform-FSI results were compared against the 4D flow measurements to quantify the agreement between the numerical results and the clinical data. A good match was found between time-dependent outlet flow rates obtained with 4D flow, CFD and NonUniform-FSI. The outlet flow rates predicted by CFD and NonUniform-FSI were 0.92 L/min and 0.94 L/min for Outlet Small, 1.20 L/min and 1.17 L/min for Outlet Large, respectively. The velocity colour maps extracted from two cross-sectional planes within the aneurysm showed that both CFD and NonUniform-FSI replicated the vortex formation visible in 4D flow (Fig. 11). Nevertheless, this comparison highlighted that CFD and

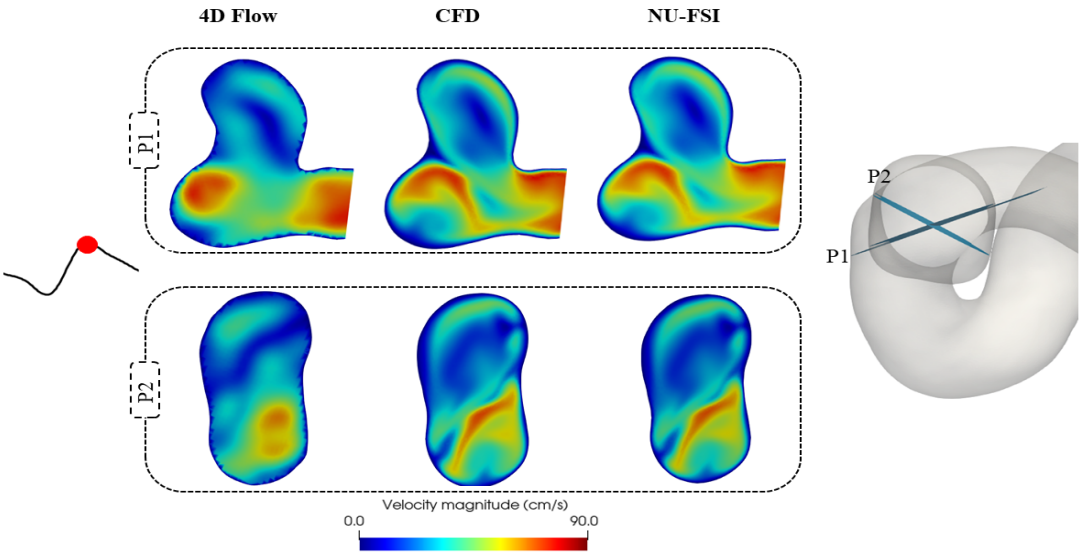

Figure 11: Velocity colour maps extracted on two cross-sectional planes within the aneurysm for 4D flow, CFD and Uniform-FSI (U-FSI) at the highest flow rate time instant.

NonUniform-FSI provided very similar velocity fields, with a maximum difference in velocity magnitude equal to 5 cm/s and only in a very restricted region of the aneurysm.

CFD, Unifrom-FSI and NonUniform-FSI: a qualitative and quantitative comparison

In order to evaluate the impact of wall deformability on the numerical hemodynamic assessment, the comparison between the CFD and the FSI (Uniform- and NonUniform-FSI) focused on the pressure field. Pressure was evaluated over the aneurysm surface and the surface-averaged pressure was plotted over time for a cardiac cycle as shown in Fig. 12. The figure (Fig. 12a), highlights a lower maximum pressure difference $\Delta P = P_{Max} - P_{Min}$ for Uniform-FSI (31.87mmHg) with respect to CFD (33.93mmHg). The same comparison, involving Uniform- and NonUniform-FSI did not show any significant difference in pressure field along the aneurysm surface (Fig 12b).

On the other hand, the displacement magnitude of the aneurysm wall doubled in NonUniform-FSI for the entire cardiac cycle (Table 2). Accordingly, the thinning assumption of the aneurysm wall in NonUniform-FSI established a time-averaged increment of $\sim 47\%$ in the maximum principal strain field along the aneurysm wall as shown in Table 2.

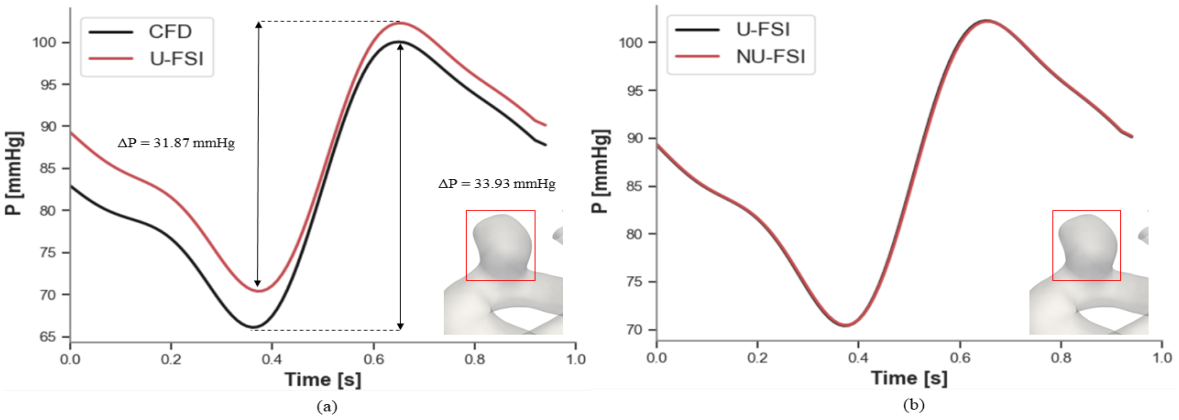

Figure 12: Aneurysm surface-averaged pressure over time. (a) Comparison between CFD and Uniform-FSI (U-FSI) with attention to the $\Delta P = P_{Max} - P_{Min}$. (b) Comparison between Uniform-FSI and NonUniform-FSI (NU-FSI).

		T1	T2	T3
Uniform-FSI				
Displacement				
	Maximum [cm]	0.029	0.034	0.042
	95^{th} percentile [cm]	0.026	0.024	0.033
Strain				
	Maximum [%]	10.1	11.6	14.9
	95^{th} percentile [%]	7.57	8.69	11.0
NonUniform-FSI				
Displacement				
	Maximum [cm]	0.057 (+49%)	0.065 (+48%)	0.082 (+48%)
	95^{th} percentile [cm]	0.040 (+44%)	0.046 (+43%)	0.058(+43%)
Strain				
	Maximum [%]	28.0 (+64%)	32.2 (+64%)	42.5 (+65%)
	95^{th} percentile [%]	14.3 (+47%)	16.4 (+47%)	21.1 (+47%)

Table 2: Maximum and $95th$ percentile of displacement and maximum principal strain field computed at the aneurysm and the proximal parent vessel wall for Uniform-FSI and NonUniform-FSI at three distinctive time points over the cardiac cycle referred to as T1, T2, T3. For NonUniform-FSI, the displacement and strain percentage increase with respect to Uniform-FSI is reported in brackets

Hemodynamics evaluation in intracranial aneurysm: WSS and OSI

WSS, TAWSS and OSI were extracted from CFD results. In this analysis, FSI results were excluded since they did not yield relevant additional information on the velocity field inside the aneurysm. Fig. 13 shows WSS contour maps at three distinct time points over the cardiac cycle, and TAWSS and OSI contour maps. The aneurysm protrudes from a region

affected by high WSS values. On the contrary, the WSS are overall low over the aneurysm surface. The TAWSS is consistent with the instantaneous WSS distribution. Remarkably, the OSI is close to zero all over the aneurysm surface. The 95^{th} percentile of WSS magnitude computed along all the model varied significantly over the cardiac cycle, oscillating between a minimum of 10.51 Pa and a maximum of 22.22 Pa. Along the aneurysm surface, the 95^{th} percentile of WSS reached 16.60 Pa at the highest flow rate time instant.

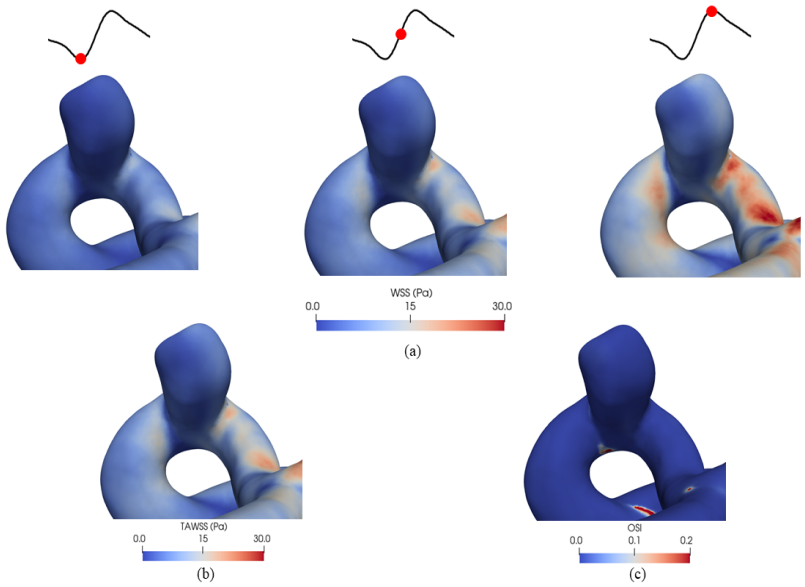

Figure 13: WSS magnitude, TAWSS and OSI colour maps. (a) Wall shear stress colour maps on a zoomed representation of the aneurysm region at three distinct time points. TAWSS (b) and OSI (c) colour maps on a zoomed representation of the aneurysm region.

Data Assimilation

2D experiments

In the two 2D experiments (*2D-Ane* and *Hole*) a good agreement was found between the assimilated velocity field and the synthetic data for regularisation parameters α ranging from 10^{-4} and 10^{-2}. As shown in Fig. 14, assuming $\alpha = 10^{-4}$ the RMSE of velocity magnitude for the assimilated solution against the observation improves with respect to the CFD solution before optimization by 41% and 43% in *2D-Ane* and *Hole*, respectively. However, the control introduced numerical artifacts that appear as discontinuities in the velocity field at the domain boundaries where the velocity is controlled by DA, especially in *2D-Ane*. Notably, the control variable did not act uniformly over the domain but peaked in restricted regions.

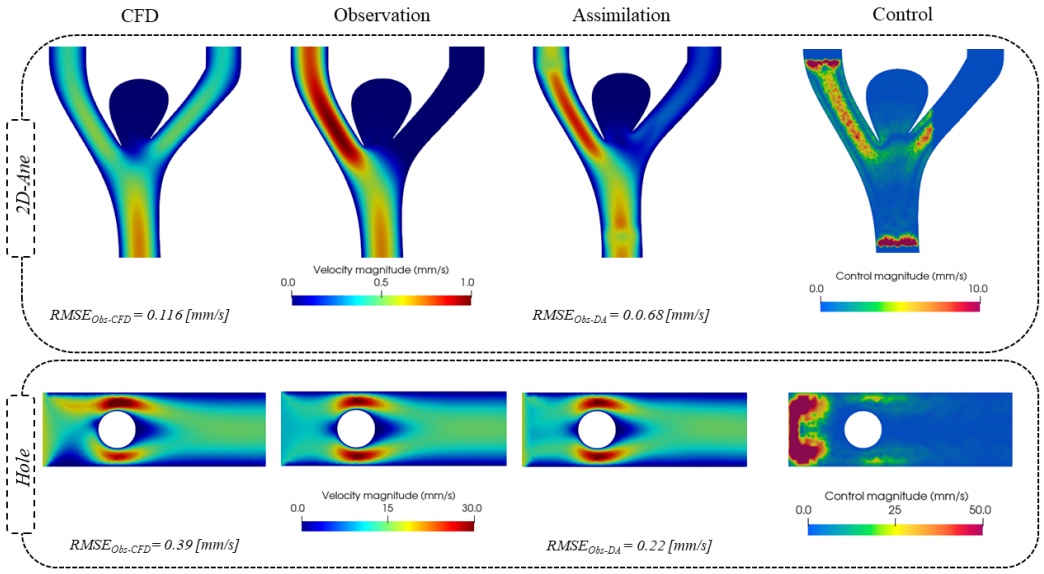

Figure 14: Data assimilation in 2D experiments assuming a regularisation parameter $\alpha = 10^{-4}$. Comparison among assimilation solution, observation and CFD (solution at $it = 0$) in*2D-Ane* (first row) and *Hole* (second row) experiments with a representation of the control variables along the domains.

3DVar

The 3DVar formulation was applied all over the 3D domain to reconstruct blood flow at the highest flow rate time frame of the 4D flow data. A good agreement was found between the assimilated velocity and the 4D flow measurements at the last optimisation iteration as shown in Fig. 15. According to the 2D experiments, the control variable (Fig. 15) acted mostly over a restricted region of the domain. As expected, the 3DVar enabled to augment the spatial resolution in the observations. Nevertheless, the peculiar 3DVar formulation here implemented allowed augmenting also the temporal resolution of 4D flow acquisition. Indeed, by formulating the optimization problem as time-dependent, the DA was performed for each Navier-Stokes time iteration, increasing temporal information between two consecutive 4D flow time frames. In Fig. 16, the 3DVar was compared with the 4D flow based-CFD (High-resolution CFD) carried out in SimVascular. Although, the velocity colour map for the High-resolution CFD appears smoother and well-defined, the predicted flow patterns are consistent with 3DVar and both techniques captured vortex formation within the aneurysm in accordance with 4D flow. The RMSE of the velocity magnitude with respect to the 4D flow reported in the figure, highlights that the 3DVar solution is closer to the observation than high-resolution CFD. Overall, the flow field obtained with 3DVar, is close to both 4D flow measurements and high-resolution CFD.

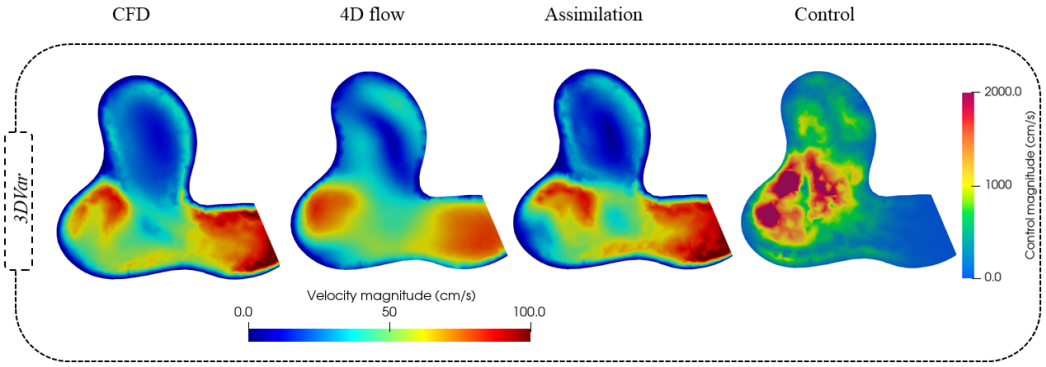

Figure 15: Comparison of the assimilated solution in the 3D model with the 4D flow and the CFD (solution at *it=0*) by velocity contour maps along a cross-sectional plane of the aneurysm. Representation of the control magnitude along the same cross-sectional plane.

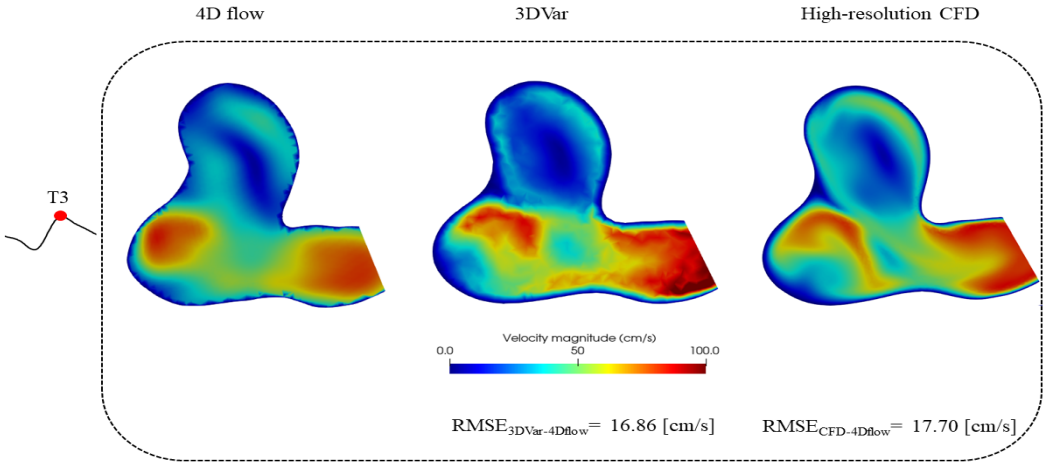

Figure 16: Velocity contour map extracted from a cross-sectional plane of the aneurysm for 4D flow, 3DVar and High-resolution CFD with RMSE of the velocity magnitude for 3DVar and High-resolution CFD against the observation (4D flow)

Discussion and conclusions

As already shown in the previous sections, intra-aneurysmal hemodynamics evaluation is crucial in IA risk stratification. Blood flow assessment can be performed by numerical simulations, or by imaging techniques. However, both approaches have limitations which may hamper their clinical application. DA is an innovative mathematical approach which enables to combine numerical simulations with 4D flow measurements, improving the quality of blood flow prediction and hemodynamic assessment. In this work, a heuristic 3DVar formulation

was implemented and evaluated in reconstructing blood flow in an IA model from 4D flow measurements. Together, the role of 4D flow guided-numerical models in IA hemodynamic assessment was investigated. The efficacy and the accuracy of the implemented 3DVar in estimating intra-aneurysmal hemodynamics were evaluated against the 4D flow guided-CFD results.

4D flow guided-CFD and FSI simulations: IA hemodynamics

CFD and FSI simulations proved to be reliable methods for reconstructing blood flow by a qualitative and quantitative comparison with 4D flow data (Maximum accuracy of $\sim 85\%$ in velocity magnitude). The maximum accuracy was higher than those one reported in [19] and [20], confirming the high performance of the correction strategies [19] adopted here for the 4D flow.

The NonUniform-FSI results did not yield relevant additional information in velocity field prediction with respect to CFD. Even if the displacement of the aneurysm wall was significant (maximum displacement 0.042cm at peak flow) and consistent with previous works [16, 17] the velocity profile was only marginally affected. Contrastingly, in [16] the intra-aneurysmal velocity profile looked different assuming a deformable wall. This disagreement may be related to the limitations of coupled-momentum method FSI implemented in SimVascular. Here, the geometry problem related to the vessel motion is not solved, assuming the vessel wall as a thin membrane strongly coupled to the fluid boundary in order to reduce the computational cost. Another explanation for the low impact of wall deformability on the intra-aneurysmal velocity profile may be related to the size and shape of the aneurysm, as reported in [15].

Nevertheless, the FSI simulations (Uniform- and NonUniform-FSI) highlighted the damping effect of blood flow due to the wall deformability, computing a lower maximum pressure difference than CFD, along the aneurysm surface. As already mentioned, the displacements field obtained with Uniform-FSI (Max displacement= 0.042cm) was consistent with [16] (Max displacment= 0.035cm). In NonUniform-FSI, the displacement magnitude on the aneurysm wall doubled with respect to Uniform-FSI in accordance with [17] where the same wall thinning model was adopted. The WSS contour map around the aneurysm was extracted only from the CFD results. The maximum WSS computed along the aneurysm wall was $\sim 6\%$ higher than that one reported in [38] and in perfect accordance with [39, 40]. Moreover, the WSS distribution found may explain the aneurysm location. Indeed, the aneurysm protrudes from a region affected by high WSS, generally associated to the initiation and growth of IAs [41].

2D and 3D variational DA

The novelty of the variational DA approach implemented here lies in its formulation. In the previous works [28, 29, 30], the Var DA aimed at recovering optimal inlet or outlet boundary conditions from the measurements. Contrastingly, in this work the data assimilation was carried out by controlling a fictitious source term added to the Navier-Stokes formulation. The fictitious source term forced the blood flow in following a reference solution. In the 2D numerical experiments, the quality of DA worsened for regularisation parameter $\alpha > 10^{-2}$ as obtained in [30]. However, the numerical artifacts introduced by the control for $\alpha = 10^{-4}$ suggest the risk of overfitting the observation when the Var DA is applied on a restriction of the domain.

The 3DVar was implemented for steady-state blood flow simulations and performed over the entire flow domain in reconstructing blood flow from 4D flow measurements. In 3DVar, the optimisation algorithm implemented in the `dolphin-adjoint` library failed due to the drastically increased dimensionality concerning the 2D experiments. The optimisation algorithm was the same used by Funke et al. [30] in the 4DVar implemented for transient blood flow. However, the optimal control applied here was dimensionally larger and hence computationally more expensive in the optimisation procedure. Nevertheless, the ad-hoc gradient descent optimisation algorithm provided a sufficient functional minimisation and the good agreement found between the assimilated solution and the observations confirmed the robustness of the implemented 3DVar formulation in reconstructing blood flow from 4D flow data. The approach enabled noise reduction and super-resolution in 4D flow measurements. Notably, the peculiar 3DVar formulation implemented here allows also augmenting arbitrarily the 4D flow temporal resolution by freely choosing the number of the Navier-Stokes time iterations to perform in the constrained optimisation process.

3DVar and High-resolution CFD in reconstructing blood flow in IAs from 4D flow data

3DVar allowed obtaining a better agreement with 4D flow data than High-resolution CFD (4D flow based-CFD) within the region of interest even on a coarser mesh (700K vs 1.3M elements), quantified by a lower RMSE of the velocity magnitude ($\sim -5\%$). In general, the reliability of blood prediction provided by 4D flow based-simulations relies on sufficient mesh refinement, reliable vessel wall modelling (in case of FSI simulations) and a correct calibration of outlet BCs which depend on pressure measurements scarcely available in cerebral arteries.

On the contrary, 3DVar has proved to be a valid method to increase numerical models accuracy in assessing blood flow in IA, exploiting entirely the 4D flow measurements.
Additionally, the 3DVar here was limited only at the highest flow rate time frame. However, by extending the approach over all the 4D flow data-set, it could be possible to reconstruct blood flow dynamics for all the cardiac cycle.

Conclusion

In conclusion, this work investigated the role of 4D flow based-CFD and FSI in assessing IA hemodynamics and proposed a heuristic 3D variational data assimilation approach to reconstruct the flow conditions in a real IA from 4D flow data. The proposed method has proved to be efficient in combining 4D flow MRI with CFD guaranteeing a better accuracy in blood flow prediction than 4D flow based-CFD analysis. This method is attractive in hemodynamics assessment of those vascular regions where models parameters, such as pressure estimations or vessel wall properties, are scarcely available, given its dependency only on 4D flow acquisitions. To the best of the author's knowledge, this is the first 3DVar formulation of this kind. It represents an effort towards an efficient merging of numerical modelling and 4D flow measurements, which will ultimately lead to more accurate risk stratification for vascular diseases such as IAs.

Chapter 1

Clinical background and numerical approach

In this chapter an overview on the anatomy, physiology and pathologies of cerebral circulation will be given. Attention will be focused on intracranial aneurysms, their clinical evaluation and their surgical treatment. In the last sections an insight on numerical methods and data assimilation will be given.

1.1 Cerebral Circulation: Anatomy of Circle of Willis

The cerebral circulation can be divided in anterior and posterior circulation. The anterior circulation is fed by the bilateral internal carotid arteries (ICAs) which run cephalically through the neck and into the brain. In the brain each ICA individually gives off an ophthalmic artery and then carries blood in the anterior and middle cerebral arteries (ACA, MCA). The vertebral arteries (VAs) supply the posterior cerebral circulation. The VAs ascend in the posterior neck, they pass through the dura mater at the level of the first cervical (C1) vertebrae and fuse themselves in the basilary artery (BA). The BA supplies the anterior inferior cerebellar arteries, the brainstem perforators, the superior cerebellar arteries, and finally the posterior cerebral arteries (PCAs). The anterior and posterior circulation are bridged anteriorly by the anterior communicating artery (AcoA), which connects the bilateral ACAs, and posteriorly by the posterior communicating arteries (PcoAs) which connect the bilateral ACA-ICA junctions with the PCAs. This ring of vessels forms the Circle of Willis (Fig. 1.1).

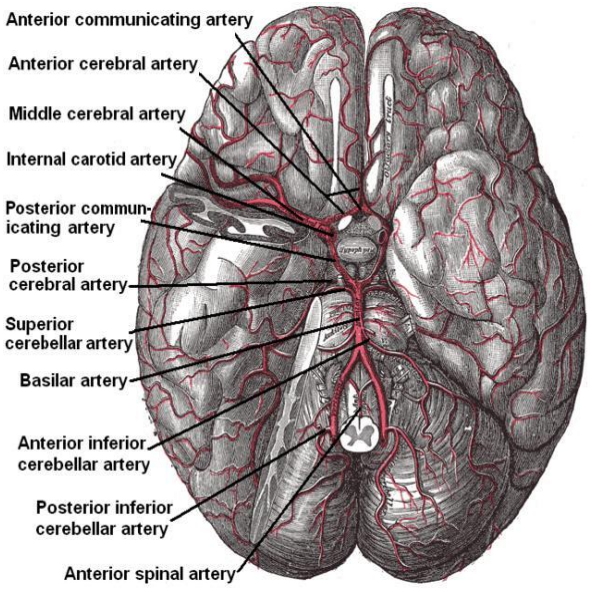

Figure 1.1: The brain arteries at the base of the brain. Circle of Willis is formed near center. Inferior aspect. [44]

Circle of Willis (CoW) acts to provide collateral blood flow between the two circulations of the brain protecting against ischemia in the event of vessel disease or damage in one or more areas [44].

Actually, several variants of CoW exist and only the 24% of individuals have a complete CoW [45]. Commonly CoW reaches its final arrangement at the 6-7 weeks embryological stage. Anyway, the multiple events that occur during embryological stage might lead to a diverse spectrum of vascular anatomical variants. Duplicated, fenestrated, hypoplastic or absent vessels are the most common physiological variants. Duplication occurs when two distinct vessels fuse together into a single vessel; fenestration is similar to duplication but in this case a single vessel split into two channels which then fuse back together, restoring the primary vessel. Duplication and fenestration are the second most common variant in cerebral vascular anatomy and are mainly reported in the anterior circulation. Hypoplasia is the first most recurrent anomaly reported in CoW [44]. A cerebral artery is considered hypoplastic if its size is smaller than normal. PcoA is the artery typically affected by hypoplasia and generally the posterior circulation is the most likely to have hypoplastic arteries [44]. It is to be noted that these cerebral arterial variants might be pathological or might work together with other vascular risk factors in promoting atherosclerosis and brain saccular aneurysm. For example, fenestrated or duplicated aneurysm were found associated with the development of saccular aneurysm. Probably this association can be explained by the arterial wall weakening which occurs in this context due to the lower quantities of smooth muscle cells and collagen at the

proximal and distal end of the duplicated segment [46]. Nevertheless, saccular aneurysms are more likely to be found near vessel bifurcation than anomalous cerebral vessels (hypoplastic or fenestrated vessels) [47]. This may suggest that hemodynamics has a major role in aneurysm development.

The cerebral vasculature presents a structural difference with respect to systemic arteries. In cerebral arteries the common division in three distinct histological layers can still be identified. However, unlike systemic arteries, cerebral arteries do not have an external elastic lamina, but a more developed internal elastic lamina; cerebral arteries present fewer elastic fibers within the middle layers and a very thin adventitia [48]. These structural differences make the cerebral vasculature more inclined to develop pathologies such as aneurysm [48]. The lack of some components within the wall layers weakens the cerebral vessels which is not able to withstand the stresses produced by the flowing blood, sometimes emphasized by anatomical or endogenous (i.e. atherosclerosis) factors [49].

1.2 Cerebral Circulation Pathologies: Intracranial Aneurysms

Cerebral or intracranial aneurysm (IA) is a cerebrovascular disorder in which a weakening of the inner muscle layer of the blood vessel causes an abnormal dilatation or ballooning [1]. The worldwide prevalence of cerebral aneurysms is 3.2%, with a mean age of 50 and an overall 1:1 gender ratio [2]. After the fifth decade of life this ratio changes significantly as the female gender is at higher risk of developing cerebral aneurysms. Indeed, the decreasing in circulating estrogen causes a reduction of collagen amount in vessels walls [2].

The rupture of cerebral aneurysms leads to subarachnoid haemorrhage (SAH), a relevant health problem with an approximate incidence of 9 per 100,000 and a mortality rate of about 60% within the first 6 months [2]. Anyway, the large majority of intracranial aneurysms never rupture. As it is mentioned in the guidelines of the American Heart Association for the management of patients with unruptured intracranial aneurysms, only 0.25% of the total diagnosed unruptured aneurysms will rupture causing SAH [3].

Most of the unruptured cerebral aneurysms are silent and often do not cause any symptoms. In case of rupture the SAH starts bleeding into the subarachnoid space (the space between the Pia mater and Arachnoid mater, i.e. the two innermost membrane layers which surround the brain) causing severe headache, decreased level of consciousness and vomit. High risk of rupture is associated with aneurysm over 10 mm [3]. Nonetheless, dimension alone is not a

reliable parameter for the valuation of cerebral aneurysm risk of rupture [3].

1.2.1 Aneurysm Classification

Cerebral or intracranial aneurysms (IAs), can be differentiated in ruptured and unruptured aneurysms; the latter can either be asymptomatic or symptomatic. Usually, ruptured aneurysms are discovered because cause of SAH while the unruptured aneurysms are often found incidentally because of symptoms unrelated to the aneurysm. Beside this overall differentiation, cerebral aneurysm can also be classified based on shape, angioarchitecture (relationship with adjacent vessels) and location, morphology, and current status [50].
Based on shape, intracranial aneurysms can be saccular or fusiform (Fig. 1.2). Saccular aneurysms arise from the side wall of the vessel creating a balloon shape dilatation with a narrow neck. Fusiform aneurysms instead, bulge out from all side (circumferentially) forming a dilated vessel. Saccular aneurysms are the most frequent, representing the 90% of all intracranial aneurysms [51].

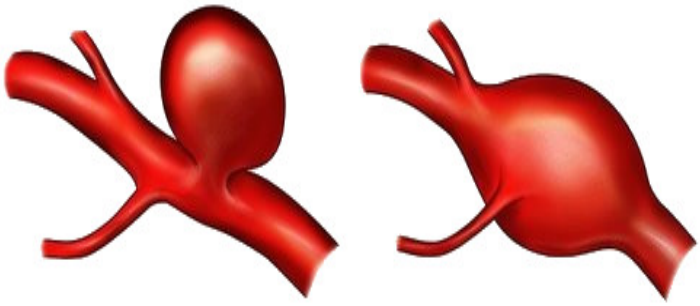

Figure 1.2: Saccular (right) and fusiform (left) aneurysms. [52]

Following the classification proposed by Pritz et al. [50] saccular aneurysm can be further classified in three more groups based on angioarchitecture. The first group are those not associated with a branch vessel (No branch vessel aneurysms). The second group are those associated with a side-branch vessel (side-branch aneurysms). The third, are those occurring at a bifurcation (bifurcation aneurysms). No branch vessel aneurysms usually occur at the major conducting vessels, namely the internal carotid artery and the vertebral artery. Side-branch aneurysms are commonly found on side branches associated with major conducting vessels in both anterior and posterior circulation. Bifurcation aneurysms can be found in both posterior and anterior circulation, at the bifurcations with the major conducting vessels (internal carotid artery and basilary artery) and the bifurcations with the primary

vessels (anterior communicating artery region or middle cerebral artery bifurcation).

Specific morphological parameters were defined to characterize ruptured and unruptured cerebral aneurysms. Beside aneurysm size, defined as the maximum distance of the dome from the aneurysm neck plane, four more parameters are commonly used in the clinic: aspect ratio (AR), size ratio (SR), flow angle (FA) and height-width ratio (H/W). AR is defined as the maximum perpendicular height of the aneurysm divided by the average neck diameter of the aneurysm. SR is defined as the maximum aneurysm height divided by its average diameter. FA is defined as the angle between the maximum height of the aneurysm and the parent vessel. Finally, H/W is defined as the ratio between the maximum height and the width of the aneurysm (Fig. 1.3). Numerous studies analysing the morphological characteristics of intracranial aneurysm have demonstrated that these parameters are associate with aneurysm rupture status [4]. In particular, Ujiie et al., examining 129 angiographic images of ruptured aneurysms and 78 of unruptured aneurysms, found that AR was predictive of aneurysm rupture in almost 80% of the subjects [53].

Unruptured aneurysms can be also classified depending on their status during follow-up in growing or stable aneurysms. Growing aneurysms have a higher risk of rupture. [54].

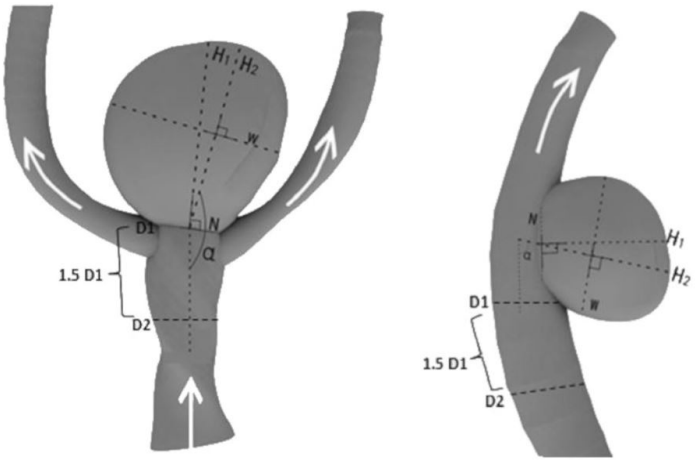

Figure 1.3: Definition of the morphological parameters in end-wall aneurysm (right) and side-wall aneurysm (left). Aneurysm size is defined as the maximum distance of the dome from the aneurysm neck plane (N). Aspect Ratio: AR = H1/N. Size Ratio: SR = H2/((D1 + D2)/2). Flow angle: FA = α. Height-width ratio: H/W = H2/W [4].

1.2.2 Risk Factors For Aneurysms Development And Rupture

In the last years, unruptured aneurysms have been discovered incidentally with an increasing frequency because of the widespread use of imaging techniques. For this reason,

more attention has been paid to the definition of aneurysm risk factors to guide healthcare specialists for decision making and for determining the best course of action when an unruptured aneurysm is found.

The American Heart Association and the European Stroke Organization have used systemic literature reviews in order to write down guidelines for the management of patients with intracranial aneurysms [2, 3]. According to both guidelines, aneurysm risk factors can be divided into factors associated with 3 phases:

- Risk for aneurysm development
- Risk for growth or morphological change
- Risk for rupture

For aneurysm development non-modifiable risk factors such as age and sex were found to have an important incidence in both guidelines. Prevalence studies have demonstrated an increasing frequency of intracranial aneurysms by age, with a peak in the fifth and sixth decade of age. Moreover, across the age spectrum there is an increasing frequency in women compared with men. In both guidelines family history of intracranial aneurysm increased the risk of aneurysm development. Excessive alcohol consumption, cigarette smoking and untreated hypertension seem to be the main modifiable risk factors for development of cerebral aneurysms [2, 3].

European and American guidelines identify cigarette smoking and female sex as independent risk factors for aneurysm growth. According to recent findings, growing (unstable) aneurysms have high propensity to rupture. Increased blood pressure, hemodynamic stress based on location, aneurysm shape, aneurysm size and inflammation are other risk factors for aneurysm growth as it is showed in the American guidelines.

From the comparison between ruptured and unruptured aneurysm data, according to both guidelines, cigarette smoking, age and hypertension seem to have a high impact in determining aneurysm rupture [2, 3]. Moreover, the combination of size and location differences, characteristic morphology and hemodynamic may influence the aneurysm risk of rupture. For example, anterior communicating artery aneurysms were found more likely to rupture than middle cerebral artery aneurysms. Maximum aneurysm diameter ($>$ 7mm), high AR, SR, bottleneck shape combined with hemodynamic features have been demonstrated to be

discriminatory between ruptured and unruptured aneurysms [3]. Anyway, it is still unclear how these factors can be effectively applied to health-care of individual patients.

1.3 Clinical Evaluation

In case of suspect of ruptured or unruptured IA the diagnosis is usually confirmed by an imaging evaluation, such as Digital Subtraction Angiography (DSA), Computed Tomography Angiography (CTA) or Magnetic Resonance Angiography (MRA) [3].

DSA represents the gold standard for aneurysm diagnosis. It guarantees high sensitivity, especially in detection of small aneurysms (diameter less than 3 mm). Despite its benefits, DSA may have complications due to its invasiveness and contrast-related events [3]. The invasiveness and the cumulative radiation dose make it less frequently used for follow-up, even if low risks have been confirmed for selective DSA follow-up for treated aneurysms [55, 56].

CTA is a contrast-based imaging technique, less sensitive to small aneurysms (diameter less than 3 mm), but also less invasive compared to DSA. Additionally, CTA is suited to identify mural calcification and thrombus, which can have a great impact in treatment decision [57], but true neck/dome/adjacent small vessel anatomy may not be accurately depicted depending on the reconstruction method [58]. Finally, its application in follow-up imaging can be limited by artifacts from bone and metal (coils, stent, and clip) in treated aneurysms.

MRA imaging of aneurysm is typically performed using time-of-flight (TOF) or contrast methods. In MRA imaging the aneurysm size highly affects the results. The sensitivity of this method is lower than DSA and CTA, and as a primary method of screening of unruptured aneurysms, MRA can be effective for aneurysms larger than 3 mm [59]. Despite these drawbacks the non-invasiveness and the absence of radiation make MRA an effective alternative to CTA and DSA for non-invasive follow-up of both treated and untreated aneurysms. However, with treated aneurysms, the resulting susceptibility artifacts on MRA can cause an underestimation of the size of the residual or recurrent aneurysm, and formal DSA may be necessary to determine the need for retreatment.

Imaging-based diagnosis is crucial for aneurysm risk stratification, which relies predominantly on aneurysm characteristics (size, location, and morphology) and patient factors. The assessment of aneurysm risk of rupture is important in determining the method of treatment, including conservative management, endovascular, surgical, or combined therapy. In the

last years, special attention has been paid to the analysis of intra-aneurysmal hemodynamic factors in order to improve prediction of aneurysm rupture risk and gain a more comprehensive understanding of the biomechanics underlying the pathology. Four-dimensional (4D) magnetic resonance imaging (MRI), or 4D flow MRI, is an emerging, non-invasive technique used for the assessment of blood flow, and which can be used to study aneurysm hemodynamics.
Given the important role of 4D flow MRI for this thesis project, the following paragraph is completely devoted to this topic.

1.4 Magnetic resonance imaging

Before describing the 4D flow MRI, a brief description of main physical principles of MRI may be useful.

1.4.1 Magnetic resonance imaging basics principles

MRI is a medical imaging technique that allows to obtain images of a specific district's internal anatomy. It does not use ionizing radiation as other imaging techniques (CT and X-rays) [60], rather it uses magnetic fields and radio frequencies. The magnetic field generated by MRI machine is measured in Tesla (T). The majority of MRI systems used in clinical practice produce magnetic fields ranging from 1.5T to 3T, even if the most modern equipment can reach a magnetic field above 7T. MRI relies on the magnetic properties of hydrogen atoms (protons) which are abundant in soft tissues containing water. Hydrogen proton produces a magnetic moment, spinning about its axis (Fig. 1.4a). When no external magnetic field is applied, protons magnetic moment is oriented randomly. The MRI system is made of 4 main components: a primary magnet, gradient magnets, radiofrequency (RF) coils and a computer system. The acquisition of a MR image can be summarized in 4 steps:

1. The primary magnet generates a constant magnetic field (B_0) which causes the proton spins to align either parallel or antiparallel to it. More spins align in a parallel configuration which corresponds to a low energy state. This results in creating a net magnetic vector (M_0) in the direction of B_0 called longitudinal magnetization (Fig. 1.4b). The proton spins, however, are not static, but precess in synchrony around the direction of B_0 with a specific frequency, called Larmor frequency, which depends on

the strength of the magnetic field.

2. The gradient magnets then generate a secondary alternating magnetic field over the primary field, called radiofrequency (RF) pulse. The arrangement of these magnets allows MRI to image directionally along different perpendicular directions, and hence for 3D spatial encoding. The RF pulse switches protons in a low energy state into a high energy state, decreasing the net longitudinal magnetization and synchronize them making precess in phase. As a result, the net magnetization vector turns 90° from the primary field towards the transverse plane (transverse magnetization).

3. After the RF pulse, relaxation occurs, and protons resume the original state in the primary magnetic field. Some protons switch back from a high energy state to a low energy state, releasing energy to the lattice (spin-lattice, or T1, relaxation). Together, protons that were in phase begin to dephase (spin-spin, or T2, relaxation). As results the net longitudinal magnetization increases and the net transversal magnetization decreases.

4. The net magnetic vector, sum of the two, spirals around the longitudinal axis changing its net magnetic moment. This phenomenon induces an electrical signal that is received by the RF coils and is later analyzed and converted to a digital signal by the computer system.

Finally, images are reconstructed from digital signal by applying Fourier transforms. MRI datasets can then be stored in a standard format called DICOM.

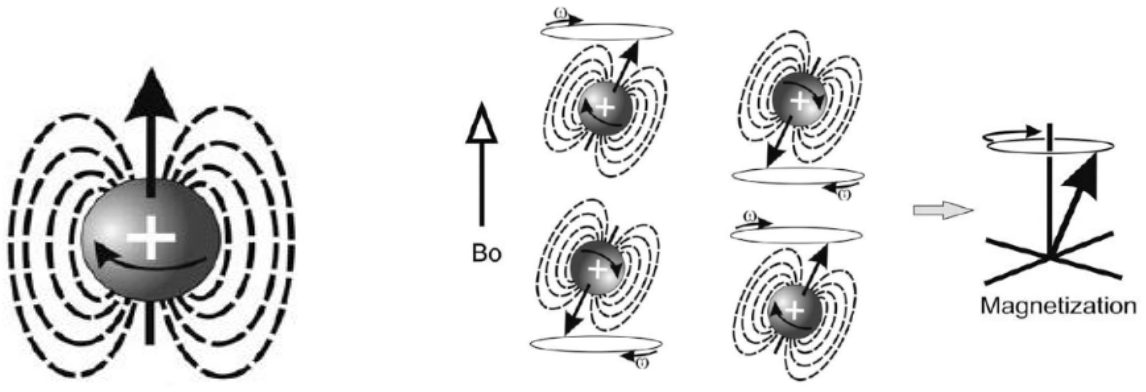

(a) (b)

Figure 1.4: Schematic representation of protons magnetic properties (a). Parallel and antiparallel proton configurations when an external uniform magnetic field B_0 is applied. A net magnetic vector is created (b) [60].

1.4.2 PC-MRI basic Principles

Phase contrast MRI (PC-MRI) is a method of obtaining quantitative information on pulsatile blood flow in the human vascular system. The basic principle relies on magnetic moments (spins) moving along an external magnetic field gradient which acquire a difference in the phase of their rotation, whereas non moving spins do not [61]. By applying a sequence of two inverted bipolar gradient, along a specific spatial direction, the phase shifts induced by other sequence parameters are eliminated, leaving only phase shifts due to spins movement (Fig. 1.5).

The phase difference $\Delta\Phi$ acquired in the two interleaved measurements can be then calculated:

$$\Delta\Phi = \gamma(\Delta M v) \tag{1.1}$$

where γ is the gyromagnetic ratio, ΔM is the gradient moment difference and v is the spin velocity along the direction of encoding gradient. From 1.1 the velocity value can be computed as:

$$v = \frac{VENC}{\pi}\Delta\Phi \tag{1.2}$$

where VENC (Velocity Encoding) value determines the range of detachable velocities encoded by a phase contrast (PC) sequence. The VENC value is a parameter which has to be set before the acquisition. It should be equal to 1/3 of the expected peak velocity (V_{max}) in order to avoid aliasing. Noise in a velocity image σ is determined by VENC and signal-to-noise ratio (SNR) of the magnitude images:

$$\sigma \sim \frac{VENC}{SNR} \tag{1.3}$$

Therefore, VENC must be properly evaluated in order to avoid aliasing and reduce the noise which can affect peak velocity V_{max} estimation.
Beside aliasing and noise occurrence, velocity estimation of blood flow can be affected by heart and lungs motion. To overcome this issue, prospective or retrospective cardiac gating are employed. In prospective gating the data acquisition is triggered to start when systole occurs and end when diastole occurs by the electrocardiogram (ECG) signal. In the retrospective gating, instead, the acquisition is performed all over the ECG and the measured blood

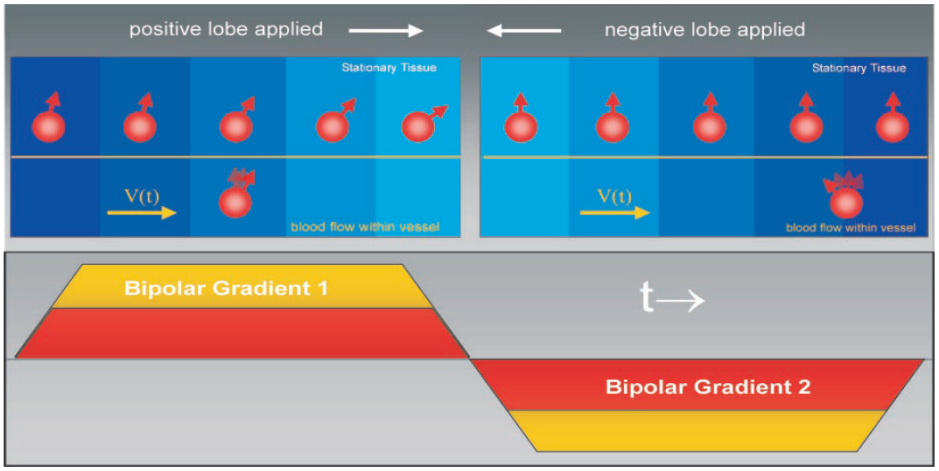

Figure 1.5: Principle of PC-MRI. Sequence of two inverted bipolar gradient is applied. Flow encoding is achieved by means of the difference in the bipolar gradients of the two acquisitions [61].

velocities are an average over multiple cardiac cycles. Motion artifacts due to respiratory movement can also be accounted for. In case of prospective gating, the patient is asked to hold his breath, while patient's diaphragm motion is recorded and successively accounted for in retrospective gating.

1.4.3 4D Flow MRI

PC-MRI allows to measure blood flow along the direction of applied bipolar gradient. Flow measurements are usually acquired positioning the imaging plane perpendicularly to the vessel of interest and using a through-plane flow encoding (2D PC-MRI). When applying velocity encoding bipolar gradients along all three flow directions and accounting for three-dimensional (3D) anatomic coverage, time-resolved (CINE) PC-MRI is also termed as 4D flow MRI [5].

In both 2D and 3D CINE PC-MRI, the acquisition cannot be performed during a single heartbeat due to time constraints and phase contrast data are collected over several cardiac cycles. To account for heart motion ECG-gated k-space segmented data acquisition is used to synchronize the measurement with the cardiac cycle. Each heart beat is divided in sub intervals (time-frame) and during each sub intervals only a subset of all required phase-encoding steps are measured. The procedure is repeated until the full raw dataset is acquired [5]. At the end of the acquisition, a magnitude image representing the anatomy and three phase difference images, one for each velocity component encoded, will be obtained for each time frame (Fig. 1.6).

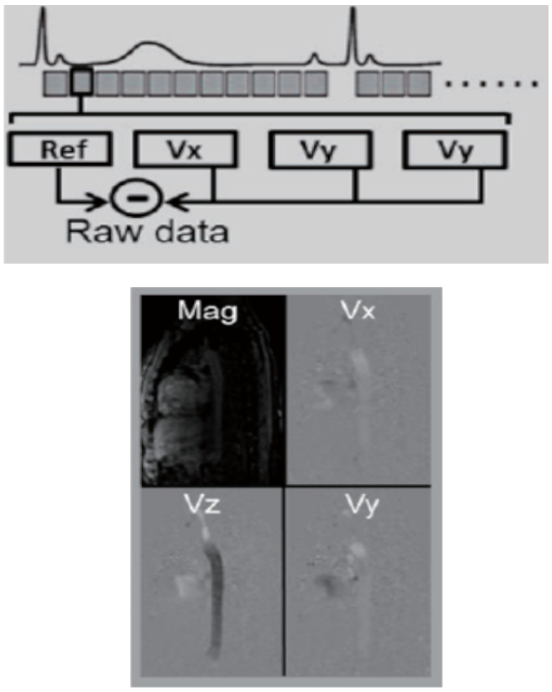

Figure 1.6: Schematic illustration of data acquisition in 4D-Flow MRI. For each time frame, four raw datasets are collected, one reference scan and three velocity-encoded acquisitions. A magnitude image and a three phase difference images of a thoracic aorta are reported. Image adapted from [5].

4D flow MRI allows for 3D blood flow visualization in the anatomical district of choice and for retrospective quantification of flow parameters. During data analysis 3D streamlines can be generated in order to visualize the spatial distribution and orientation of blood flow velocities in a specific time frame. Generally, peak systolic 3D streamlines are used to identify outflow jets or helix flow. Less frequently, time-resolved pathlines are used to visualize temporal evolution of 3D blood flow over one or more heartbeats [62]. Color-coding of these traces allows for the visualization of velocity changes in the anatomy. In contrast to traditional 2D CINE PC-MRI, 4D flow MRI enables the retrospective quantification of hemodynamic parameters at any location within 3D data volume [63]. With 4D flow MRI, peak and mean velocities, total flow, net flow or retrograde flow can be calculated. Moreover, additional hemodynamic parameters, such as wall shear stress (WSS) or pressure difference can be computed from PC data [62].

Unfortunately, 4D flow MRI still has some limitations which hamper its application in some human districts and in life threatening situations. As mentioned in the previous paragraph PC-MRI can be heavily affected by noise and aliasing if a not suitable VENC is set before acquisition. Heart motion and respiration can introduce imaging artifacts, making cardiac and respiration gating necessary, thus increasing acquisition time. In addition to these drawbacks,

4D flow MRI has limited temporal resolution, which does not allow for capturing rapid variation in flow, and limited spatial resolution, which adds partial volume effects causing an underestimation of the flow and peak velocity [61]. PC measurements are weak for accelerated flow limiting the application of 4D flow MRI in high Reynolds flow districts. Phase offset errors due to eddy currents, Maxwell terms, and gradient field non linearity are frequently encountered inaccuracies which long the image reconstruction process and the data analysis workflow.

1.4.4 4D flow-based studies on IA

Despite these current limitations, 4D flow MRI has been effectively applied for the assessment of arterial and venous hemodynamics in various anatomic regions in the human body [5]. Several studies demonstrated the feasibility of 4D flow MRI to identify hemodynamic properties in IA [6, 7, 8]. Some studies focused on flow pattern and looked for an association between morphology, hemodynamics, and growth. They found that flow distributions, WSS, vorticity, and peak velocity are highly differentiated between saccular and fusiform aneurysms, and between large and small aneurysms. Narrow, high-velocity jets along the aneurysm wall were found in saccular aneurysms, while fusiform aneurysms were characterized by slow-flow channel within the entire lumen. WSS, vorticity, and peak velocity were greater in saccular than fusiform aneurysms, and WSS was inversely correlated with aneurysm size [6, 64]. 4D flow MRI has also been used for evaluating aneurysmal endovascular treatment outcomes of stent-flow diversion [65, 66]. Nevertheless, low spatial and temporal resolution is a significant limiting factor for 4D flow, particularly in the computation of WSS and the other hemodynamic indexes associated with it, which seem to have a crucial role in the development and rupture of cerebral aneurysms [42]. The velocity sensitivity (VENC) may also hamper the ability of 4D MRI to capture the full spectrum of flow velocities circulating within the aneurysm. Schnell et al. argued that a dual-VENC encoding protocol could overcome this limitation [67].

1.5 Treatments

Intracranial aneurysms are treated surgically by clip occlusion (clipping) or in a less invasive way by endovascular coiling [3] (Fig. 1.7a 1.7b).

Before aneurysm clips development, bypass or aneurysm wrapping with muscle tissue were the

usual surgical treatments to prevent the rupture of unruptured aneurysms or the rebleeding of ruptured aneurysms. With the invention of detachable platinum coils by G. Guglielmi in 1990, endovascular aneurysm treatment with coiling has been proved to be a valid alternative to surgical clipping [3]. Although its lower invasiveness, coiling is not always preferred to clipping and the choice between the two therapeutic approaches depends on age of the patient, morphology and location of aneurysms, experience of the surgeon and other intraoperative factors.

(a) (b)

Figure 1.7: Surgical and endovascular treatments for intracranial aneurysm. Surgical clipping of the aneurysm neck (a). Endovascular coiling of the aneurysm sack (b) [68].

1.5.1 Surgical Therapy: Clipping

During microsurgical clipping, a small metal clip is used to stop blood flow into the aneurysm. A craniotomy is performed to create an opening in the skull to reach the aneurysm in the brain. The clip is placed on the neck (opening) of the aneurysm to obstruct the flow of the blood and remains inside the brain. In a recent clinical study, which reports on 9845 patients from 60 studies published in a time frame spanning 1990 to 2011, the authors found an overall mortality rate of 1.7% and a morbidity rate of 5% with an outcome estimation time up to 1 year after clipping surgery [69]. Consistent findings were showed in another study of the International Study of Unruptured Intracranial Aneurysms (ISUIA) carried out on 1917 patients after clipping for unruptured aneurysms. The authors found an overall mortality of 2.3% and a morbidity of 12.1% at 1 year after treatment [70]. In [70] potential cognitive impact of surgical treatment was also evaluated as a morbidity factor, since cognitive assessments of patients after clipping seemed to provide additional outcomes information [71]. It can explain the higher morbidity rate respect to [69]. The performance in occlusion rate is generally greater than 90% with the remaining almost equally divided in aneurysms incompletely occluded and aneurysms with neck remnants [69, 72]. Large (10-24 mm) and

giant (>25 mm) aneurysm are associated with a higher morbidity and mortality than small one (<10 mm). Anterior aneurysms are also more likely to rupture after surgical clipping than posterior aneurysms. Advanced age, symptoms associated to aneurysm particularly ischemic symptoms and general medical comorbidities are factors which negatively affect outcomes after surgical clipping increasing morbidity and mortality associated to the treatment [70, 72, 73, 74].

1.5.2 Endovascular Therapy: Coiling

Endovascular coiling is a minimally invasive technique, in which a catheter is passed through the groin up into the artery containing the aneurysm. Platinum coils are then released. The coils induce clotting of the aneurysm and, in this way, prevent blood from perfusing it.

Since the introduction of Guglielmi detachable coil, the portion of cerebral aneurysm undergoing endovascular treatment increased rapidly. The first clinical data available on the endovascular aneurysm coil occlusion, demonstrated the relative safety of this treatment [75]. Nevertheless, some studies showed an acceptable efficacy, intended as complete aneurysm occlusion, in a relatively small portion of patients [76]. Moreover, coiling failed frequently in treating aneurysm located in the middle cerebral bifurcation, and failure was more common in smaller (1-6 mm) than larger (7-15 mm) aneurysms [76]. Coiling treatment can be applied with adjunctive methods such as balloon remodelling or stent-assisted occlusion. These methods are commonly used in treatments of more aneurysms and an increased rates of progressive aneurysm occlusion have been reported with the use of stents. In general, from a cost-effectiveness perspective coil embolization of cerebral aneurysms was found efficacious in treatment of large (> 10 mm) or symptomatic aneurysms with less adverse outcomes, less in-hospital deaths and shorter hospital stays than surgical clipping. Anyway, endovascular treatment requires the use of x-ray fluoroscopy. This aspect can have an impact on the choice of which treatment to perform.

1.5.3 Clipping vs Coiling

To recap, endovascular coiling showed to have an advantage over surgical clipping, with better clinical outcome in terms of absolute risk reduction of death and severe disability after the treatment. However, the postoperative rebleeding risk seems higher in patients treated with coiling. The postoperative risk of rebleeding appears to be associated with the degree

of insufficient aneurysm occlusion leading to high risk of retreatment. Moreover, coiling is less efficient for bifurcation aneurysms and for aneurysms located on the middle cerebral artery. In general, as a rough guidance, aneurysms with a wide neck, small aneurysms, middle cerebral artery aneurysms, aneurysm in the anterior circulation and young patients should preferably be treated by clipping, while aneurysms with a small aneurysm neck, large aneurysms, aneurysms in the posterior circulation and elderly patients (>70 years) should be coiled [2, 3].

1.6 Numerical Models

Numerical models have proved to be valuable for simulating blood flow in several cardiac districts. Numerical approaches can be divided in 4 steps:

1. Define the physical problem to model;

2. Identify the major mathematical variables of the problem and derive a mathematical equation which links the relevant variables to the problem;

3. Choose the numerical schemes which enable to solve the equation;

4. Analyse critically the obtained numerical results;

In this context, the physical problem is describing the hemodynamics in human arteries. Local variations in hemodynamics have been proved to have an impact on development of several cardiovascular diseases, such as IAs [9, 10]. The problem of hemodynamics consists in assessing blood flow in human vessels. The principal quantities which describe blood flow are velocity and pressure. Knowing these fields allows the reconstruction of flow field for qualitative visualization and the computation of the stresses to which an arterial wall is subjected due to the blood movement. To model blood flow in large arteries, some hypothesis have to be made in order to formulate the problem correctly.
Firstly physiologic flow is transient. Blood flow is pulsatile, therefore one cannot neglect time by considering a "steady-state solution".
Blood is a body fluid which is composed by cells (red blood cells, white blood cells and platelets) suspended in the plasma. Therefore, blood cannot be considered as a homogeneous

fluid, even if in vessel bigger than capillaries (diameter larger than 8-10 μm) the discrete nature of blood can be discarded. Blood is a viscous fluid and its rheology depends on temperature and shear rate, defined as the derivative of velocity vector along the normal direction to the wall ($\frac{\delta u}{\delta n}$). This makes blood difficult to model and several approaches have been proposed to describe correctly this variable behaviour [77]. In most of the cases, viscosity (μ) is assumed constant, considering blood as a Newtonian fluid.

Another complex aspect to model is blood interaction with vessel walls. Blood vessels are hollow tubes with a multi-layers wall configuration, which deform under blood pressure. The deformability of vessel walls is relevant for large vessels and it affects the fluid flow. Generally, in numerical simulations the vessel wall is treated as rigid (Computational Fluid Dynamic (CFD) simulations). In order to account for fluid vessel interaction Fluid Structure Interaction (FSI) simulations can be performed. In some context, simulating the interaction problem can improve the reliability and the accuracy of the numerical results, although inevitably increasing the computational cost.

Lastly, boundary conditions must be provided at the domain boundaries. Normally, blood flow models are limited to a section of the cardiovascular system which can be reconstructed from medical images, such as CT or MR. For "artificial" boundaries, i.e. boundaries which truncate the space occupied by the fluid for computational reasons, the choice of BCs is often more delicate. The more classical BCs are applied stresses, or Neumann boundary condition, on the facet where flow goes out (outlet) and prescribed velocity, or Dirichlet boundary condition, on the facet where flow goes in (inlet). Realistic boundary conditions should be defined based on physical measurements, such as 4D flow MRI, to guarantee the reliability of the numerical results. For "physical or "wall" boundaries, since blood is a viscous fluid ($\mu > 0$), the "no slip" condition is the most commonly prescribed, which entails zero velocity in CFD simulations and coupling between blood velocity and wall velocity in FSI simulations.

Flow dynamics obey the Navier-Stokes equations (Eq. 1.4), a set of partial differential equations formed by the continuity equation and the momentum equations of fluids. They are valid on a fixed spatial domain Ω, representing the region within the fluid flows. The first equation derives from the principle of conservation of linear momentum, where the Cauchy stress tensor was linked to the kinematic quantities (pressure and velocity) by the constitutive law for a Newtonian incompressible fluid. The second one represents the principle of conservation of mass for a incompressible fluid.

$$\begin{aligned} \frac{d\mathbf{u}}{dt} + (\mathbf{u}\cdot\nabla)\mathbf{u} + \nabla p - \nu\Delta\mathbf{u} = \mathbf{f}, \quad \text{in } \Omega \\ \nabla\mathbf{u} = 0, \quad \text{in } \Omega. \end{aligned} \tag{1.4}$$

The unknowns are the velocity $\mathbf{u}$ and the scaled pressure $\mathrm{p} = \mathrm{P}/\rho$, where ρ is the density of the fluid. Since blood is an incompressible fluid, the first set of equations in Navier-Stokes model is divided by density, therefore $\nu = \mu/\rho$ is the kinematic viscosity (notice that the Eq. 1.4 was derived assuming ν constant). The Navier-Stokes equations must be supplemented by an initial condition (Eq. 1.5), which described the initial status of the fluid velocity, and by proper boundary conditions (BCs).

$$\mathbf{u}(\mathbf{x}, 0) = \mathbf{u}^0(\mathbf{x}), \quad \mathbf{x} \in \Omega. \tag{1.5}$$

The Navier-Stokes equations form then a set of partial differential equations (PDEs) which allow to reconstruct the velocity and pressure field within Ω. These equations cannot be solved exactly and numerical methods must be used. Proper numerical schemes must be selected to discretize the equations in time and space domain and solve them with the help of computers.

1.6.1 Numerical studies on intracranial aneurysms

Although unruptured IAs carry a relatively low risk of rupture, the high morbidity associated to SAH makes preventive interventions desirable. Moreover, both surgical and endovascular treatments carry a small but significant risk that can exceed the natural risk of aneurysms rupture [78]. For these reasons, improved risk stratification methods can be valuable for clinicians. Currently, prediction of aneurysm rupture relies on specific clinical and morphological parameters. Large aneurysm size, high aspect ratio, high size ratio and bottleneck shape are believed to be valid predictive parameters. However, the dynamics leading to aneurysm rupture are more complex and related not just to geometric, but also to specific hemodynamic features. For this reason, a comprehensive hemodynamycs evaluation could improve aneurysm risk stratification.

In the last decades, great attention has been paid to numerical models in order to extract hemodynamic information and relate them to the geometric measures commonly used in clinic, thus strengthening their role in IAs pathophysiology. In [11] distinct hemodynamics were found in low AR (< 1.8) and high AR (> 2.2) aneurysms in rabbits. Lower speed

flow, lower time averaged wall shear stress, lower wall shear stress at peak systole and higher oscillatory shear index denoted high AR aneurysms. In [79] the authors assessed that aneurysms shape and size cannot be used as independent rupture prediction factor since the parent vessel geometry can highly affect the hemodynamics within the aneurysm. High SR (>2) aneurysm morphology were found to be associated with multiple and complex flow patterns, confirming the influence of parent vessel geometry [12]. High SR was also found to be a discriminant factor between ruptured and unruptured aneurysms [43]. Moreover, in [80], hemodynamic simulations conducted on several aneurysms at different locations, showed distinct hemodynamic parameters distributions depending on cerebral regions, confirming that in some locations aneurysms rupture can be more frequent.

CFD allows analysing intra-aneurysmal hemodynamic in both qualitative and quantitative ways. Concentrated inflow jets, small impingement regions, complex flow patterns, and unstable flow patterns have been correlated with a clinical history of prior aneurysms rupture [14]. In two related works, Cebral et al. [13, 14], characterized a large series of IAs hemodynamic by patient-specific CFD. In [13] they found that unruptured aneurysms were more commonly characterized by simple stable flow patterns, large impingement regions, and large jet sizes, while ruptured aneurysms had disturbed flow patterns, small impingement regions, and narrow jets. The following work [14], was conducted on a larger sample size and confirmed the main findings of the previous one and reiterated the strong correlation between qualitative hemodynamic characteristics and aneurysm rupture.

For quantitative characterization of IA hemodynamic, several blood flow-related parameters have been proposed in the past years. Wall Shear Stress (WSS), Oscillatory Shear Index (OSI) and Pressure difference (PD) are the most frequent parameter associated to aneurysm status. WSS is a frictional force on the arterial wall produced by blood flow on the vessel wall, as described in the following equation:

$$WSS = \mu \left(\frac{du}{dy} \right)_{y=0} \tag{1.6}$$

where μ is the dynamic viscosity, u is the blood velocity and y is the distance from the vessel wall. WSS has been used to investigate aneurysm rupture, growth and initiation. Regarding aneurysm rupture, controversial results have been reported about role of WSS. High WSS were associated to aneurysm rupture in several studies [39, 40]. Increased WSS at thin aneurysmal wall area was involved with ruptured [81]. Flow impingement regions were

found associated with high level of WSS and believed as the area where the wall thinning starts [82]. Conversely, other works indicated low WSS as the main trigger for aneurysm rupture. Low values of WSS were found at the rupture sites, leading to the hypothesis that low WSS was the main responsible of the vessel weakening until the vessel could no longer sustain the arterial pressure [83, 84]. OSI is another blood flow-related parameter associated to IA rupture status which can be obtained from CFD and measures the directional change of WSS. High OSI values are usually associated with disturbed flow fields. It is defined as:

$$OSI = 0.5 \left(1 - \frac{\mid \int_0^T \mathbf{wss}_i dt \mid}{\int_0^T \mid \mathbf{wss}_i \mid dt} \right) \tag{1.7}$$

where $\mathbf{wss}_\mathrm{i}$ is the instantaneous WSS vector, t is time, and T is the duration of the cycle. In aneurysmal hemodynamic high value of OSI have been found in low WSS region and vice versa [85]. The controversial results on the role of WSS and OSI on aneurysm evolution is mostly due to the difference in the natural history of each analyzed aneurysm. Meng et al. [41] published a review article in which they distinguish the role of high WSS and low WSS during IA evolution. They associated high WSS at the blood flow jet impingement zone to the initiation of aneurysm. Then, they identify two different scenarios: if the WSS is still high, it causes degeneration of the cellular matrix and cell apoptosis, and aneurysm may rupture rapidly without reaching a large dimension. On the contrary, if WSS lowers, high OSI values associated with disturbed flow and low recirculation can trigger the inflammation process, increasing the aneurysm size.

PD is defined as the degree of pressure elevation at the aneurysm wall [86]. PD was showed to be related to aneurysm thin-walled regions considered as high risk condition for aneurysm rupture [87]. The role of pressure was also studied in aneurysm formation and growth. Doeinetz et al. [88] performed a CFD studied on basilary tip geometry before and after aneurysm formation. They found that local rise in wall pressure may initiate aneurysm formation, ballooning the vessel wall. This leads to a reduction of blood flow inside the vessel inflation, causing a decrease in WSS. Despite CFD has proven to be a powerful tool for assessing blood flow-related parameters, the rigid-wall assumptions limits the fidelity of this approach.

Accounting for vessel-blood interaction, thus performing FSI simulations, can increase the reliability of hemodynamic prediction. Few FSI investigations have been performed on patients specific aneurysms models [15, 16, 17, 18]. Reproducing patient-specific vessel wall

mechanics is a complex task, mainly because of the very low amount of data available on cerebral vessels. Wall thickness and material constitutive model should be correctly set based on *in vivo* measurements in order to guarantee accurate results. In [15], Bazilevs et al. compared CFD and FSI simulations in patient-specific IA models, showing that blood flow velocities within the aneurysm did not seem altered, while wall shear stress was found consistently overestimated in rigid wall simulations. Torii et al. investigated the influence of structural modeling [16] and wall-thickness [17] on FSI-based patient-specific assessment of cerebral aneurysm. High flow velocity and WSS distribution were seen to be independent of the constitutive wall model, i.e. hyper-elastic vs. linear elastic model. While, rigid wall simulations, performed as a comparison, yielded different flow patterns inside the aneurysm and higher WSS magnitude on the aneurysm wall [16]. Instead, in [17] larger wall displacements were observed in FSI simulations assuming a pathological wall thinning model around the aneurysm with respect to a uniform wall model. Consequently, the flow velocities in the aneurysm with the pathological wall model were lower, and that results in a reduction in WSS on the aneurysm wall. For this reason, modeling vessel wall thickness as uniform could hamper the reliability of aneurysm risk assessment. Accordingly, in [18] the impact of patient-specific wall thickness (non-uniform wall thickness) on FSI simulations in ruptured IA was assessed, revealing similar averaged wall stress on the aneurysm wall but a better correlation of stress distribution with rupture sites with respect to uniform wall thickness configuration.

Although numerical models are a valuable tool to analyze the hemodynamics within IAs, they rely on hypothesis and measurements (geometry reconstruction, blood model, BCs) that affect the reliability of the computation and may hamper their clinical implementation. The pursuit of patient specific BCs is the most challenging aspect in setting a numerical model for hemodynamic characterization. As it is showed in Sec. 1.4.2, PC-MR imaging is an innovative technique that enables measurements of blood flow and it provides high reliable velocity measures to apply as BCs for numerical models. Time-resolved 3D PC-MRI, also called as 4D flow MRI, can be used to measure hemodynamics within IAs (see Sec. 1.4.3). In [19, 20], 4D flow MRI was used to prescribe BCs for a CFD model of IA blood flow and to validate CFD results. Van Ooji et al. [19] found good agreement in flow features extracted from 4D flow MRI and computed with CFD in systole, while in diastole 4D flow measurements appeared inconsistent due to the low velocity-to-noise ratios. On the other hand, the relative difference in velocity magnitude was found lower in diastole. Similar findings were reported in [20]. In

[21], a complete review about research articles which used 4D flow MRI and CFD to compare the magnitude of WSS is given. The main goal of this review was to understand whether it is possible to achieve an accurate estimation of WSS from 4D flow in IAs, comparing it to CFD results (the goal standard for WSS estimation). Generally, 4D flow MRI-derived WSS was found lower in magnitude respect to CFD-derived WSS. Moreover, the level of agreement between 4D flow MRI and CFD-derived WSS magnitudes decreased at higher WSS values, while the relative distribution was found similar between the two techniques. The reasons for discrepancy are several and mostly related to 4D flow MRI limitations already described in Sec. 1.4.3. The low resolution limits the 4D flow in capturing the region of low and complex flow, which are precisely the region of most interest [22]. Increasing the resolution of 4D flow have the side effect to decrease the SNR which is already low in low flow regions [89] (for instance within the aneurysm). 4D flow MRI-derived WSS should account for reliable boundary conditions (inflow, outflow conditions and vessel motion) which are usually difficult to reproduce in numerical models and they are the main source of uncertainty for them. In [90] and [91], the effect of not accounting for vessel compliance in numerical simulations have been assessed, demonstrating that vessel distention is negligible in evaluating WSS in aneurysmal arteries. On the other hand, in [23] the authors supported that the rigid wall assumption in CFD simulations can lead to an overestimation of WSS. In conclusion, therefore, the reduced 4D flow MRI-derived WSS estimations may not be related only to low resolution but also to the accounted vessel motion [63].

1.7 Data assimilation

Data assimilation (DA) is a mathematical approach that aims at optimally combining results from numerical models with observations. Assimilation of measured data (generally sparse and noisy) and numerical models is well established in numerical weather predictions [24]. The merging improves the quality of the information in both directions: numerical simulations are improved by the including data-related effects and features otherwise difficult to model; while, measurements are denoised by assimilation of results based on physical and constitutive laws. Traditionally there are two strategies for performing DA:

1. Ensemble Data Assimilation

2. Variational Data Assimilation

Both srategies have been defined and applied in earth sciences. Ensemble DA is a sequential methods and belongs to the estimatory theory, while variational DA is a batch method [92]. Ensemble DA is based on the ensemble Kalman filter (EnKF), which is a statistical approach generally applied for prediction of linear systems affected by uncertainty, but in DA it is extended to nonlinear problems. Variational DA (Var, or in its specific 3D implementation 3DVar) implements an algorithm for the identifications of a set of control variables which minimizes (optimization problem) a functional dependent from the mismatch between the numerical model solutions and the observations. The control variables affect the mathematical model which is used as constraint for the optimization problem. Variatonal DA approach can be depicted as a classical feedback loop (Fig. 1.8).

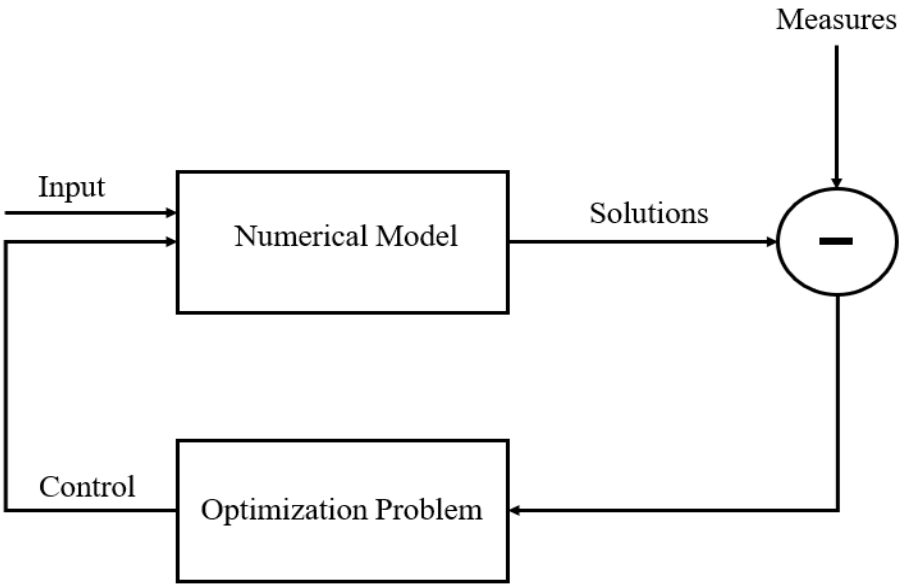

Figure 1.8: Schematic representation of Variational DA approach. Image adapted from [93].

1.7.1 Data Assimilation in computational hemodynamics

As mentioned in the previous section, numerical models (i.e. CFD and FSI) and 4D flow MRI are two valuable alternative for investigation of hemodynamics in cardiovascular districts, such as IAs. However, both techniques still have limitations: numerical models depend on the assumption needed for the model, which may hamper their clinical implementation; 4D flow MRI has a low resolution, long time-scan and postprocessing, and image quality is be affected by noise.

With DA, noisy and uncertain 4D flow data can be incorporated into numerical simulations

improving the accuracy and physical correctness (imposing incompressibility and conservation laws) of the measured velocity fields. Only a few studies have been devoted to DA applied to hemodynamics. This is probably due to the very recent advancements in medical imaging which provide tools to measure blood flow. Ensemble DA was applied to combine 3D PC-MRI data and CFD simulations in steady [94] and transient [95] conditions to reconstruct blood flow in an idealized IA using a Localization Ensemble Transform Kalman Filter (LETKF) approach. In both works, the DA procedure outputs were compared with high-resolution PIV to validate the procedure. Improvement in flow prediction with respect to the noisy PC-MRI data were obtained, confirming the DA procedure as a valuable approach to get high-resolution flow fields. Moreover, the computational cost was kept lower than Extended Kalman Filter, previously implemented for DA in pulsatile cardiac flow [96].

With respect to Ensemble Kalman Filters, Var is based on a more complex formulation due to the need for linear and adjoint models which increase the computational cost in comparison to one simple model simulation. For this reason, most of the numerical studies on Var addressed steady-state condition and 2D geometries. As Ensemble DA, Var can be applied in computational hemodynamics, merging the data provided by instruments or images about blood velocity with the Navier-Stokes model in order to improve the flow field reconstruction in the anatomical district of interest. Assuming as known the velocity measurements $\mathbf{u}_\mathrm{m}$ in a subregion of the domain of interest (Ω), the mathematical formulation for the incorporation of velocity data into the computation of the incompressible Navier-Stokes equations reads as follows:

$$\begin{aligned} \min_{\mathbf{c}} J(\mathbf{u},\mathbf{c}) = \mathit{dist}(f(\mathbf{u}),\mathbf{u}_\mathrm{m}) + \mathit{Regularisation}(\mathbf{c}) \\ \text{s.t.} \qquad F(\mathbf{u},\mathbf{c}) = 0 \end{aligned} \tag{1.8}$$

Eq. 1.8 is a PDE-constrained optimization problem for the identification of a control variable $\mathbf{c}$, which minimizes a functional J defined as a misfit between the computed velocity, from Navier-Stokes equations, and the velocity measures $\mathbf{u}_\mathrm{m}$. The computed velocity is mapped on the measurements sites by a function *f(·)*. A Regularization term is added for the well-posedness of the problem. The minimization problem is constraint by Eq. 1.4, F($\mathbf{u}$,$\mathbf{c}$), with proper initial and boundary conditions.

A problem in the form of Eq. 1.8 can be solved in two alternative ways. The first approach consists in defining the problem at the continuum level and perform the optimization. Successively, the resulting set of equations are discretized. This is the *Optimize then Discretize* (OD) approach. In the second approach, instead, the problem is discretized and then the

optimization of the discrete system is performed. This second approach is called the *Discretize then Optimize* (DO) approach.

Var procedures in hemodynamics have been investigated by Elia et al. in several works. In [25] they investigated two different formulations of Var DA, a splitting technique and a control based formulation, based on 2D stokes flow simulations. Synthetic data were generated by analytical solution on some planes along the domain. The splitting technique relies on solving the numerical model on subdomains and using the velocity data as inflow boundary conditions, while in the control based formulation, an optimization problem like Eq. 1.8 is solved to identify a control variable (in this case the inflow normal stress) which minimizes a specific functional depending on the misfit between the data and the recovered velocity field. Considering noisy velocity data, the first technique was found inconsistent because of a high sensitivity to noise. The control based formulation instead, was found robust and accurate but computationally expensive. Moreover, a DO approach and a OD approach were used to solve it, finding the first approach more efficient. In the following work [26] they proposed a Var DA implementation for including noisy measurements of the velocity field into the simulation of the Navier-Stokes equations. A DO procedure applied to Eq. 1.8 was used and the finite element method was selected as discretisation technique. The Var implemented was first tested for linear problem on the Oseen equations, and then extended to non-linear problem on the Navier-Stokes equations. A simplified 2D geometry of an aortic arch was used as illustrative application. The DA technique proved to be valuable in reconstructing the flow from synthetic noisy data even if computationally expensive. In particular, they assessed that both regularization and suitable measurements distribution might improve the efficiency of the procedure. In [27], the same Var formulation proposed in [26] was applied on a 2D idealized geometry of a carotid bifurcation and on a 3D axisymmetric geometry, using the inflow normal stress as control variable for the optimization problem. Assuming a generic domain Ω in R^d (d = 2, 3) with inflow boundary Γ_{in}, outflow boundary Γ_{out} and physical wall of the vessel Γ_{wall}, the mathematical formulation of the Var approach, derived from Eq.

1.8, reads as follows:

$$\min_{\mathbf{h}} J(\mathbf{u},\mathbf{h}) = dist(f(\mathbf{u}),\mathbf{u}_{\mathrm{m}}) + Regularization(\mathbf{h})$$
$$\text{s.t.} \begin{cases} -\nu\nabla\cdot(\nabla\mathbf{u}+\nabla\mathbf{u}^T)+(\mathbf{u}\cdot\nabla)\mathbf{u}+\nabla p = 0 \quad \text{in } \Omega, \\ \nabla\cdot\mathbf{u} = 0 \quad \text{in } \Omega, \\ \mathbf{u} = 0 \quad \text{on } \Gamma_{wall}, \\ -\nu\nabla\cdot(\nabla\mathbf{u}+\nabla\mathbf{u}^T)\mathbf{n}+p\mathbf{n} = \mathbf{h} \quad \text{on } \Gamma_{in}, \\ -\nu\nabla\cdot(\nabla\mathbf{u}+\nabla\mathbf{u}^T)\mathbf{n}+p\mathbf{n} = \mathbf{g} \quad \text{on } \Gamma_{out}. \end{cases} \tag{1.9}$$

With $\mathbf{u(x)} \in [H^1(\Omega)]^d$ velocity and $\mathrm{p}(\mathbf{x}) \in L_0^2(\Omega)$ pressure, variables of interest which are assumed to obey the Navier-Stokes equations and belong to Hilbert space (H^1) and space of square integrable functions (L_0^2), respectively. This formulation corresponds to an inverse problem where a DO approach was used to minimize the misfit between the computed velocity field and the data, subject to the incompressible, steady-state Navier-Stokes equations. The optimization problem was solved iteratively by means of a Reduced Hessian Method applied to a Lagrangian functional constructed by adding to the functional J the discrete Navier-Stokes equations, weighted by unknown multipliers, and then compute the derivative of the Lagrangian function with respect to the state variables, the multipliers and the control variables. The first two derivatives are the so called adjoint equations. With respect to [27], here Var was tested on the computation of WSS from synthetic noisy data on a 2D vessel bifurcation and in a 3D axysymmetric model. The accuracy of the assimilated solution was investigated, confirming the statements reported in [27]. In [97] the same problem was solved through a Bayesian method formulating a statistical inverse problem. The main difference relies on assuming the discrete variable as random. The inclusion of statistical information in the solution of the inverse problem results in a considerable gain in accuracy. These preliminary works highlighted the impact of DA on computational hemodynamic in clinical scenarios, particularly when patient specific measurements of velocity field are provided, for example by means of 4D flow MRI. In [28] a data assimilation approach was applied for the first time to a realistic 3D geometry of a saccular brain aneurysm. A comparison between Dirchlet and Neumann boundary control was carried applying a DO approach as solution strategy. However, the flow condition was stationary and the flow data were synthetic. 4D flow MRI measurements were applied for the first time in a Var

DA strategy in [29]. Here, Koltukluoğlu et al. proposed a DA method for 3D steady-state blood flow simulations following the OD approach. The novelty of this approach relies on an optimisation procedure based on a variational framework where the cost functional depends on flow-matching in the whole domain volume and not only on specific sites as in the previous work. The control variable used in this case was the Dirchlet boundary condition at the inlet. A sensitivity analysis with respect to changes in the optimisation parameters and with respect to changes in the flow-matching domain was carried out. The optimization problem consisted in solving a nonlinear system of coupled variational equations (obtained by computing the derivative of a Lagrangian functional as described above) by means of a gradient descent-like iterative method. The direct and the adjoint problems were approximated using the finite volume method. The 4D flow data were acquired from a glass replica of the aorta. Before using the experimental data in the DA approach, the measurements were opportunely denoised, mapped on the computational mesh where flow simulations were performed and finally a space projection was applied to recover back the divergence-free property of the flow data. The validation of the DA method was carried with synthetic high resolution CFD simulations performed in the same geometry and the 4D flow MRI measurements. The quantitative comparison showed that the optimized solution matched better the synthetic data with respect to a CFD solution obtained with noisy BCs. In particular, the data assimilation was most effective when applied close to the inlet (where the optimization was performed) and got worse decreasing the near-wall distance of the flow-matching domain. Similar findings were reported when assimilating 4D flow measurements. The optimized solutions were qualitatively and quantitatively closer to the observations, than the predictions from CFD, supporting that DA provides better solutions when compared with classical CFD as showed in Fig. 1.9. In [30], for the first time, Funke et al. derived and implemented 4DVar for transient blood flow. They investigated its feasibility and robustness in cerebral aneurysms with 4D data obtained from a PC-MRI scan. They formulated the Var DA as a mathematical optimimisation problem constrained by the Navier-Stokes equations where the unknown model parameters, to be identified by the DA, were the initial and boundary conditions of the model equations. A detailed description of the mathematical formulation of the problem and of the numerical assumptions was given. A DO approach and a finite element method were used to formulate the problem. Optimization was performed using a Reduced Hessian Method applied to the functional representing the misfit between the computed velocity and the data. A complete description of the adjoint approach used to solve the functional derivative was provided,

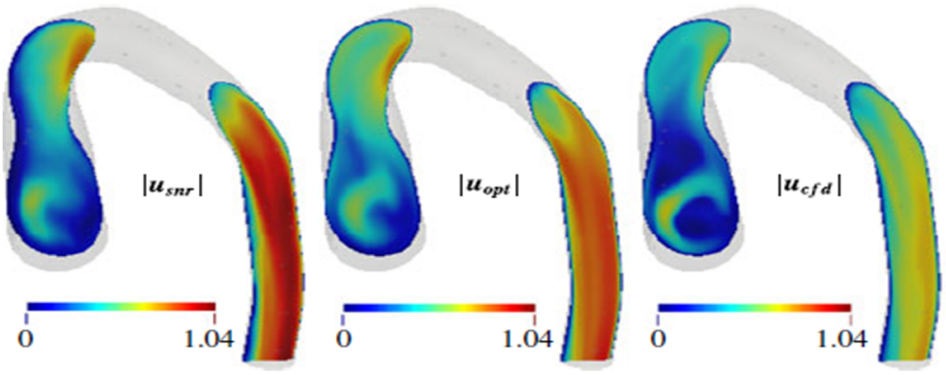

Figure 1.9: Velocity magnitude in a cross-sectional slice of the aorta replica. Comparison among the 4D flow data, the CFD solution and the optimized solution obtained in [28].

highlighting the advantages and disadvantages of this approach. The Navier-Stokes solver was implemented in the FEniCS finite element framework which has an adjoint solver derived via the algorithmic differentiation tool `dolfin-adjoint`. The authors verified the DA approach on a 2D test case using synthetic velocity data, investigating the role of the regularization term in the functional formulation, the impact of the sparsity in the physical observations and the choice of the controlled boundaries. The methodology proposed appeared to be robust in the sense of numerical stability for transient problem but the associated computational cost was much more higher than a single flow simulation (50-100 times). In the 3D test, performed on a canine cerebral aneurysm model, the evaluation of the method was carried only qualitatively comparing the flow magnitude within the aneurysm among the observations, the assimilation and the high-resolution CFD results at the peak flow instant. The difference between the DA solution and the observation were minimal and probably due to the noise in the observation. While the high-resolution CFD simulation provided a transient to turbulent behaviour which was not detected by the assimilated solution.

1.8 Conclusion

As discussed in the previous paragraphs, a clinical evaluation of IA risk of rupture is complex and difficult. It is predominantly based on morphological parameters, patient factors such as age and prior diseases and aneurysm evolution. These factors are highly dependent on the specialist experience and the accuracy of the imaging technique used for the evaluation. Hemodynamic parameters have been reported to be valuable predictor

for rupture. Nevertheless, the combination of hemodynamic features with the traditional aneurysm rupture risk stratification is difficult to apply to individual patients. Moreover, rupture risk evaluation influences the decision above the therapy treatment to adopt, whether it is conservative management, clipping or coiling, whose outcomes highly depend on the aneurysm status.

Numerical simulations of blood flow and 4D flow MRI have been proved valuable for evaluating flow in IAs enabling a high patient-specific evaluation of IA risk of rupture. Unfortunately, both techniques have limitations:

CFD depends on the assumptions needed for the model, such as geometry reconstruction from clinical images, boundary conditions, blood modelling and wall parameters (if FSI simulations is performed), which may hamper its clinical implementation.

4D flow MRI, on the other hand, has a low resolution, long time-scan and postprocessing, and image quality is affected by noise.

DA is a promising approach to combine numerical models with 4D flow MRI, enabling super-resolution and noise reduction in 4D flow measurements.

The main objectives of the present work are the implementation and evaluation of a data assimilation (3DVar) approach in reconstructing IA blood flow from 4D flow data. 3DVar in IA blood flow simulation would improve the hemodynamic assessment by fully exploiting 4D flow measurements. In this way, 3DVar aims to increase the accuracy of numerical models even when reliable model parameters, such as pressure estimations or vessel properties, are not available. This will ultimately lead to more accurate risk stratification for IAs.

Chapter 2

Materials and methods

In this chapter the workflow designed to perform the numerical analyses is described. In the first part, the patient-specific CFD and FSI simulations carried out in SimVascular are presented. In the second part of this chapter, the finite element framework for the solution of the Navier-Stokes equations and the 3DVar implemented in FEniCS is illustrated.

2.1 4D flow data and anatomical model

A 4D flow MRI dataset of a saccular IA located at the bifurcation of ICA and ACA-MCA junction was considered. The 4D flow MRI acquisition was provided in *.vtk* format by the Institute of Neuroradiology, University Hospital LMU, Munich, Germany. The measurements were performed with the use of Philips Ingenuity TF PET/MR with an Achieva 3.0T TX series MR system (Philips Healthcare, Cleveland, Ohio, USA)). Cerebral 3D blood flow was measured by using cardiac gated 4D phase-contrast (PC) MR imaging on the entire aneurysm volume and adjacent parent vessel. Data were acquired with the following pulse parameter: FOV 190×210 mm^2, acquisition voxel size $1 \times 1 \times 1$ mm^3, reconstructed with 0.82 mm^3, sense acceleration factor 2, TR/TE 4.6/2.9 ms, velocity sensitivity encoding parameter (VENC) was set to 80 cm/s in all directions. The number of cardiac phases was 16 for a heart rate of 65 bpm. Acquisition time was approximately 13 min. The data was then postproccesed by applying the correction strategies described in [37]. After correction and denoising the 3D-PCMRI was registered on a 3D Rotational Angiography (3DRA) interpolating the velocity at the 3DRA surface to zero. The final result is shown in Fig. 2.1.

The geometric vascular model was extracted from 4D MRI data in *.stl* format through an ad-hoc python script. Subsequently, the model was imported in Meshmixer 3.5 (Autodesk,

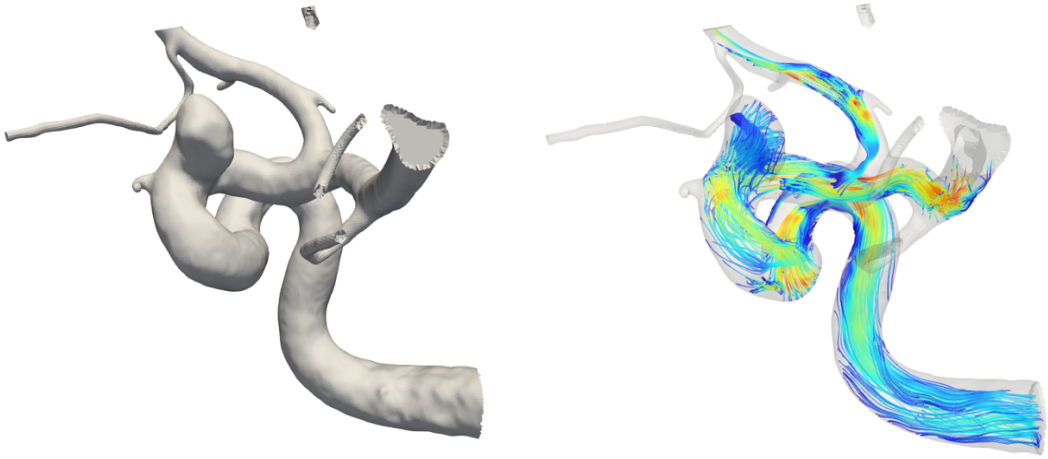

Figure 2.1: 4D flow data after registration on 3DRA. Geometric vascular model (right) and velocity field (left) represented by streamlines in Paraview 5.7.0 (Kitware, Santa Fe, New Mexico, USA).

Mill Valley, California, USA) in order to cut the small vessels were velocity data was not detected because of the low resolution of 4D flow. The STL was then smoothed (via shape-preserving interpolation) and remeshed. The final 3D model used for the numerical simulations is shown in Fig. 2.2. The model comprised the side-wall saccular aneurysm located at the bifurcation of ICA, MCA and ACA. Inlet (ICA) and Outlets (MCA and ACA) diameters are reported in Table 2.1. Table 2.2 shows the morphological parameters of the saccular aneurysm following the definition reported in Fig. 1.3 .

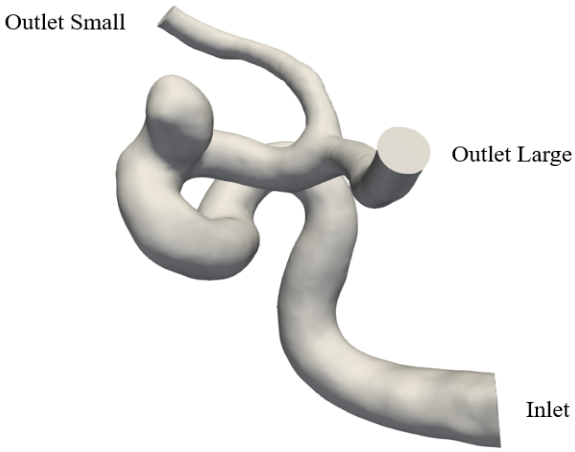

Figure 2.2: 3D model of the side-wall saccular aneurysm at the bifurcation of ICA (inlet), MCA (outlet large), and ACA (outlet small) used for the numerical simulations.

	Diameter [mm]
Inlet	5.07
Outlet Large	2.48
Outlet Small	1.95

Table 2.1: Inlet and outlets diameters of the 3D model.

Morphological Parameters	
N	3.52 [mm]
H1	4.92 [mm]
H2	4.88 [mm]
D1	4.17 [mm]
D2	3.75 [mm]
W	4.64 [mm]
AR	1.40
SR	1.23
H/W	1.05

Table 2.2: Morphological parameters of the saccular aneurysm. Aspect Ratio (AR), Size Ratio (SR) and Height to Width Ratio (H/W) are reported.

2.2 Numerical simulations

The numerical simulations described in this chapter were carried out using the open-source software SimVascular. The SimVascular enviorment provides a complete pipeline from medical image data segmentation to patient specific blood flow simulation and analysis [98]. SimVascular enables to set BCs that achieve physiological levels of pressures, and is endowed with a robust finite element solver for FSI.

2.2.1 Mesh Generation

The 3D model was meshed using the SimVascular embedded meshing tool TetGen. The mesh was generated estimating a proper *Global Max Edge Size* and using the default software's parameters. No boundary layers were generated. A sensitivity analysis was performed by running steady flow simulations on three meshes consisting of ∼2 (coarse), ∼4 (medium) and ∼8 (fine) million elements. A plug velocity profile, given the peak flow rate, was applied at the inlet, while zero pressure was set at both outlets. Velocity magnitude contours were evaluated on a cross section within the aneurysm neck, as it is reported in [99]. The 90^{th} percentile of velocity was extracted from the section and used as parameter of grid convergence to evaluate the best suited mesh. Then the Grid Convergence Index (GCI) [31] was estimated for the fine-to-medium and for the medium-to-coarse mesh according to [100]. The GCI is based

	Coarse	Mid	Fine
N	2083718	4043601	8041791
f [cm/s]	72.69	72.34	72.31
$GCI_{2,3}$		0.004%	
$GCI_{1,2}$		0.56%	
k		0.99	

Table 2.3: Mesh sensitivity analysis.

upon a grid refinement error estimator extracted from the theory of generalized Richardson extrapolation. It provides a percentage measure of how much the computed value (velocity magnitude in this case) is far from the asymptotic solution (i.e. when the grid spacing tends to zero). The objective is to quantify the error that would generate from each level of grid refinement. Let the subscripts 1,2,3 indicate the fine, medium and coarse mesh respectively:

$$r \approx \left(\frac{N_1}{N_2}\right)^{1/3} \approx \left(\frac{N_2}{N_3}\right)^{1/3}, \tag{2.1}$$

$$p = \frac{log\left(\frac{f_3 - f_2}{f_2 - f_1}\right)}{log(r)}, \tag{2.2}$$

$$E_1 = \frac{\frac{f_2 - f_1}{f_1}}{r^p - 1}, \quad E_2 = \frac{\frac{f_3 - f_2}{f_2}}{r^p - 1} \tag{2.3}$$

$$GCI_{1,2} = F_s \mid E_1 \mid, \quad GCI_{2,3} = F_s \mid E_2 \mid \tag{2.4}$$

where N is the number of elements, p is the order of convergence, f is the parameter of interest, E is the estimated fractional error and F_s is the factor of safety that for comparison of three or more grids should be set to 1.25 [31]. In this case, f_1 = 72.31 cm/s, f_2 = 72.34 cm/s and f_3 = 72.69 cm/s were found. $GCI_{1,2}$ was approximately 0.56%, therefore less than 1% which is the target value to asses the independence of the results from the grid refinement. For this reason the medium mesh was chosen for the following simulations. Additionally, the solutions were in in the asymptotic range of convergence since $k = \frac{GCI_{2,3}}{r^p GCI_{1,2}}$ was found close to 1 (Table 2.3). The selected mesh consisted of tetrahedra (Fig. 2.3) and it was generated by using a *Global Max Edge Size* of 0.152 mm.

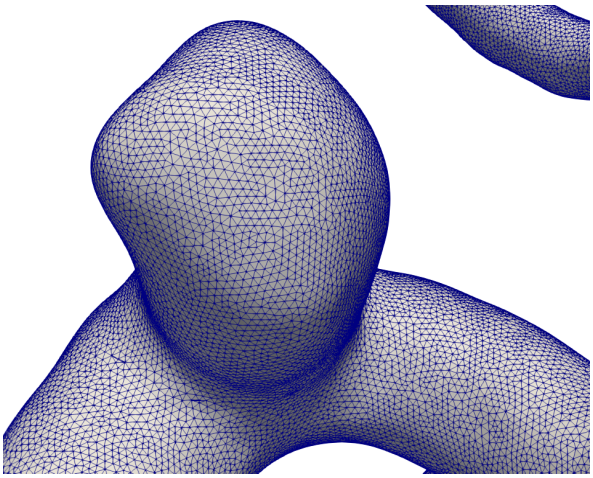

Figure 2.3: Visualization of mesh details in a zoom on the aneurysm region.

2.2.2 Fluid materials properties and initial condition

The Newtonian blood rheology is one of the most popular assumption in CFD models of blood flow. Non-Newtonian behaviour modeling is plausible in low shear rate region where recirculating flow, vortex structures, flow separation and flow stagnation are common features. In aneurysmal flow these characteristics are usually found, therefore a non-Newtonian modelling would be motivated. However, according to [32], a non-Newtonian blood rheology assumption would overestimate shear dependent behaviour, leading to an incorrect estimation of hemodynamics. Therefore blood was modelled as Newtonian fluid with a density of $\rho = 1.06$ g/cm^3 and a viscosity of $\mu = 0.04$ poise.

Initial conditions are needed to simulate unsteady blood flow. In SimVascular, they are required in the basic parameters section. For the rigid wall (CFD) simulation, default initial conditions were used. Both initial velocity components and initial pressure were set to zero ($\mathbf{u}$ = (0,0,0), p = 0). For the FSI simulations, instead, a Initial Condition (IC) file is provided. As it will explain in the governing equations subsection the FSI implemented in SimVascular relies on the Coupled Momentum Method (CMM-FSI). The CMM algorithm requests to initialize the problem with a previous rigid wall simulations, with the same initial and boundary conditions, to provide a pressure distribution in order to compute the initial values for the wall stress/displacements fields. For this reason, a IC file with the last restart file of the CFD simulation was loaded in the simulation pipeline.

The blood flow regime was assumed laminar, since the Reynolds number $Re = \frac{\rho \overline{U} D}{\mu}$, evaluated along a plane cross the aneurysm neck, was equal to 202 ($\ll$ 2000).

2.2.3 Boundary conditions

As inlet boundary condition for the model, a time-varying flow rate curve extracted from 4D flow data was prescribed. An ad-hoc python script was used to extract the velocity data from the 4D flow in *.csv* format. Then, the data were used to write a custom Boundary Condition Text (BCT) file as requested by SimVascular. A BCT file consists of a text file where for each time instant of the flow curve velocity has to be prescribed point-wise over the inlet mesh. To account for the effect of distal vasculature and obtain physiological flow rate and pressure curves, at each outlet, 3-EWK models were set as boundary conditions (Fig. 2.4). In 3-EWK model downstream vasculature is represented by means of a proximal resistance R_p, a distal resistance R_d and and a compliance C. The values reported in Table 2.4, were calculated following the approach described in [34]. Briefly, an average pressure over the cardiac cycle for each outlet $\overline{P}$= 80 mmHg was assumed; the total resistance R_t was calculated as $R_t = \frac{\overline{P}}{\overline{Q}}$, with $\overline{Q}$ being the average flow rate at each outlet obtained from 4D flow. In order to account for conservation of mass, which in 4D flow measurements may not be satisfied due to noise, the average flow rate from the smaller outlet was calculated as the difference between the inlet and the larger outlet flow rates. Hence, the proximal resistance R_p was calculated as $R_t = \frac{\rho c}{A}$, where ρ is the blood density, c is the pulse wave velocity and A is the outlet cross-sectional area. The value c was calculated using the relation $c = \frac{a_2}{(2r)^{b_2}}$, with $a_2 = 13.3$, $b_2 = 0.3$ and r being the vessel radius in mm [101]. Next,the distal resistance R_d was calculated from $R_t = R_p + R_d$. For each outlet, the total compliance C was calculated as $C = \frac{\tau}{R_t}$ as described in [102], with $\tau = 1.79$, which corresponds to the exponential decay of diastolic pressure in normotensive patients [103].

Outlet	R_p	C	R_d
Small	3.880	0.271	2.725
Large	2.217	0.313	3.506

Table 2.4: 3-EWK model parameters: proximal resistance, compliance and distal resistance for small and large outlets. Resistances are expressed in $\frac{g}{(mm^4 \cdot s)}$, while compliances are expressed in $\frac{mm^4 \cdot s}{g}$

2.2.4 Vessel wall properties

One rigid-wall simulation (CFD) and two deformable-wall simulations (Uniform-FSI, NonUniform-FSI) were carried out in SimVascular. In the Uniform-FSI, a uniform wall thickness was assumed, while in the NonUniform-FSI a decreasing in vessel wall thickness around the aneurysm was considered. In order to accounting for the pathological thinning of

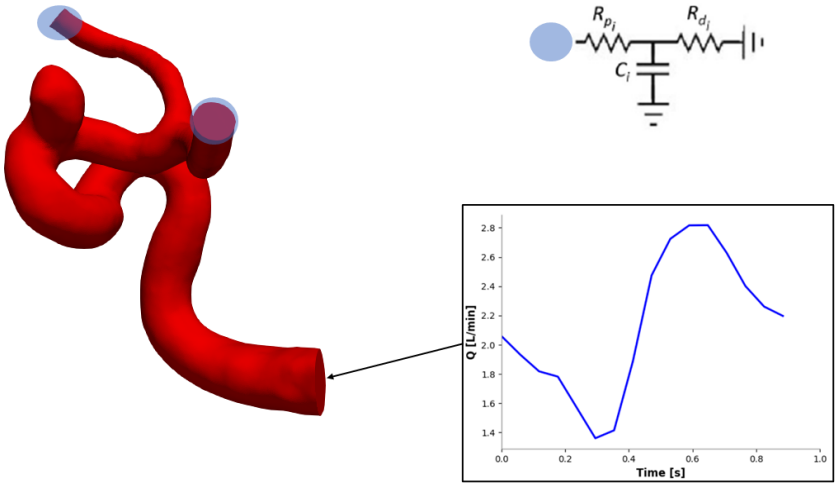

Figure 2.4: Description of the model boundary conditions used in the numerical simulations; patient-specific transient flow rate was imposed at the inlet, while 3-EWK were set as outlet boundary conditions.

the wall around the aneurysm region, the model face IDs generated by SimVascular were modified adding a new ID for the aneurysm, by means of an ad-hoc python script. In SimVascular's model section, the software requires to define the face IDs for the model surfaces in order to assign the proper BCs and wall parameters for the FSI simulations. The implemented script enables to define a new region around the aneurysm applying a Paraview clip filter in a very handy way. In this fashion, in Uniform-FSI a Young's modulus $E = 1$ MPa and a wall thickness $\zeta = 300\mu$m were assigned. In NonUniform-FSI, according to [17], a wall thickness $\zeta = 100\mu$m around the aneurysm was assigned.

2.2.5 Governing equations

In this subsection the main equations involved in the mathematical formulation of the solution method for the CFD and FSI are described. Particular attention will be given to the CMM-FSI formulation implemented in SimVascular. This formulation modifies a convectional finite element solution for the Navier-Stokes equations in a rigid domain, so that wall elasticity is taken into account [33].

As it is mentioned in Chapter 1, in the fluid domain the governing equations are represented by the incompressible Navier-Stokes equations. Following the notation used in [33] and referring to the schematic representation in Fig. 2.5, the strong form of the continuity and momentum balance equations for blood, assuming rigid walls, reads as follows:

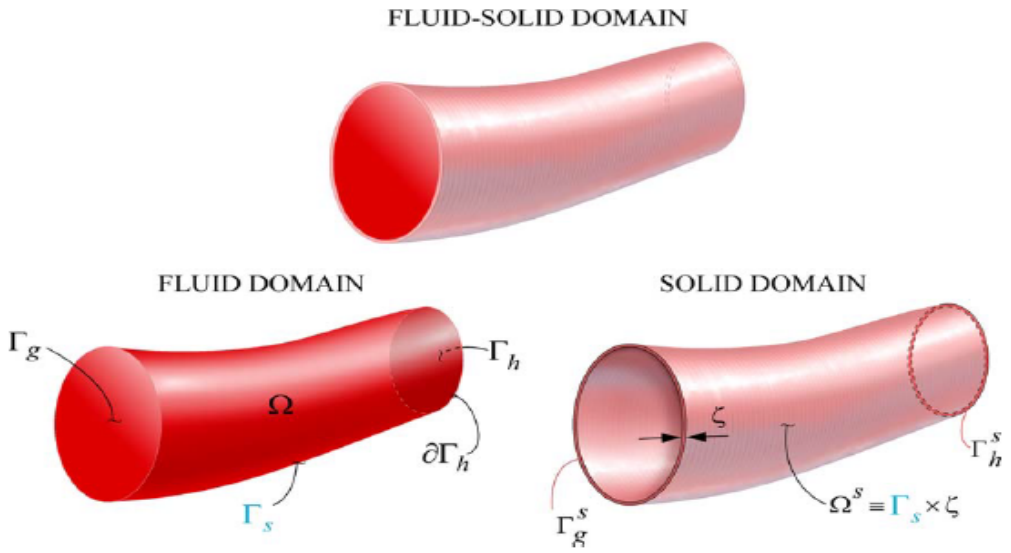

Figure 2.5: Schematic representation of the fluid and solid domains and their boundaries [33].

Given $\mathbf{f} : \Omega \times (0,T) \longrightarrow \mathbb{R}^3$, $\mathbf{g} : \Gamma_g \times (0,T) \longrightarrow \mathbb{R}^3$, $\mathbf{h} : \Gamma_h \times (0,T) \longrightarrow \mathbb{R}^3$, $\mathbf{u}^0 : \Omega \longrightarrow \mathbb{R}^3$; find $\mathbf{u}(\mathbf{x},t)$ and $p(\mathbf{x},t)$ $\forall \mathbf{x} \in \Omega, \forall t \in [0,T]$ such that:

$$\rho \mathbf{u}_t + \rho \mathbf{u} \cdot \nabla \mathbf{u} = -\nabla p + \nabla \tau + \mathbf{f} \quad \text{for } (\mathbf{x},t) \in \Omega \times (0,T), \tag{2.5}$$

$$\nabla \cdot \mathbf{u} = 0 \quad \text{for } (\mathbf{x},t) \in \Omega \times (0,T), \tag{2.6}$$

with a Dirichlet boundary condition:

$$\mathbf{u} = \mathbf{g} \quad \text{for } (\mathbf{x},t) \in \Gamma_g \times (0,T), \tag{2.7}$$

$$\mathbf{u} = 0 \quad \text{for } (\mathbf{x},t) \in \Gamma_s \times (0,T), \tag{2.8}$$

and Neumann boundary conditions:

$$\mathbf{t}_n = \sigma \mathbf{n} = [-p\mathbf{I} + \tau]\mathbf{n} = \mathbf{h} \quad \text{for } (\mathbf{x},t) \in \Gamma_g \times (0,T). \tag{2.9}$$

plus the initial condition:

$$\mathbf{u}(\mathbf{x},0) = \mathbf{u}^0(\mathbf{x}) \quad \text{for } \mathbf{x} \in \Omega. \tag{2.10}$$

In these equations, apart from the notation already defined in chapter1, $\mathbf{u}_t$ is a contraction for the velocity time derivative, τ represents the viscous stress tensor, $\mathbf{f}$ is the prescribed volume force and σ is the cauchy stress tensor for fluid, which multiplied for the surface normal vector $\mathbf{n}$, returns the normal stress vector $\mathbf{t}_n$.
Assuming deformable walls, the governing equations for the fluid domain change. Eq. 2.9 is replaced by the following Neumann boundary conditions,

$$\mathbf{t}_n = \mathbf{t}^f \quad \text{for } (\mathbf{x}, t) \in \Gamma_s \times (0, T). \tag{2.11}$$

where $\mathbf{t}^f$ is an unknown and it will be obtained solving the vessel wall equations for the solid domain. Therefore, $\mathbf{t}^f$ represents in fact the coupling parameter between the fluid and the solid domain.
In the CMM-FSI formulation implemented in SimVascular, the classic elastodynamics equations are used to describe the motion of the vessel in a domain $\Omega^s \in \mathbb{R}^3$ (see Fig. 2.5). In particular, the vessel wall mechanics is approximated using a thin-walled structure assumption. Therefore, the solid domain Ω^s can be topologically related to the surface defining the lateral boundary of the fluid domain Γ_s [33]. The strong form of the vessel wall problem can be described as follows:
Given $\mathbf{b}^s : \Omega^s \times (0, T) \longrightarrow \mathbb{R}^3$, $\mathbf{g}^s : \Gamma_g s \times (0, T) \longrightarrow \mathbb{R}^3$, $\mathbf{h}^s : \Gamma_h^s \times (0, T) \longrightarrow \mathbb{R}^3$, $\mathbf{d}^0 : \Omega \longrightarrow \mathbb{R}^3$, $\mathbf{d}_t^0 : \Omega \longrightarrow \mathbb{R}^3$; find $\mathbf{d}(\mathbf{x}, t)\ \forall \mathbf{x} \in \Omega, \forall t \in [0, T]$ such that:

$$\rho^s \mathbf{d}_{tt} = \nabla \cdot \sigma^s + \mathbf{b}^s \quad \text{for } (\mathbf{x}, t) \in \Omega_s \times (0, T). \tag{2.12}$$

with boundary conditions:

$$\mathbf{d} = \mathbf{g} \quad \text{for } (\mathbf{x}, t) \in \Gamma_g^s \times (0, T), \tag{2.13}$$

$$\mathbf{t}_n = \sigma^s \mathbf{n} = \mathbf{h}^s \quad \text{for } (\mathbf{x}, t) \in \Gamma_h^s \times (0, T), \tag{2.14}$$

and initial conditions:

$$\mathbf{d}(\mathbf{x}, 0) = \mathbf{d}^0(\mathbf{x}) \quad \text{for } \mathbf{x} \in \Omega^s, \tag{2.15}$$

$$\mathbf{d}_t(\mathbf{x}, 0) = \mathbf{d}_t^0(\mathbf{x}) \quad \text{for } \mathbf{x} \in \Omega^s, \tag{2.16}$$

where $\mathbf{d}$ is the displacement field, $\mathbf{d}_{tt}$ is a contraction for the displacement second time derivative, σ^s is the cauchy stress tensor for solid and $\mathbf{b}^s$ is the body force. In this case, the assumption of thin-walled structure allows to relate the surface traction $\mathbf{t}^f$, acting on the fluid lateral boundary due to the interaction with the solid, to the body force $\mathbf{b}^s$, acting on the solid domain, through the wall thickness ζ:

$$\mathbf{b}^s = -\frac{\mathbf{t}^f}{\zeta} \tag{2.17}$$

This is the dynamic condition which is used in the weak form of the CMM-FSI method to couple the fluid and the solid domains. For the sake of simplicity, here only the CMM-FSI weak form is derived. Referring to Fig. 2.5, for the fluid domain Ω with boundary $\Gamma = \Gamma_g \cup \Gamma_h \cup \Gamma_s; \Gamma_g \cap \Gamma_h \cap \Gamma_s$, the following function space are defined:

$$S_h^k = \big\{\mathbf{u} \mid \mathbf{u}(\cdot,t) \in H^1(\Omega), t \in [0,T], \mathbf{u} \mid_{x\in\overline{\Omega}_e} \in P_k(\overline{\Omega}_e), \mathbf{v} = \hat{\mathbf{g}} \quad \text{on} \quad \Gamma_g\big\}, \tag{2.18}$$

$$W_h^k = \big\{\mathbf{w} \mid \mathbf{w}(\cdot,t) \in H^1(\Omega), t \in [0,T], \mathbf{w} \mid_{x\in\overline{\Omega}_e} \in P_k(\overline{\Omega}_e), \mathbf{v} = 0 \quad \text{on} \quad \Gamma_g\big\}, \tag{2.19}$$

$$P_h^k = \big\{p \mid p(\cdot,t) \in H^1(\Omega), t \in [0,T], p \mid_{x\in\overline{\Omega}_e} \in P_k(\overline{\Omega}_e)\big\}, \tag{2.20}$$

where $\overline{\Omega}_e$ represents the closure of the finite element domain, $\hat{\mathbf{g}}$ the finite element approximation of the prescribed velocity field, $P_k(\overline{\Omega}_e)$ the space of continous polynomials within each element and the subscripts h and k represent the discrete approximation indexes. Then, the Galerkin finite element approximation for the fluid domain yields to the following weak form: find $\mathbf{u} \in S_h^k$ and $p \in P_h^k$ such that:

$$\begin{aligned} B_G(\mathbf{w},q;\mathbf{u},p) = &\int_\Omega \{\mathbf{w}\cdot(\rho\mathbf{u}_t + \rho\mathbf{u}\cdot\nabla\mathbf{u} - \mathbf{f}) + \nabla\mathbf{w} : (-pI+\tau) - \nabla q\cdot\mathbf{u}\}d\mathbf{x} + \\ &+ \int_{\Gamma_h}\{-\mathbf{w}\cdot\mathbf{h} + qu_n\}ds + \int_{\Gamma_s}\{-w\cdot\mathbf{t}^f + qu_n\}ds + \\ &+ \int_{\Gamma_g} qu_n ds = 0, \quad \forall\mathbf{w} \in W_h^k \quad and \quad \forall q \in P_h^k \end{aligned} \tag{2.21}$$

In the CMM-FSI, the weak form (Eq. 2.21) for the fluid domain is modified by expressing the unknown integral on Γ_s using the weak form for the solid governing equations, which is not herein explicitly reported for conciseness, and exploiting the coupled condition Eq. 2.17. Therefore, the combined formulation leads to the CMM-FSI weak form:

$$\begin{aligned} B_G(\mathbf{w},q;\mathbf{u},p) = \int_\Omega \{\mathbf{w}\cdot(\rho\mathbf{u}_t+\rho\mathbf{u}\cdot\nabla\mathbf{u}-\mathbf{f})+\nabla\mathbf{w}:(-pI+\tau)-\nabla q\cdot\mathbf{u}\}d\mathbf{x}+ \\ +\int_{\Gamma_h}\{-\mathbf{w}\cdot\mathbf{h}+qu_n\}ds+\int_{\Gamma_g}qu_nds+\zeta\int_{\Gamma_s}\{w\cdot\rho^s u_t+\nabla w:\sigma^s(d)\}ds- \\ -\zeta\int_{\delta\Gamma_h}w^s dl+\int_{\Gamma_s}qv_nds=0, \quad \forall\mathbf{w}\in W_h^k \quad and \quad \forall q\in P_h^k \end{aligned} \tag{2.22}$$

Actually, the weak formulation reported in [33] is a stabilized version of Eq.2.22, which is not herein reported for sake of simplicity.

As it is showed above, through the hypothesis of thin-walled structure for the vessel mechanics, a unique weak form accounting for both fluid and solid problem was obtained. To sum up, the CMM-FSI formulation starts from the conventional Navier-Stokes equations in a rigid domain, removes the no-slip condition along the wall boundary and replaces it with a traction condition. Through the thin wall approximation this unknown traction is related to a body force for the vessel wall, defined by the elastodynamics equations. Furthermore, the degrees-of-freedom of the vessel wall and the fluid boundary are strongly coupled, namely they coincide. This feature, together with a linearized approach,results in a fixed mesh at the fluid-solid interface, whose nodes can have nonzero velocities. All these features make the CMM-FSI computationally comparable to a rigid wall formulation, producing equivalent results, but with a lower computational effort, to those given by FSI formulations such as Arbitrary Lagrangian Eulerian (ALE) formulation, in problem where the deformations are small (<10%).

2.2.6 Solver parameters

The system of nonlinear first-order ordinary differential equations in time, resulting from the weak form given by Eq. 2.22, is integrated in time and linearized through the finite element code PHASTA [104]. In this way, within each time step a nonlinear system of equation is linearized and solved using a Newton-Raphson iterative method. For the time discretization, a time step size $\Delta t = 0.5$ ms was set. The time step size was estimated in order to satisfy the CFL condition, $CFL = \frac{u\Delta t}{h} \approx 1$, with u the averaged expected velocity and h the finite

element size. For the nonlinear iteration loop, the minimum and maximum iterations required for step construction were set respectively to 4 and 5. The latter parameter was increased to 10 in the deformable wall simulations. While the non linear residual was set to 0.001. To solve the linearized system GMRES was selected as linear solver and both continuity and momentum tolerance values were set to 1e−4. Solutions were saved each 20 time steps. Simulations were run for 3 cardiac cycles in order to reach the desired convergence residual and obtain periodicity, and only the last cycle was used for further analysis. Each cardiac cycle had a period of 0.9 s.

2.3 DA framework

For the DA assimilation approach, a Navier-Stokes solver was implemented in the FEniCS finite element framework [35]. Following the approach reported in [30], a Var DA formulation was defined as an optimisation problem constrained by the Navier-Stokes equations. The adjoint problem, derived from the optimisation algorithm, was solved via the algorithmic differentiation tool `dolfin-adjoint` [36]. The overall implemented framework can be synthesized in three steps:

1. Solution of a steady-state, rigid-wall simulation (The Tape)

2. Optimization problem

3. Solution of a steady-state rigid-wall simulation with optimized parameters.

Following [30], a *Discretize then optimize* (DO) approach was adopted to solve the Var DA formulation. In the following subsections, the mathematical assumptions behind the formulation and a brief description of the implementation will be given for each step.
The Var DA approach here implemented was tested on two 2D models (referred to as Hole and 2D-Ane, Fig.2.6a and Fig.2.6b). In these two test geometries, the effect of the regularisation parameters on the assimilated solution was investigated. A 3DVar was then implemented to assimilate flow data from 4D flow MRI into a 3D cerebral aneurysm CFD model (Fig. 2.7). In this case, the geometry was obtained by clipping the previously considered vascular district (Fig. 2.2) used to carry out the numerical simulations in SimVascular in order to reduce the computational cost. Influence of flow data was restricted only to the time instant of maximum flow rate corresponding to the 10^{th} time frame of the 4D flow acquisition.

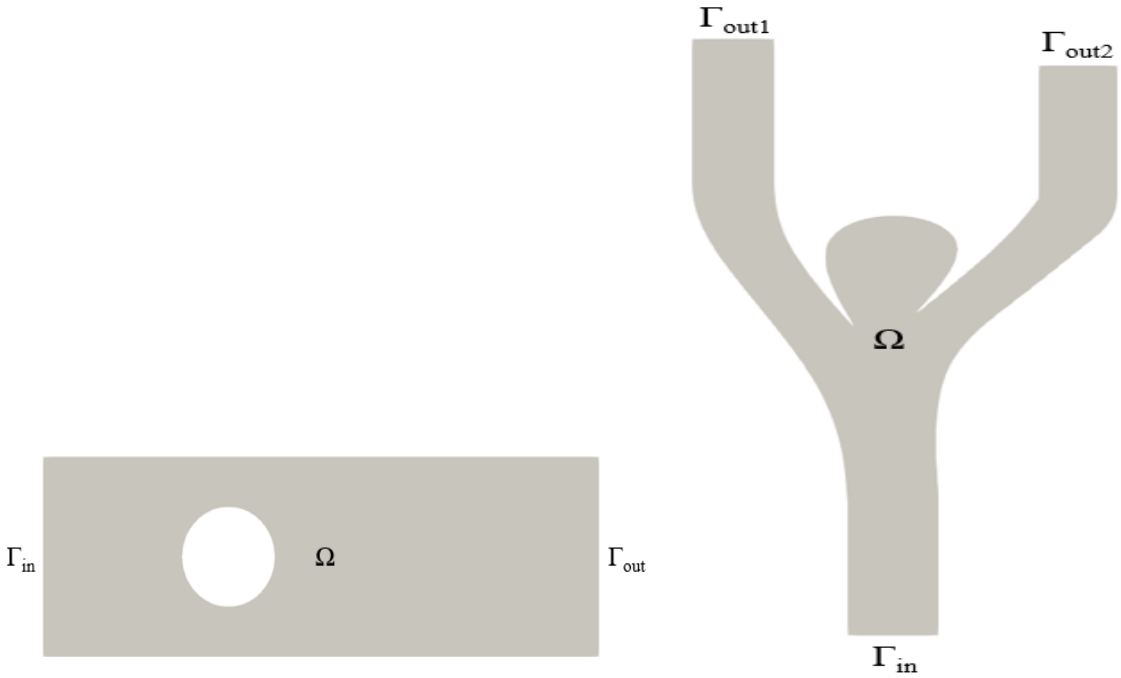

(a) (b)

Figure 2.6: 2D rigid models used to test the Var DA approach. (a) Hole, a 2D rectangular model with a circle hole within the domain Ω. (b) 2D-Ane, a 2D model resembling a blood vessel bifurcation with an aneurysm. The latter model is the same adopted in [30].

2.3.1 Discretization of Navier-Stokes equations: The Tape

FEniCS is an open-source computing platform for solving partial differential equations (PDEs) using finite element methods. The FEniCS problem-solving environment is implemented into both C++ and Python. FEniCS enables users to quickly translate scientific models into efficient finite element code through the domain-specific language UFL [105]. UFL is a high level interface to write variational forms of the model with a mathematical notation. Then, the model is assembled by DOLFIN, the programming interface of FEniCS.

Assuming a generic fixed spatial domain $\Omega \in \mathbb{R}^d$ (d=2 or 3), representing the fluid flow region, the Navier-Stokes equations reads as Eq.1.4. Referring to Fig. 2.6a and Fig. 2.7, a velocity field $\mathbf{g}$ was prescribed at the inlet Γ_{in} (Dirichlet BC), while at the outlet Γ_{out} zero pressure was assumed. For time discretisation a $\theta - method$ scheme was adopted, with a $\theta = 0.5$ and a time step $\Delta t = 1\text{e}{-3}$. The scheme was initialized with a prescribed velocity $\mathbf{u}_0$. The weak formulation for the Navier-Stokes model can be then written as follows:

Being $V_g = \{\mathbf{u} \in H^1(\Omega) : \mathbf{u} = \mathbf{g} \quad on \quad \Gamma_{in}\}$, $V = \{\mathbf{v} \in H^1(\Omega) : \mathbf{v} = 0 \quad on \quad \Gamma_{in}\}$ and $Q = \{q \in L^2(\Omega)\}$ function spaces for velocity and pressure fields respectively, find $\mathbf{u} \in V_g$ and

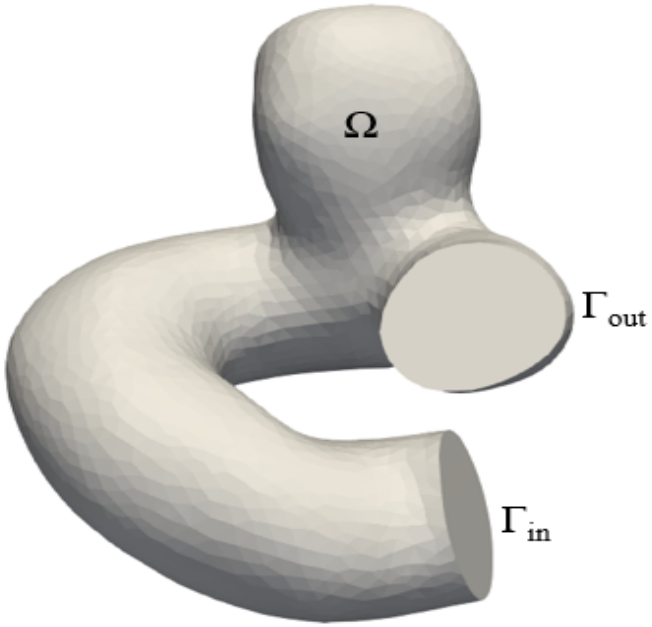

Figure 2.7: 3D cerebral aneurysm model obtained by clipping 2.2 upstream and downstream the aneurysm. A 3D model with one inlet Γ_{in} and one outlet Γ_{out} was obtained.

$p \in Q$ such that:

$$F(\mathbf{u}^{k+1}, \mathbf{v}, p^{k+1}, q) = (\frac{\mathbf{u}^{k+1} - \mathbf{u}^k}{\delta t}, \mathbf{v})_\Omega + ((\mathbf{u}^{k+\theta}\cdot)\nabla\mathbf{u}^{k+\theta}, \mathbf{v})_\Omega + (p^{k+1}, \nabla\mathbf{v})_\Omega$$
$$-(\nu\nabla\mathbf{u}^{k+\theta}, \nabla\mathbf{v})_\Omega - (q, \nabla\mathbf{u}^{k+1})_\Omega \quad \forall\mathbf{v} \in V, \forall q \in Q \tag{2.23}$$

with $\mathbf{v}$ and q suitable test functions for velocity and pressure respectively, and $\mathbf{u}^{k+\theta} = \theta\mathbf{u}^{k+1} + (1-\theta)\mathbf{u}^k$ for k=0,1,..., N-1 (N number of time instant). The variational form in Eq. 2.23 was obtained by multiplying Eq. 1.4 by $\mathbf{v}$ and q, taking the volume integral over the domain Ω, ruling out the second derivatives by using integration by parts and Green's identity, and applying the boundary conditions. The only external force is the body force which is usually neglected in cardiovascular applications.

The equation was then discretised in space by first order finite elements for both velocity and pressure spaces (P1-P1 discretisation). With a P1-P1 space discretisation the Ladyzhenskaya–Babuška–Brezzi (LBB) conditions are not satisfied. Therefore, the stabilisation term $-\beta h^2(\nabla p, \nabla q)_\Omega$ where h is the local mesh element size and $\beta = 1\text{e}{-3}$ is the stabilization coefficient, was added to Eq. 2.23. The problem was treated as transient even if it was actually a steady problem, since steady boundary conditions were assumed for each

time step. This numerical technique was adopted in order to stabilize the convective term, which can lead to instabilities in some flow conditions. Blood was modelled as Newtonian fluid with a density $\rho = 1.06$ g/cm^3 and a viscosity $\mu = 0.04$ poise. Notice that, since blood is an incompressible fluid, Eq.2.23 was divided by ρ, with $\nu = \mu/\rho$ kinematic viscosity. As mentioned above, in both 2D and 3D case a velocity field was prescribed as inlet and pressure zero was assumed in outlet. In particular for 3DVar, referring to Fig. 2.7, a velocity field, extracted from the highest flow time instant (10^{th} time frame) of the 4D flow acquisition, was prescribed point-wisely at the inlet Γ_{in} by interpolating the measurements over the inlet mesh. Finally, the velocity $\mathbf{u}_0$ was initialized with a velocity field extracted from the 9^{th} time frame of the 4D flow acquisition.

As it will be elucidated in the following subsections, the library for algorithmic differentiation allows to automatically derive the discrete adjoint equations of the assemble model in Eq. 2.23, which is called *forward model* or *Tape*.

Source term

The Var DA formulation implemented here relies on a fictitious source term $\mathbf{c} \in \mathbb{R}^d$ (d=2,3) added to the weak form of Navier-Stokes model in Eq. 2.23. This term acts as control parameter for the DA approach. The source term $\mathbf{c}$ was defined on the same finite element space of velocity and its role was to force the velocity field to resemble a target solution. A similar approach was used in optimal control of the Poisson equation in [106, 107], where the objective was to find the best heating/cooling term to achieve a desired temperature profile. A function χ was defined in order to map the target solution on the computational mesh of the model. χ was defined over the mesh cells and it assumed only two values, 0 and 1. In this way, assuming that the solution target is available only in a subdomain of Ω, the effect of the source term $\mathbf{c}$ can be activated only in that region by defining a suitable χ. The final weak form of Navier-Stokes model implemented for the Var DA is then:

$$\begin{aligned} F(\mathbf{u}^{k+1}, \mathbf{v}, p^{k+1}, q, \mathbf{c}) = (\frac{\mathbf{u}^{k+1} - \mathbf{u}^k}{\delta t}, \mathbf{v})_\Omega + ((\mathbf{u}^{k+\theta}.)\nabla \mathbf{u}^{k+\theta}, \mathbf{v})_\Omega + \\ (p^{k+1}, \nabla \mathbf{v})_\Omega - (\nu \nabla \mathbf{u}^{k+\theta}, \nabla \mathbf{v})_\Omega - (q, \nabla \mathbf{u}^{k+1})_\Omega + \\ (\chi \mathbf{c}, \mathbf{v})_\Omega \quad \forall \mathbf{v} \in V, \forall q \in Q \end{aligned} \tag{2.24}$$

with $\mathbf{c} \in V_g$.

2.3.2 Adjoint equations

As discussed in the introduction, Var DA in hemodynamics can be stated as a minimisation problem constrained by the Navier-Stokes equations (Eq. 2.24):

$$\begin{aligned} &\min_{\mathbf{c}} J(\mathbf{u}) + R(\mathbf{c}) \\ &\text{s.t.} \qquad F(\mathbf{u}, \mathbf{c}) = 0. \end{aligned} \tag{2.25}$$

Defining $\mathbf{u_{obs}}$ as the target solution, the functional J is defined as:

$$J(\mathbf{u}) = || \mathbf{u} - \mathbf{u}_{obs} ||_{L^2(\Omega)} \tag{2.26}$$

where Ω is a generic fluid domain. A regularisation term R was added to ensure well-posedeness of the problem. For this numerical approach, a Tikhonov regularisation was applied:

$$R(\mathbf{c}) = \frac{\alpha}{2} || \mathbf{c} ||^2_{L^2(\Omega)} \tag{2.27}$$

where the coefficient α determines how strongly the problem is regularised in the given norms. Following [30], the optimisation problem in Eq.2.25 was solved in its reduced formulation. In the reduced formulation the explicit PDE-constraints ($F(\mathbf{u}, \mathbf{c}) = 0$) is removed by implicitly enforcing the PDE in the functional. This strategy is common practice for solving PDE-constrained optimisation problems. Assuming the velocity $\mathbf{u}$ as an implicit function of the control variable $\mathbf{c}$ the functional Eq.2.26 can be then written as:

$$\hat{J}(\mathbf{u}) = J(\mathbf{u}(\mathbf{c})) + R(\mathbf{c}) \tag{2.28}$$

In this fashion, an evaluation of $\hat{J}$ for a specific control variable automatically invokes the Tape (Eq.2.24) solve to obtain the velocity $\mathbf{u}(\mathbf{c})$. This leads to the reduced optimisation problem

$$\min_{\mathbf{c}} \hat{J}(\mathbf{c}). \tag{2.29}$$

The advantage of adopting such formulation is that the reduced problem becomes an unconstrained optimisation problem and can hence be solved with an unconstrained optimisation method.

The minimisation problem 2.29 was solved with a gradient descent method, an iterative

optimization algorithm for finding a local minimum of a differentiable equation. At each iteration the algorithm computes the control variable c which approximates a minimiser of $\hat{J}$ and evaluates the derivative $\nabla_{\mathbf{c}}\hat{J}(\mathbf{c})$ to determine a direction along which the functional is decreasing. The approximation of $\nabla_{\mathbf{c}}\hat{J}(\mathbf{c})$ by finite differences would require computing as many finite differences as the dimension of the control variable, and for each of them solving Eq. 2.24. For moderate to large problem size, this can be quite costly [108]. To cope with this obstacle, the adjoint approach is used to efficiently compute the functional total derivative $\nabla_{\mathbf{c}}\hat{J}(\mathbf{c})$, at the approximate cost of one linearised Naviers-Stokes solve, namely solving the adjoint Navier-Stokes equations [30].

Here, a brief description of the adjoint method is reported. The total derivative of the functional in direction $\mathbf{c}$, using the chain rule, is:

$$\nabla_{\mathbf{c}}\hat{J}(\mathbf{c}) = \frac{\delta\hat{J}}{\delta\mathbf{u}}\frac{d\mathbf{u}}{d\mathbf{c}} + \frac{\delta\hat{J}}{\delta\mathbf{c}} \tag{2.30}$$

Computing directly $\frac{d\mathbf{u}}{d\mathbf{c}}$ is computationally expensive because the Naviers-Stokes model should be solved for each iteration of optimization. The adjoint approach, instead, eliminates this term by taking the derivative of the PDE equation $F(\mathbf{u},\mathbf{c}) = 0$:

$$\frac{\delta F}{\delta\mathbf{u}}\frac{d\mathbf{u}}{d\mathbf{c}} + \frac{\delta F}{\delta\mathbf{c}} = 0 \tag{2.31}$$

and substituting it into 2.30:

$$\frac{d\hat{J}}{d\mathbf{c}} = -\frac{\delta\hat{J}}{\delta\mathbf{u}}\left(\frac{\delta F}{\delta\mathbf{u}}\right)^{-1}\frac{\delta F}{\delta\mathbf{c}} + \frac{\delta\hat{J}}{\delta\mathbf{c}} \tag{2.32}$$

The expression $-\frac{\delta\hat{J}}{\delta\mathbf{u}}\left(\frac{\delta F}{\delta\mathbf{u}}\right)^{-1}$ may be understood in terms of linear algebra as the solution of the linear equation [108]

$$\left(\frac{\delta F}{\delta\mathbf{u}}\right)^{T}\lambda = -\left(\frac{\delta\hat{J}}{\delta\mathbf{u}}\right)^{T} \tag{2.33}$$

where T is the matrix transpose. Eq.2.33 is called *adjoint equation* and in this particular case it represents the adjoint Navier-Stokes equation. The *adjoint variable* λ is computed from Eq.2.33 and is then used to compute the total derivative

$$\frac{d\hat{J}}{d\mathbf{c}} = \lambda^{T}\frac{\delta F}{\delta\mathbf{c}} + \frac{\delta\hat{J}}{\delta\mathbf{c}} \tag{2.34}$$

Adopting a DO approach for the Var DA the *adjoint equation* is derived after the discretisation of the Navier-Stokes equation. The DO approach has the advantage that the discretised derivative is the exact derivative of the discretised system [30]. The discretised adjoint Navier-Stokes equation is not here reported for the sake of clarity. See [30] for a complete and rigorous derivation of the adjoint method for the Navier-Stokes model.

2.3.3 2D Tests

In the 2D setups shown in Figs. 2.6a and 2.6b, the quality of the Var solution was quantified and the effect of the regularisation term on the solution was investigated.

Observations

In these two examples, the reference solution $\mathbf{u}_{obs}$ was obtained by solving the Naviers-Stokes equations on the same domain, but assuming different boundary conditions. In *Hole*, $\mathbf{u}_{obs}$ was computed prescribing a velocity field in inlet Γ_{in} directed along the horizontal direction. This solution was forced on a *Tape* model where the velocity field in inlet was mainly directed along the vertical direction. The DA was limited on a restriction of the domain Ω by defining a suitable χ function (Fig. 2.8). In *2D-Ane* the reference solution was computed prescribing a zero velocity field at the outlet Γ_{out2} on the right side of the bifurcation. The velocity field $\mathbf{u}_{obs}$ was forced on a *Tape* model with zero pressure assumed at both outlets Γ_{out1} and Γ_{out2}. As in the previous case the DA was limited on a restriction of the domain Ω, defining a χ function which takes not null values around the bifurcation as shown (Fig. 2.9).

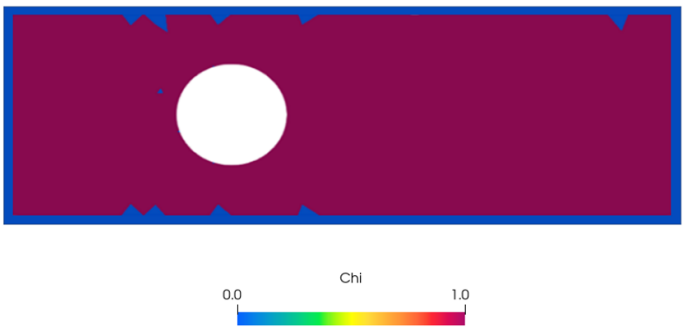

Figure 2.8: Representation of the χ function defined in *Hole*. χ assumes null value only along the domain boundaries.

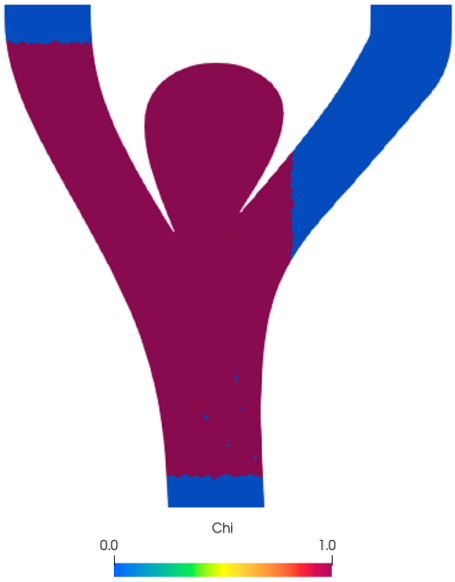

Figure 2.9: Representation of the the χ function defined in *2D-Ane*. χ takes not null value around the bifurcation.

Optimization algorithm

The minimisation problem 2.28 was solved with the Broyden-Fletcher-Goldbarb-Shanno (BFGS) algorithm, according to [30]. BFGS algorithm is an iterative method to solve unconstrained optimization problem. At each iteration, it computes the control variable $\mathbf{c}$ which minimises an approximation of $\hat{J}$ and estimates the derivative of the functional $\nabla_{\mathbf{c}}\hat{J}$ to determine a direction in which the functional is decreasing. The descent direction is determined by preconditioning the gradient with an approximation of the Hessian matrix of J. It brings a lower computational complexity than other methods (i.e. Newton's method). Actually, the L-BFGS algorithm, a limited-memory version of BFGS, was used for solving the optimisation problem. This variant is particularly suited to problems with very large number of variables. A schematic representation of the descent algorithm applied to the reduced minimisation problem 2.28 is shown in algorithm 1. The step length in algorithm 1 should be chosen to satisfy the Wolfe conditions which ensure the convergence of the method [109].
The L-BFGS algorithm is already implemented in the SciPy library which is automatically called by dolfin-adjoint library. The SciPy library provides many user-friendly numerical routines, such as the routine for optimization. The *minimize* function called from the SciPy library, allows to choose among several types of optimization methods for constrained and unconstrained optimization.

Algorithm 1: Schematic representation of the BFGS algorithm. Representation adapted from [30].

```
Set an initialization point for c;
for k = 0,1,... do
    Evaluate J(g) {requires solving the Tape and evaluating Eq. 2.28} ;
    Compute a search direction {requires solving Eq. 2.33 and evaluating Eq. 2.34} ;
    Set a step length so that J decreases {requires solving the Tape and evaluating
     Eq. 2.28} ;
    Update the control variable c ;
    if converged then
        return;
    end
end
```

2.3.4 3DVar

The variational data assimilation approach was then tested on real measurements of blood flow within a 3D cerebral aneurysm model, showed in Fig. 2.7.

Observation

The physical measurements were the same 4D flow data used to carry the transient simulations in SimVascular. Only the 10^{th} time frame of the 4D flow acquisition, correspondent to the highest flow time instant, was used for the 3D Var. The flow reconstruction was limited only at the highest flow time instant by solving the optimization problem assuming a steady state condition for the Navier-Stokes model. The observed velocity field $\mathbf{u}_{obs}$ was obtained by extracting the velocity measurements only within the restriction of the vessel model employed for the DA approach (Fig. 2.7). Later, the measurements were interpolated over the computational mesh and stored inside a finite element vector $\mathbf{u}_{obs}$ defined on the same finite element space for the velocity $\mathbf{u}$. Here, the DA was performed over the entire domain Ω.

Optimization algorithm

The L-BFGS algorithm already implemented in the SciPy library failed for the 3DVar formulation probably due to the increased complexity of the problem. Therefore, in order to overcome this problem an iterative gradient descent-like algorithm was implemented. The custom optimization algorithm exploited the dolfin-adjoint functions to keep the dependence of the functional J from the control variable (i.e the fictitious source term) $\mathbf{c}$, but different from

the adjoint approach it solves the Navier-Stokes equations at each iteration of the optimization, bringing a higher computational cost. Then, the iterative algorithm solves the Navier-Stokes equations, evaluates the functional $J(\mathbf{c})$, sets a step length and finally updates the control variable $\mathbf{c}$ (see algorithm 2).

Algorithm 2: Schematic representation of the custom optimization algorithm.

```
Set an initialization point for c;
for k = 0,1,... do
    Solve the Navier-Stokes model 2.24;
    Evaluate the functional J;
    Set a step length α ;
    Update the control variable c by a factor α δJ/δu ;
    if converged then
        return;
    end
end
```

Differently from algorithm 1, in algorithm 2 the step length was set manually in order to guarantee the convergence for each iteration.

2.3.5 Implementation and validation

The Naviers-Stokes solver implemented in FEniCS was first validated against SimVascular. A steady-state simulation on the same computational mesh, and with same boundary conditions was carried out using both solvers. The velocity and pressure fields obtained were compared qualitatively and quantitatively.

The variational DA here implemented, was first tested on 2D models (*Hole* and *Ane-2D*) with synthetic observations. The 2D set-up served as benchmark to test the robustness of the algorithm against the observation range, the variability between the solution and the observation, and the regularisation term $R(\mathbf{c})$ added to the functional J. The latter aspect was investigated running the algorithm for four different values of the regularisation parameter α. For each value the assimilated solution and the solution of the *forward model* were compared against the synthetic observation qualitatively and quantitatively.

The 3DVar allowed for reconstructing the blood flow within a cerebral aneurysm model from 4D flow data at the peak flow rate time frame. After estimating the quality of assimilated velocity against the measurements, a comparison among 3DVar and transient CFD and FSI at the peak flow rate time instant was carried out.

2.4 Expected results

4D flow guided-CFD and FSI simulations were expected to reconstruct the blood flow in the IA model with a good reliability concerning the 4D flow data. FSI simulations should enrich the hemodynamics evaluation highlighting the impact of wall deformability on blood flow. Notably, NonUniform-FSI should increase the reliability of the analysis by accounting for the pathological wall thinning of the aneurysm.

3DVar was expected to reconstruct the velocity field at the peak flow with an excellent consistency with 4D flow data. 3DVar should enable augmented spatial and time resolution of 4D flow measurements. The accuracy in blood flow prediction within the IA was expected to increase in 3DVar concerning High-resolution CFD. Overall, 3DVar would represent an innovative approach to overcome the lack of reliable model parameters, such as pressure estimations and vessel wall properties, which will ultimately lead to more accurate risk stratification for IAs.

Fig. 2.10 shows a synthetic representation of the total workflow carried out. The figure highlights the 4D flow based-BCs and the vessel thickness assumed in Uniform- and NonUniform-FSI. An illustrative representation of the 3DVar and its comparison with the 4D flow guided-CFD is also displayed.

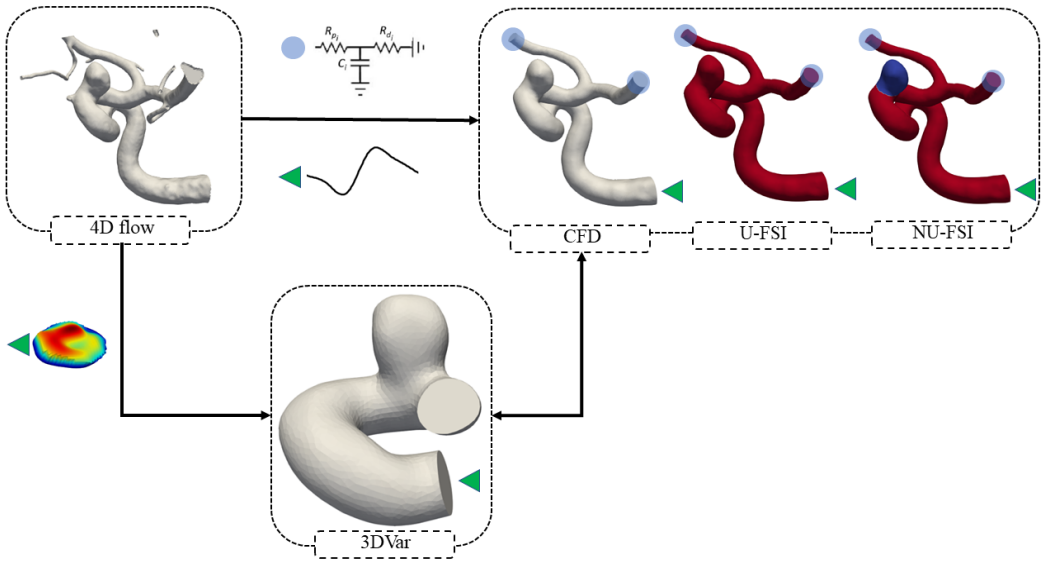

Figure 2.10: Schematic representation of the total workflow carried out. 4D flow based-CFD and FSI (Uniform-FSI and NonUniform-FSI) simulations were performed applying BCs extracted from 4D flow measurements. In NonUniform-FSI a thinning of the aneurysm wall was modeled (blue region). 3DVar was performed to reconstruct blood flow from the highest flow rate time frame of 4D flow, applying in inlet a velocity profile extracted from the measurements. The assimilated solution was compared with the transient-CFD.

Chapter 3

Results

In this chapter, the results obtained from the 4D flow guided-CFD and FSI simulations carried in SimVascular and from the implemented Var DA will be illustrated. In the first part, the numerical results will be compared with the 4D flow data, and the role of CFD and FSI simulations in assessing IA hemodynamics will be investigated. The second part will focus on the results from the numerical experiments carried to test the Var DA. Special consideration will be given to the 3D Var formulated to reconstruct the flow conditions in a real IA from 4D flow data.

3.1 4D flow based-CFD and FSI simulations

As already mentioned in Chapter 2, one rigid-wall simulation (CFD) and two deformable-wall simulations (Uniform-FSI, NonUniform-FSI) were carried out in SimVascular. In NonUniform-FSI, the vascular model was modified by an ad-hoc python script so that SimVascular recognized a new wall region around the aneurysm. In this way, a specific thickness was defined for the aneurysm to account for the pathological wall thinning (Fig. 3.1). All the following analyses refer to the last cardiac cycle simulated in order to guarantee solution periodicity and mitigation of transient effect.

3.1.1 Validation against 4D flow data

The CFD and FSI results were first compared against the 4D flow measurements to quantify the agreement between numerical results and clinical data. Outlet flow rates over time and velocity color maps were analysed.

Overall, a good match was found between time-dependent outlet flow rates with CFD,

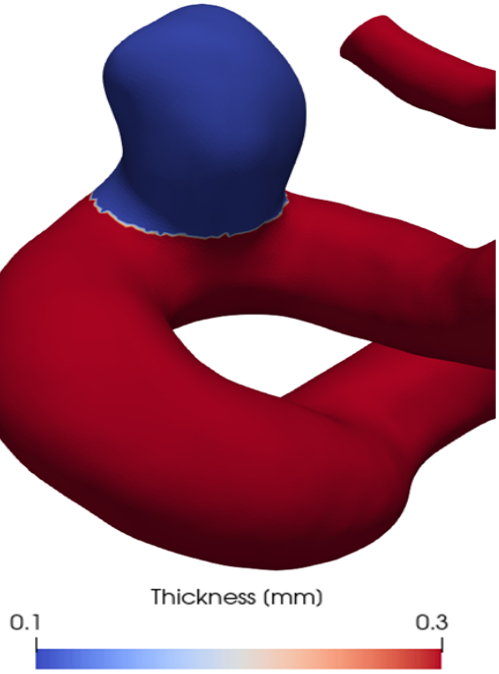

Figure 3.1: Contour map of the wall thickness defined on the computational model for the NonUniform-FSI. The wall thickness pass from $300\mu m$ for the parent vessel to $100\mu m$ for the aneurysm.

NonUniform-FSI and 4D flow data (Fig. 3.2). The largest difference with 4D flow in time-averaged flow rate was $\sim$ 0.42 L/min ($\sim$ 45%) at the Outlet Small in both NonUniform-FSI and CFD (Table 3.1). This discrepancy can be explained with the following reason: in 4D flow the conservation of mass is not satisfied due to the noise in the measurements therefore, in order to overcome this limitation, the RCR at the Outlet Small was calibrated with respect to an outflow rate estimated as the difference between the Inlet flow rate and the Outlet Large flow rate. The Outlet Large flow rate curve seems fully consistent with 4D flow data in both CFD and NonUniform-FSI. Comparing CFD and NonUniform-FSI, the outflow predicted at the Outlet Small by NonUniform-FSI is slightly higher than CFD in the first half of the cardiac cycle. In the following half the two curves are almost overlapped. At Outlet Large, instead, the outflow predicted is always lower than CFD. Both observations are related to the wall deformability accounted in the NonUniform-FSI. Indeed, at the peak flow, the vessel enlarging seizes part of the blood, which gives back after the peak, when the vessel recovers its original configuration. Nevertheless, looking the at the time-averaged flow rate shown in Table 3.1, the predicted outflow rate in NonUniform-FSI was 2.1% higher at the outlet small and 2.5% lower at the Outlet Large with respect to CFD.

In Fig. 3.3 a qualitative comparison of velocity color maps between 4D flow, CFD and

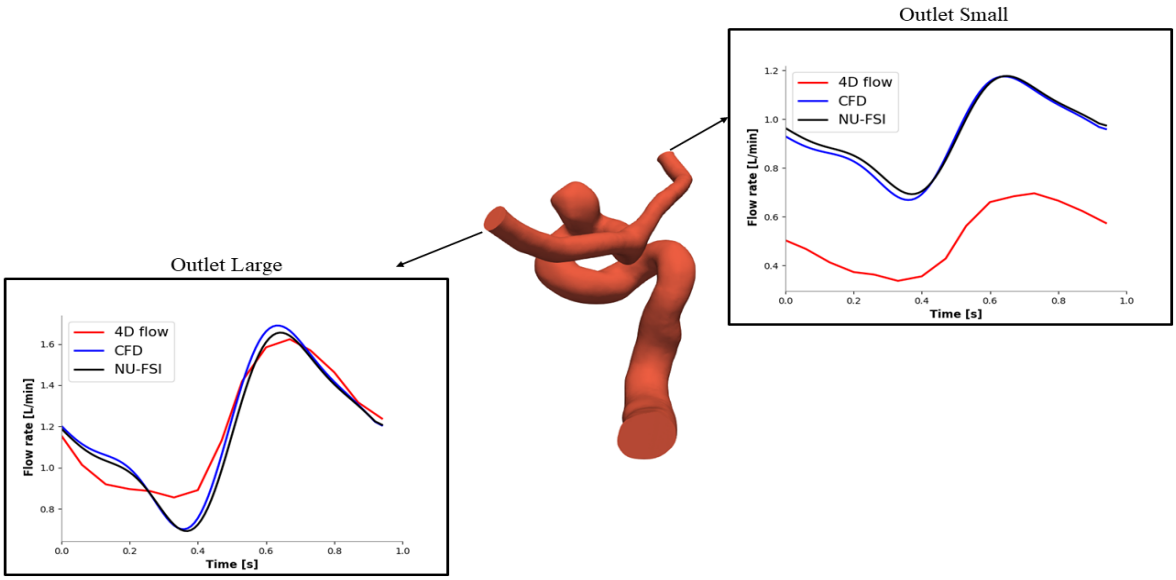

Figure 3.2: Outflow rate at Outlet Large and Outlet Small. Comparison between CFD and NonUniform-FSI (NU-FSI).

Outlet	$\bar{Q}_{4Dflow}$	$\bar{Q}_{CFD}$	$\bar{Q}_{NU-FSI}$
Small	0.51	0.92	0.94
Large	1.19	1.20	1.17

Table 3.1: Time-averaged outflow rate in [L/min] for 4D flow, CFD and NUniform-FSI.

NonUniform-FSI is provided at three distinct time instants (T1, T2 and T3) and on three different planes (P1, P2, P3 and P4). In the top row of the figure, colour-encoded velocity streamlines are shown within the aneurysm at the lowest flow rate time instant (T1), at the highest flow rate time instant (T3) and at a time instant in the middle (T2) for 4D flow and CFD. Both techniques depict a complex flow in the aneurysm volume. As expected, the vorticity within the aneurysm increases at high flow rate time instants. The velocity field seems consistent between 4D flow and CFD at each time instant, especially at the neck and along the parent vessel, where the velocity is usually higher than inside the aneurysm. Nevertheless, streamlines from 4D flow in the aneurysm region are noisy, reducing the information quality, particularly at T3. This is probably due to a low spatial resolution which affects 4D flow measurements. In the middle and the bottom rows of the figure, velocity colour maps extracted from an upstream (P1) and a downstream (P2) planes the aneurysm and from two cross-sectional planes (P3 and P3) for 4D flow, CFD and NonUniform-FSI are shown. A good agreement between 4D flow and both CFD and NonUniform-FSI can be appreciated along P1 and P2 at low flow rate time instants (T1 and T2). At T3 the discrepancies are more evident, mainly in P2, where the velocity profile in 4D flow seems directed to the bottom

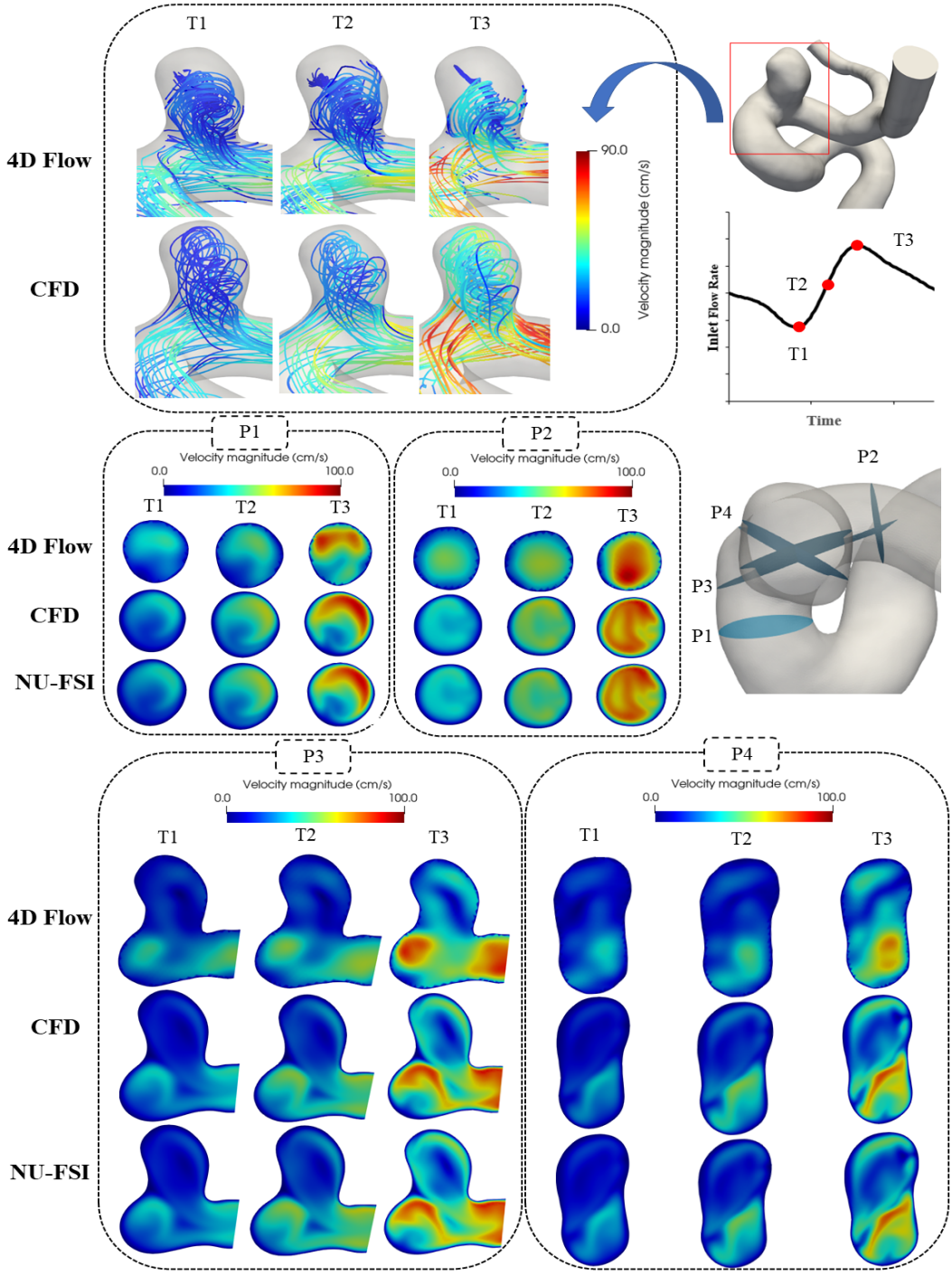

Figure 3.3: Qualitative comparison among 4D flow, CFD and NonUniform-FSI (NU-FSI). **Top row**: color-encoded velocity streamlines in 4D flow and CFD within the aneurysm at three distinct time instants are shown together with a representation of the 3D geometry and time points in the cardiac cycles. **Middle row**: Velocity colour maps on planes upstream and downstream the aneurysm for 4D flow, CFD and NU-FSI at three distinct time points are shown with cross-sectional planes representation. **Bottom row**: Velocity colour maps on two cross-sectional planes within the aneurysm for 4D flow, CFD and NU-FSI at three distinct time points are shown.

side of the vessel and not toward the extrados as in CFD and NonUniform-FSI. In P3 and P4 a consistent velocity field was found along the parent vessel section, for each time instant. Inside the aneurysm, instead, the agreement is remarkable at T3 when the velocity is higher and both CFD and NonUniform-FSI replicate the inflow jet visible in 4D flow.

The good agreement between numerical simulations (CFD and NonUniform-FSI) and 4D flow is confirmed by the normalized root mean squared error (RMSE) shown in Tables 3.2 and 3.3, with values ranging from 0.115 to 0.185, and from 0.107 and 0.178 for CFD and Uniform-FSI, respectively.

Nevertheless, NonUniform-FSI does not seem to bring any further improvement in the velocity field prediction by comparing the velocity colour maps and the RMSE with the CFD. As shown in Fig 3.4, only a slight difference exists in the velocity field for CFD and NonUniform-FSI. For this reason, from now on, NonUniform-FSI will be excluded in any analysis concerning the velocity. Accordingly, Uniform-FSI will be excluded too, since a increased aneurysm wall thickness is expected to impact less on the intra-aneurysmal velocity field.

Cross-sectional Planes	T1	T2	T3
P1	0.148	0.168	0.168
P2	0.172	0.185	0.161
P3	0.170	0.144	0.139
P4	0.115	0.129	0.137

Table 3.2: RMSE normalized by the maximum 4D flow velocity between CFD and 4D flow velocity magnitude contours on the selected planes for the specified time points.

Cross-sectional Planes	T1	T2	T3
P1	0.145	0.158	0.166
P2	0.169	0.177	0.160
P3	0.168	0.171	0.137
P4	0.112	0.122	0.135

Table 3.3: RMSE normalized by the maximum 4D flow velocity between Uniform-FSI and 4D flow velocity magnitude contours on the selected planes for the specified time points.

3.1.2 CFD, Uniform-FSI and NonUniform-FSI: qualitative and quantitative comparison

As shown in Fig. 3.4, wall deformability only minimally impacts the velocity field within the IA. Accordingly, the comparison between CFD and FSI (Uniform-FSI and NonUniform-FSI) simulations focused on the pressure fields over all cardiac cycle, which, on the other hand, was largely influenced by wall properties.

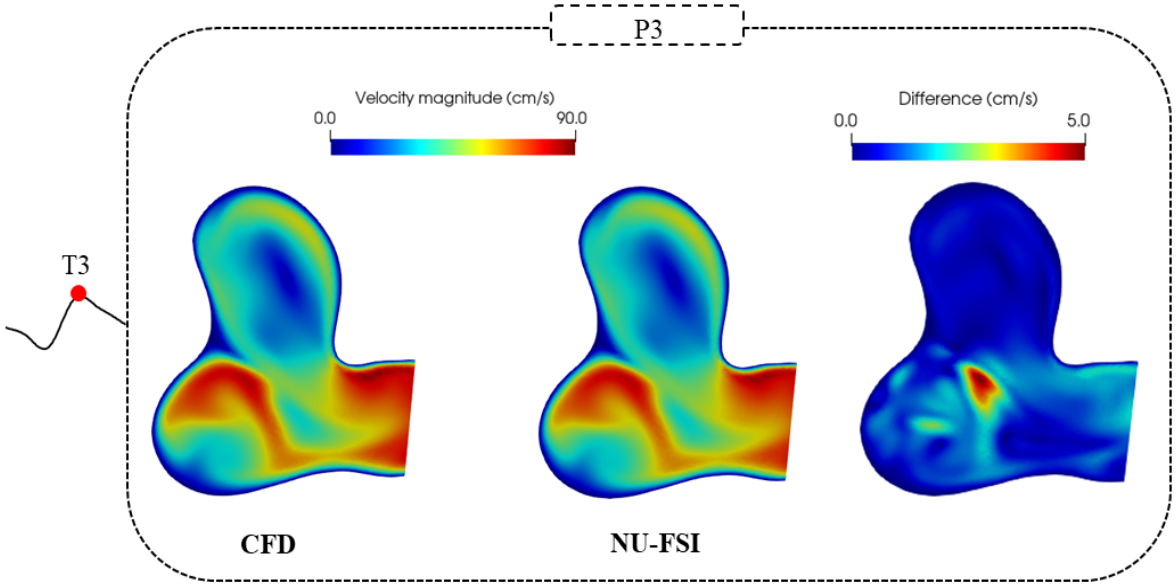

Figure 3.4: Velocity colour maps along a cross-sectional plane of the aneurysm at the highest flow rate time instant for CFD and Uniform-FSI compared with a colour map of the difference in velocity magnitudes returned by these two methods.

Pressure field was evaluated along the aneurysm surface highlighted in Fig. 3.5a and surface-averaged pressure was plotted over time for CFD and Uniform-FSI (Fig. 3.5a). In Uniform-FSI the pressure is higher over all cardiac cycle. The maximum pressure difference $\Delta P = P_{Max} - P_{Min}$ is 31.87 mmHg in Uniform-FSI and 33.93 mmHg in CFD ($\sim$ +6%). The deviation in ΔP may be related to the damping of blood flow due to the wall deformability in Uniform-FSI. The curves in Fig. 3.5b show plane-averaged values of the pressure computed along planes upstream and downstream of the aneurysm in CFD and Uniform-FSI. As expected, the peak-to-peak pressure difference ($\Delta P_{Up-Down}$) is reached at the highest flow time instant, when more blood flow within the aneurysm, in both CFD and Uniform-FSI. Notably, the maximum $\Delta P_{Up-Down}$ in FSI and CFD are 1.68 mmHg and 1.71 mmHg ($\sim$ +1.4%), respectively. The deviation in $\Delta P_{Up-Down}$ may still be related to the wall deformability assumed in Uniform-FSI. Pressure contours compared at three different time points in the cardiac cycle are reported in Fig. 3.5c. The difference between the pressure computed in CFD and Uniform-FSI is minimal and more appreciable only at the lowest flow rate time instant. Here, the pressure in Uniform-FSI is higher, probably due to the vessel wall that retrieves its original configuration after the flow peak. Accordingly, in Fig. 3.6 Uniform-FSI and NonUniform-FSI are compared. NonUniform-FSI does not seem to bring any additional information in pressure field along the aneurysm model. The aneurysm surface-averaged maximum pressure difference $\Delta = P_{Max} - P_{Min}$ is only $\sim$ 0.46% lower in

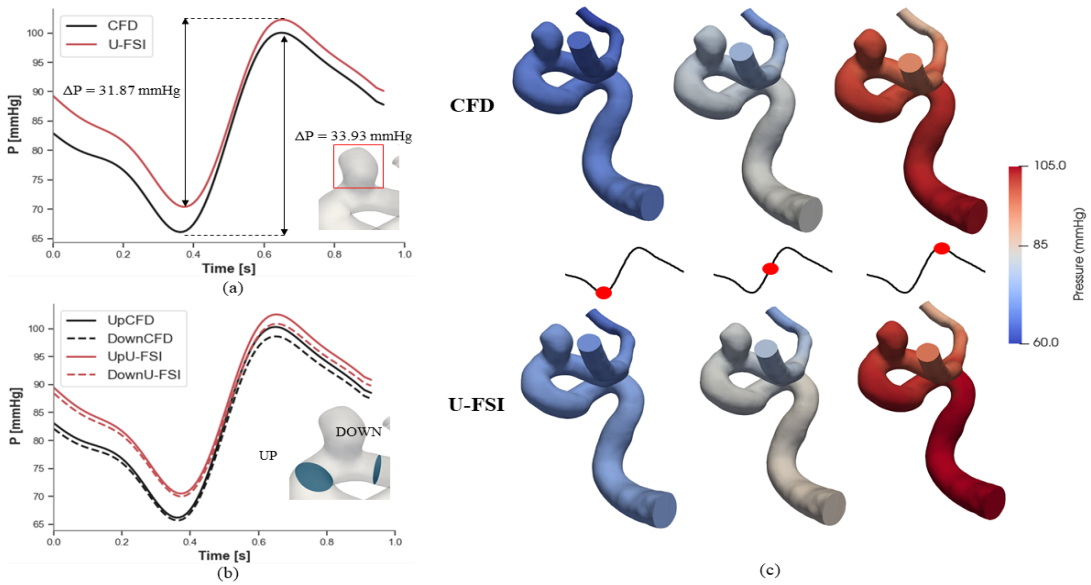

Figure 3.5: Quantitative and qualitative comparison of pressure field for CFD and Uniform-FSI. (a) Aneurysm surface-averaged pressure over time in CFD (black line) and Uniform-FSI (red line). Highest to lowest flow rate pressure differences are highlighted in the figure for both methods. (b) Surface-averaged pressure between a section upstream (continuous line) and downstream (dashed line) the aneurysm for CFD (black) and Uniform-FSI (red). (c) Pressure contours at three distinct time points over all the model for CFD and Uniform-FSI.

NonUniform-FSI, while $\Delta P_{Up-Down}$ is $\sim$ 0.33% lower. The pressure contours (Fig. 3.6c) confirm the aforementioned statement, since any difference in pressure field for Uniform-FSI and NonUniform-FSI is appreciable for all three time instants. Vessel wall displacements and maximum principle strain fields were calculated for Uniform- and NonUniform-FSI. In Fig. 3.7 displacement contour maps for three distinct time points are shown. The posterior side of the aneurysm is the most affected region by high displacements. This behaviour is accentuated in NonUniform-FSI where the pathological wall thinning causes a change in the displacement field. Tables 3.4 and 3.5 confirm these observations, with a maximum displacement of 0.042cm of the aneurysm wall in Uniform-FSI which doubled in NonUniform-FSI. Accordingly, in Fig. 3.8 strain contour maps at three distinct time points are shown. In Uniform-FSI (top row) the strains are under 15% for each time point according to Table 3.4. The strain field is almost uniform all over the model apart from the aneurysm neck, where a small increment in the strain field occurs. In NonUniform-FSI (bottom row), this behaviour is accentuated with a maximum strain increment on the aneurysm neck up to the 65% at the highest flow rate time instant (Table 3.5). In general, the thinning assumption of the aneurysm wall in NonUniform-FSI establishes an averaged increment of the $\sim$ 47% in the strain field along the aneurysm wall, in accordance with the displacement growth displayed in Fig.3.7.

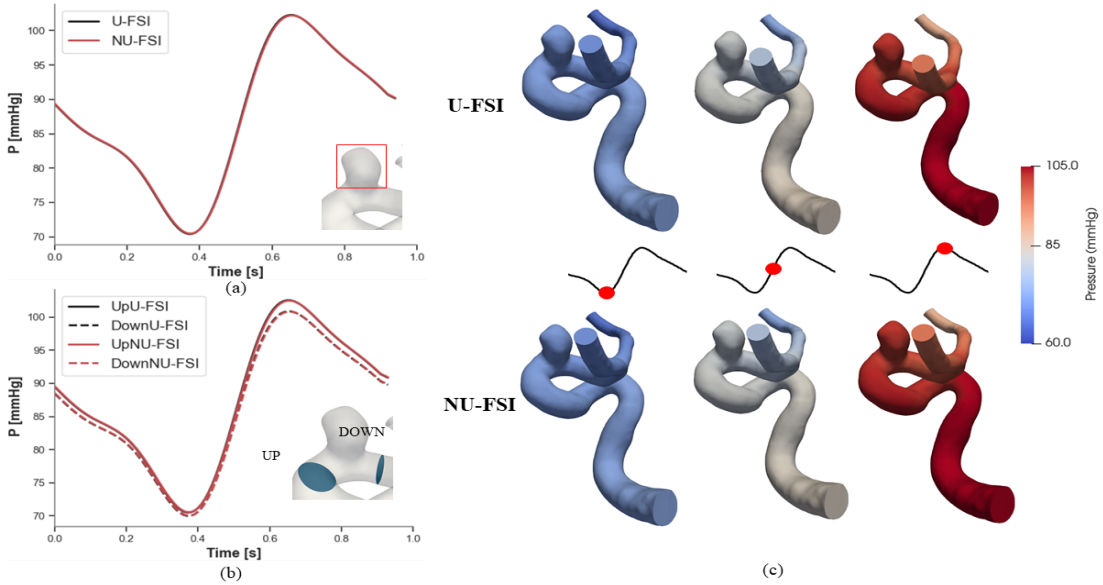

Figure 3.6: Quantitative and qualitative comparison of pressure field for Uniform-FSI and NonUniform-FSI. (a) Aneurysm surface-averaged pressure over time in Uniform-FSI (black line) and NonUniform-FSI (red line). Highest to lowest flow rate pressure differences are highlighted in the figure for both methods. (b) Surface-averaged pressure between a section upstream (continuous line) and downstream (dashed line) the aneurysm for Uniform-FSI (black) and NonUniform-FSI (red). (c) Pressure contours at three distinct time points over all the model for Uniform-FSI and NonUniform-FSI.

		T1	T2	T3
Displacement				
	Maximum [cm]	0.029	0.034	0.042
	95^{th} percentile [cm]	0.026	0.024	0.033
Strain				
	Maximum [%]	10.1	11.6	14.9
	95^{th} percentile [%]	7.57	8.69	11.0

Table 3.4: Maximum and $95th$ percentile of displacement and strain field computed at the aneurysm and the proximal parent vessel wall for Uniform-FSI.

		T1	T2	T3
Displacement				
	Maximum [cm]	0.057 (+49%)	0.065 (+48%)	0.082 (+48%)
	95^{th} percentile [cm]	0.040 (+44%)	0.046 (+43%)	0.058(+43%)
Strain				
	Maximum [%]	28.0 (+64%)	32.2 (+64%)	42.5 (+65%)
	95^{th} percentile [%]	14.3 (+47%)	16.4 (+47%)	21.1 (+47%)

Table 3.5: Maximum and $95th$ percentile of displacement and strain field computed at the aneurysm and the proximal parent vessel wall for NonUniform-FSI with the increment with respect the Uniform-FSI.

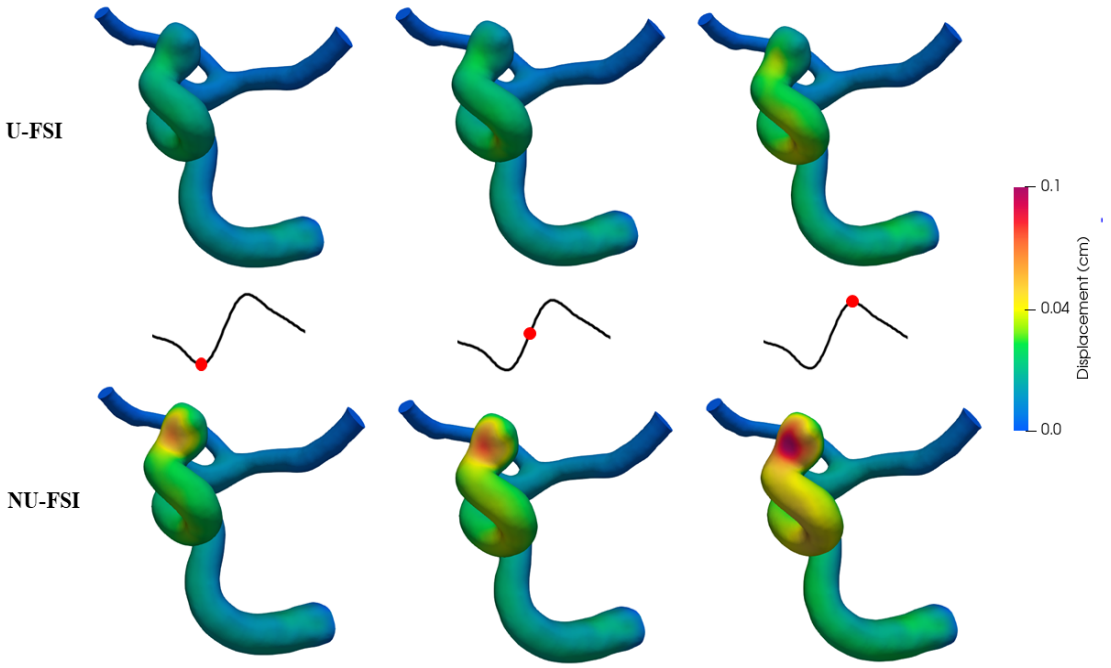

Figure 3.7: Displacement contour maps at three distinct time points for Uniform-FSI and NonUniform-FSI.

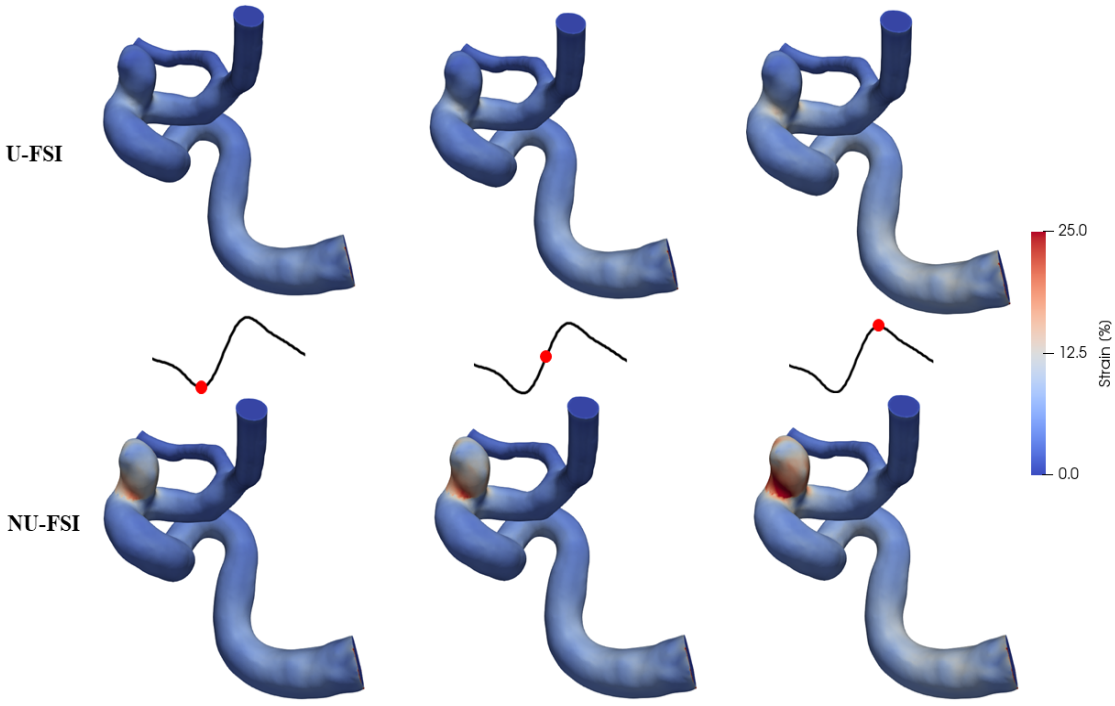

Figure 3.8: Strain contour maps at three distinct time points for Uniform-FSI and NonUniform-FSI.

3.1.3 Hemodynamics evaluation in intracranial aneurysm: WSS and OSI

From the CFD results, WSS, TAWSS and OSI were extracted. This analysis excludes FSI results, since they did not add relevant information on velocity field within the aneurysm.

Fig 3.9 shows the WSS magnitude contours map at three different time instants, and TAWSS and OSI contours maps. The first row focuses on the whole model, whereas in the second row, a zoom around the aneurysm region is provided. As expected, WSS magnitude increases at high flow rate time instants. The bifurcation of ICA, MCA and ACA is the most affected region by high WSS at each time instant. The TAWSS contours map is consistent with the instantaneous WSS magnitude distributions. High OSI values (generally > 0.5) are associated with disturbed flow fields. Here, OSI keeps values lower than 0.2 all over the anatomy. Only small regions downstream ICA curvatures are affected by OSI grater then 0.5. Accordingly, these regions results affected by low WSS value.

Focusing on the second row, the aneurysm protrudes from a region affected by high WSS values. On the other hand, over the aneurysm surface the WSS are overall low. Only the left-posterior side of the aneurysm surface is characterized by increased WSS values, with a maximum value of 27.90 Pa and a 95^{th}percentile of 16.60 Pa at the highest flow rate time instant as shown in Table 3.6. Remarkably, the OSI is closed to zero all over the aneurysm

	T1	T2	T3
Maximum WSS [Pa]	11.35	19.36	27.90
95^{th} percentile WWS [Pa]	6.08	9.84	16.60

Table 3.6: Maximum and 95^{th} percentile along the aneurysm surface at three distinctive time point over the cardiac cycle.

surface. Fig. 3.10 shows the 95^{th}percentile of the WSS computed along all the model over time. The WSS varies significantly over the cardicac cycle oscillating between a minimum of 10.51 Pa and a maximum of 22.22 Pa. It is to be noted that WSS varies in accordance to the flow rate.

3.2 Data Assimilation

The finite element solver implemented in FEniCS was validated against SimVascular. Next, the Var DA approach was tested on two numerical experiments. The experiments consist of two 2D domains where a reference velocity field was pre-computed. Lastly, the DA approach was formulated for a 3D domain (3DVar) and tested in reconstructing the flow conditions in an aneurysm model from 4D flow data. The assimilated solution was compared with the high-resolution CFD, carried in SimVascular, to further assess the quality of the DA approach.

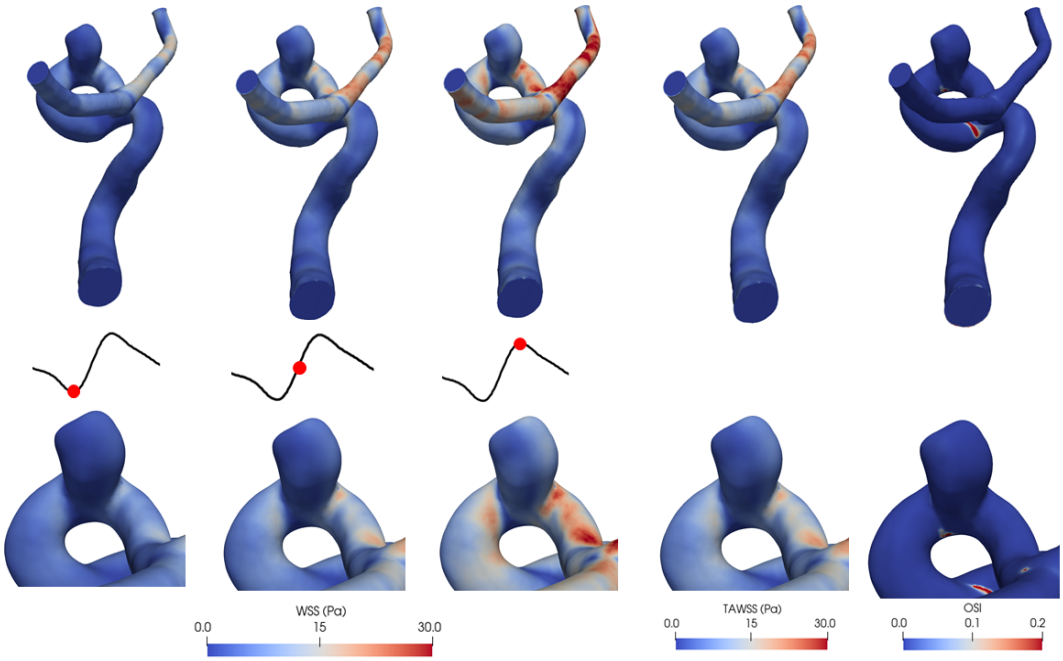

Figure 3.9: WSS contours map at three distinctive time points of the cardiac cycle, TAWWS and OSI contour map. **First row:** representation of the entire geometry. **Second row:** zoomed on the aneurysm region.

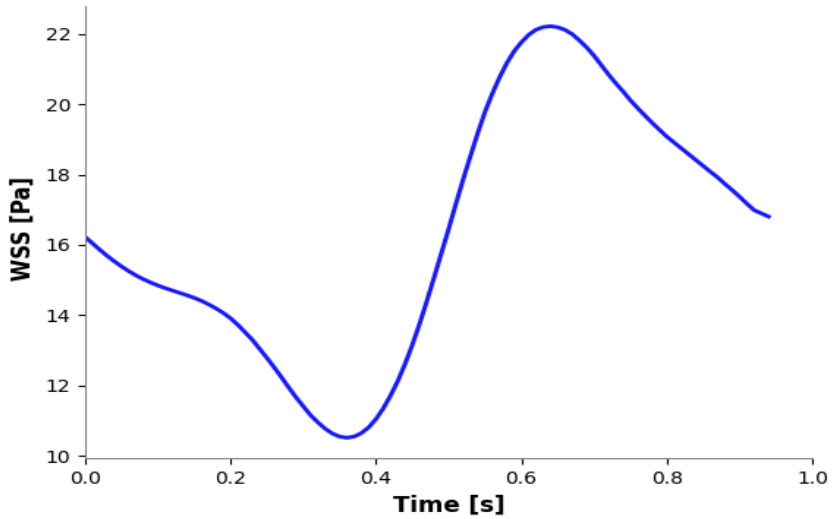

Figure 3.10: 95^{th}*percentile* of WSS magnitude computed along the entire model surface over the cardiac cycle.

3.2.1 Custom Navier-Stokes solver validation

Two steady-state CFD simulations were carried out on the same mesh and applying the same BCs (plug velocity in inlet and zero pressure in outlet), one using Simvascular

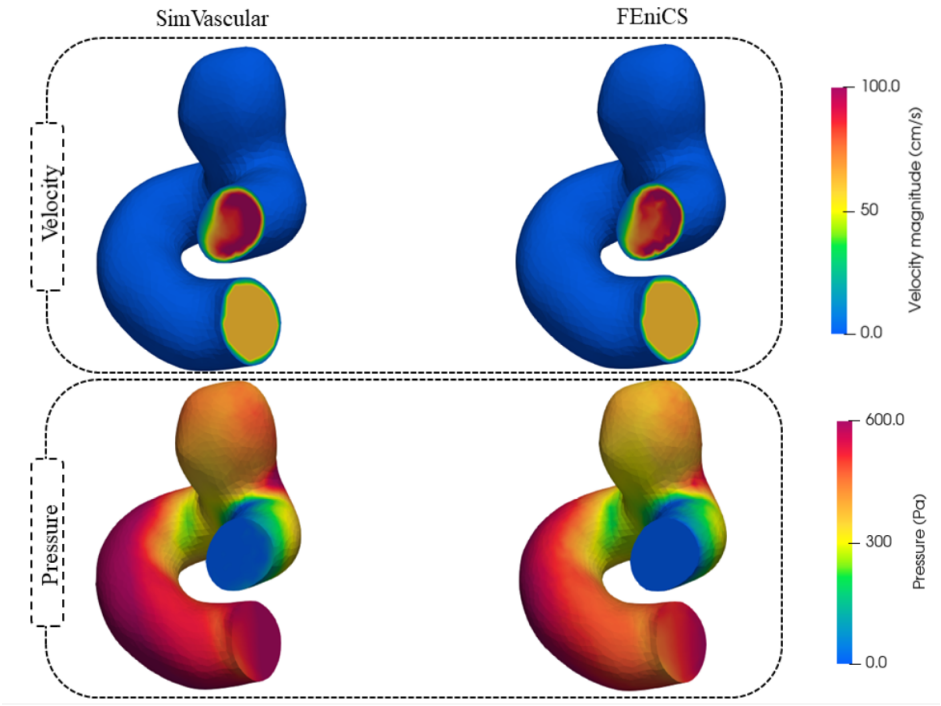

Figure 3.11: Pressure and velocity field calculated in SimVascular (left) and in FEniCS (right) by the ad hoc implemented solver.

and the other using the ad-hoc finite element solver implemented in FEniCS. Both solvers treat steady-state problems with a transient numerical formulation applying steady BCs. The simulations were run for 100 iterations in order to get an asymptotic solution. The velocity field in inlet and outlet, and pressure field obtained in FEniCS are consistent with SimVascular, as showed in Fig. 3.11. The maximum and the 95^{th} percentile of both velocity and pressure fields for FEniCS and SimVascular are compared in Table 3.7. The discrepancies between those values are negligible, and probably related to the different stabilization term (SUPG-PSPG, Streamline upwind Petrov-Galerkin pressure-stabilizing Petrov-Galerkin) and time integration algorithm used in SimVascular. During the solver validation, it was noted that 10 time iterations were sufficient to get an asymptotic solution. Therefore, the Variational DA formulation was implemented according to that.

	FEniCS	SimVascular
Maximum velocity [cm/s]	126.36	117.36
95^{th} percentile velocity [cm/s]	77.17	77.97
Maximum pressure [Pa]	641.96	713.51
95^{th} percentile pressure [Pa]	591.29	660.11

Table 3.7: Comparison between velocity magnitude and pressure obtained in FEniCS and SimVascular. Maximum and 95^{th} percentile of velocti magnitude and pressure is reported.

3.2.2 2D numerical experiments

The test environments were created by generating the observations ($\mathbf{u}_{obs}$) from a numerical reference solution. In *Hole*, the numerical reference solution differed from the *Tape* solution for the inlet boundary condition. While in *Ane-2D*, the observations were generated from a reference solution with different outlet BC on the *Tape*.

As mentioned in Chapter 2, in both *Hole* and *Ane-2D* the DA was limited to an area of the domain by defining a suitable χ function. In *Hole* the DA was performed over the interior part of the domain excluding the boundaries. In *Ane-2D* the DA focused on the bifurcation. The convergence of the Var DA algorithm was highly dependent on χ function definition, and therefore, on the extension of the domain where DA was performed. In *Ane-2D*, the algorithm was tested with several χ functions by varying the extension of the sub-domain where χ takes not null values. The sensitivity of the Var DA approach implemented was tested against the regularisation parameter α. Fig. 3.12 compares DA assimilation in *Hole* domain for three different α values. The influence of the regularisation term was investigated by varying alpha between 1 and 10^{-6}. In Fig. 3.12 only the attempts with $\alpha = 10^{-4}$, 10^{-2} and 1 are displayed. The reconstructions works well for $\alpha < 10^{-2}$, then the quality starts to reduce. For $\alpha = 10^{-4}$ and 10^{-2} the DA was able to reconstruct the symmetry in velocity field which characterizes the observation. By increasing α, the functional value $J + R$ at the optimal point (i.e. last optimisation iteration) increases, confirming the reduction of DA effectiveness. As shown in Table 3.8, the RMSE of velocity magnitude between the assimilated solution and the observation passes from 0.22mm/s to 0.37mm/s increasing alpha. The RMSE improves by 41% between the assimilated solution at optimal point ($it = 12$) with $\alpha = 10^{-4}$ and the solution before the optimisation ($it = 0$). Notably, the RMSE for $\alpha = 10^{-2}$ (0.19mm/s) is slightly better even if the functional value at the optimal point was higher. By plotting the control $\mathbf{c}$ over the domain, the most affected regions by the assimilation procedure can be distinguished. Here, the control magnitude is a measure of the effectiveness of the assimilation procedure in forcing the numerical solution to follow a target solution. In this case, the control acts mostly close to the inlet of the domain. Notably, increasing α, the similarity with the observation decreases and the control reduces its effect on the assimilation. For *Hole*, the optimisation started with a (J+R) equal to 26374.67 and was terminated when the relative change of the functional between consecutive iteration dropped below 10^{-4} or the number of iterations exceed 4000. In Fig. 3.13 a comparison between the solution at $it = 0$, the reference solution and the assimilated solution for $\alpha = 10^{-4}$ is provided. The DA algorithm was able

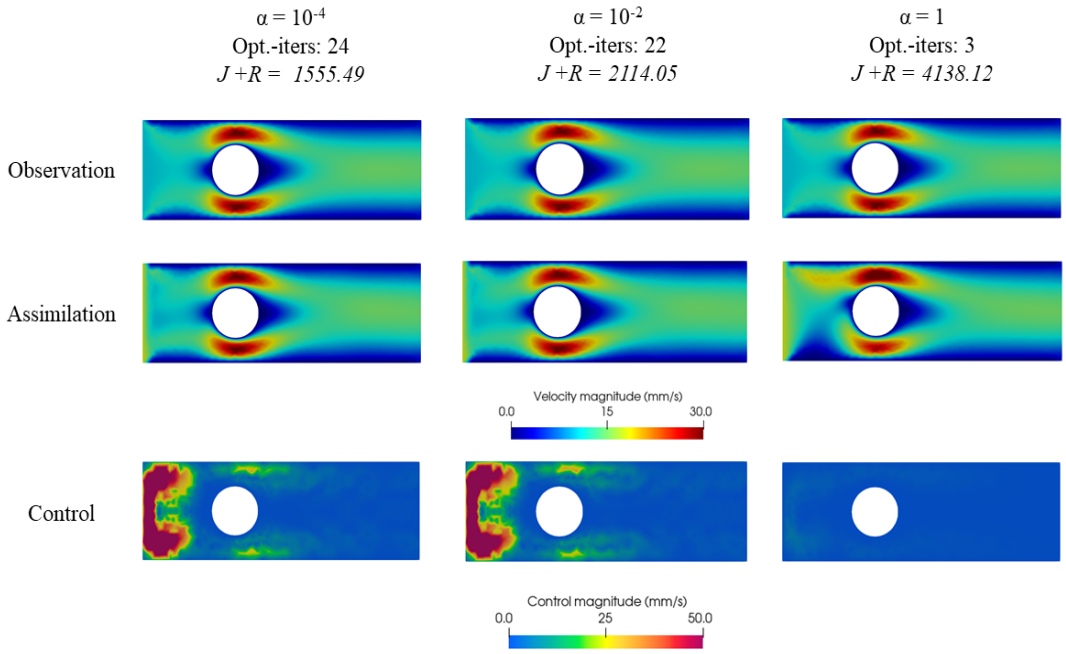

Figure 3.12: Velocity magnitude contour maps of the reference and the assimilated solution with control magnitude color map for *Hole*. **First row:** number of iterations for the optimisation solver to converge (*Opt.-iters)*) and the functional value plus the regularisation term at the optimal point (*J+R*). **Second and third rows:** assimilated velocity is compared to the numerical observations by means of contour maps. **Fourth row:** the control magnitude **c** at the optimal point is displayed over the domain.

	$it = 0$	$\alpha = 10^{-4}$	$\alpha = 10^{-2}$	$\alpha = 1$
RMSE [mm/s]	0.39	0.22	0.19	0.37

Table 3.8: Root Mean Squared Error of the velocity magnitude between the assimilated solution and the reference solution varying α compared with the Root Mean Squared Error before the optimization ($it = 0$) in *Hole*

to reconstruct the symmetry of the flow field on a CFD solution characterized instead by an asymmetrical flow field. Focusing on the inlet, the effect of the control in forcing the reference solution only at the interior domain is appreciable. The main difference in flow field between the CFD (solution at $it = 0$) and the reference solution are located at the inlet. Indeed, the control **c** acts mostly in this region (Fig. 3.12 last row).

The results of the assimilation procedure varying the regularisation parameters α for *Ane-2D* are presented in Fig. 3.14 in a consistent way with respect to *Hole*. As shown in the previous example, the flow reconstruction allows to recover the observations for $\alpha < 10^{-2}$, then the quality starts to reduce. For $\alpha = 10^{-4}$ and 10^{-2} the DA was able reconstruct the asymmetric velocity field which characterizes the observation by forcing a null velocity along the left branch of the bifurcation. By increasing α, the functional value $J + R$ at the optimal point increases,

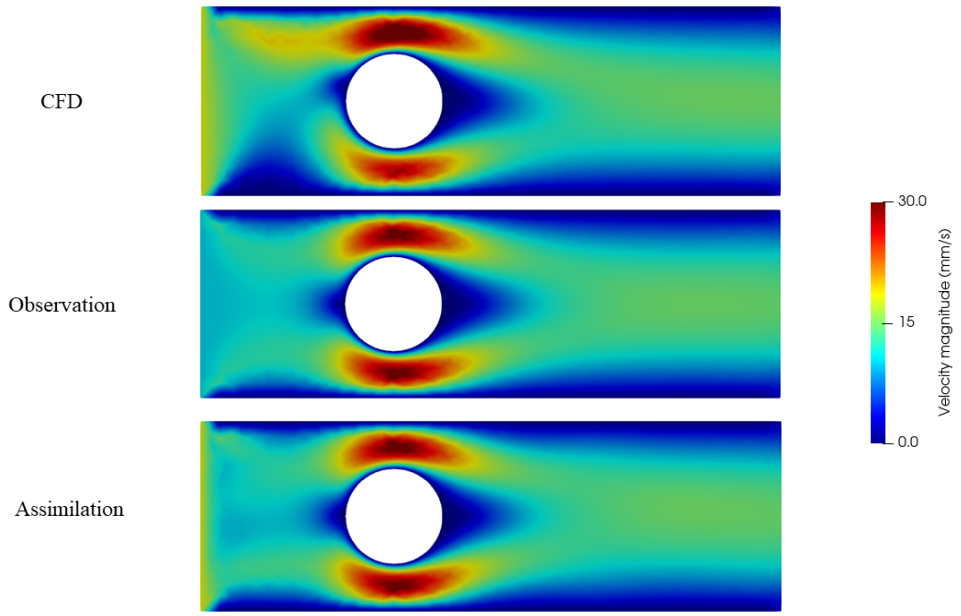

Figure 3.13: Comparison of the velocity magnitude contour maps among CFD (solution at *it=0*), observation and assimilated solution at optima point (*it=12*) for $alpha = 10^{-4}$.

confirming the reduction of DA effectiveness. The RMSE of velocity magnitude between the assimilated solution and the observation goes from 0.069mm/s to 0.115mm/s increasing α as shown in Table 3.9. The RMSE improves by 40% between the assimilated solution at optimal point ($it = 63$) with $\alpha = 10^{-4}$ and the solution before the optimisation ($it = 0$). Nevertheless, in this experiment the RMSE for $\alpha = 10^{-2}$ is slightly better than for $\alpha = 10^{-4}$, accordingly to the previous experiment. This result is confirmed by the velocity contour map in Fig. 3.14. For $\alpha = 10^{-4}$ the flow reconstruct introduces numerical artifacts that appear as discontinuities in the velocity field at the inlet and right outlet. The discontinuities are exactly located at the boundaries of χ domain. Instead, for $\alpha = 10^{-2}$ the assimilated solution looks smoother over the whole domain. In the last row of Fig. 3.14 the control $\mathbf{c}$ is displayed over the domain varying α. The control affects mostly the inlet and the outlets of the assimilation domain and its effect decreases when α increases. For *Ane-2D*, the optimisation started with a $J+R$ equal to 24.9 and was terminated when the relative change of the functional in one iteration dropped below 10^{-4} or the number of iterations exceed 4000. In Fig. 3.15 a comparison between the solution at $it = 0$, the reference solution and the assimilated solution for $\alpha = 10^{-4}$ is provided. The DA algorithm was able to force a almost null velocity field along the left branch of the bifurcation on a CFD solution characterized by a symmetrical velocity field. As mentioned above, the effect of the control was so strong that it introduced discontinuities in the velocity

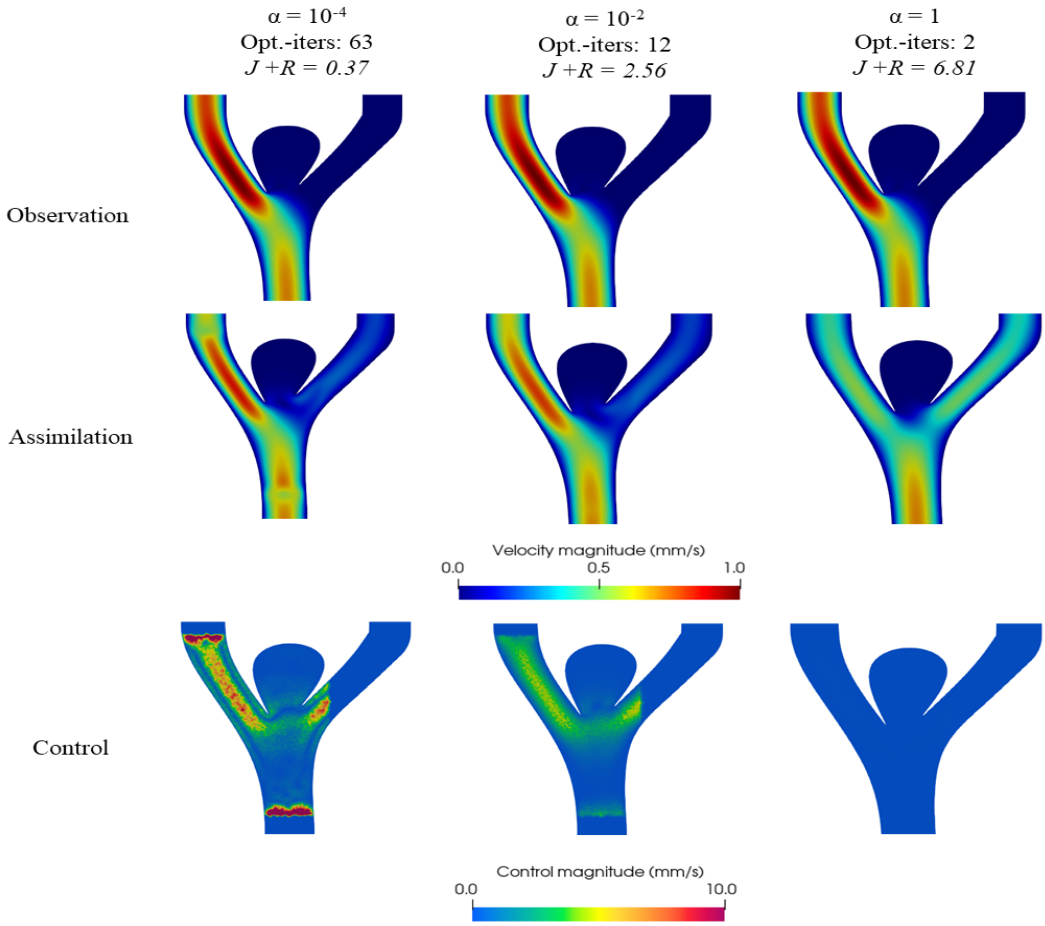

Figure 3.14: Velocity magnitude contour maps of the reference and the assimilated solution with control magnitude color map for *2D-Ane*. **First row:** number of iterations for the optimisation solver to converge (*Opt.-iters)*) and the functional value plus the regularisation term at the optimal point (J+R). **Second and third rows:** assimilated velocity is compared to the numerical observations by means of contour maps. **Fourth row:** the control magnitude **c** at the optimal point is displayed over the domain.

	$it = 0$	$\alpha = 10^{-4}$	$\alpha = 10^{-2}$	$\alpha = 1$
RMSE [mm/s]	0.116	0.069	0.068	0.115

Table 3.9: Root Mean Squared Error of the velocity magnitude between the assimilated solution and the reference solution varying α compared with the Root Mean Squared Error before the optimization ($it = 0$) in *Ane-2D*

field. Accordingly, to the previous example, the control **c** acts predominantly on the regions where the CFD (solution at $it = 0$) and the reference solution are highly different in the velocity field.

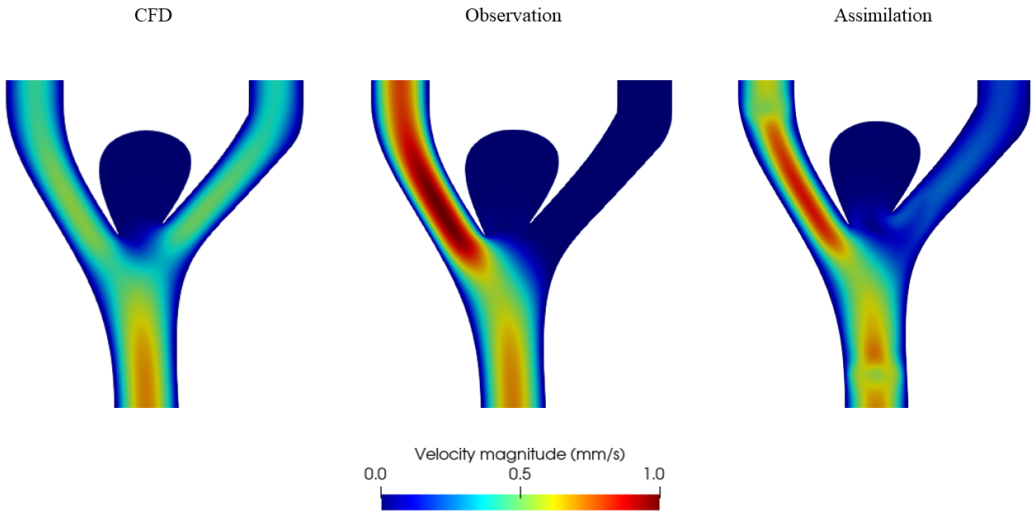

Figure 3.15: Comparison of the velocity magnitude contour maps among CFD (solution at *it=0*), observation and assimilated solution at optima point (*it=63*) for $alpha = 10^{-4}$.

3.2.3 3DVar for blood flow reconstruction from 4D flow in IA.

The 3DVar implementation was applied on a restriction of the vascular model (comprising the IA) used to carry out the transient simulations in SimVascular, in order to reduce the computational cost. The model was discretised with a 700 thousands element mesh. The DA procedure focused only on the highest flow rate time instant.

The physical measurements were obtained from the same 4D flow data used to extract BCs for the transient simulations (CFD, Uniform-FSI and NonUniform-FSI). Velocities at the highest flow rate time frame (10^{th} time frame of the 4D flow) were extracted from 4D flow data and interpolated onto the computational mesh. Differently from the 2D experiments, the DA was performed over the entire domain.As mentioned in Chapter 2, the 3DVar here implemented is based on a gradient descent optimization algorithm implemented ad-hoc. Even with only two optimisation iterations, a sufficient functional minimisation was reached. In Fig. 3.16, the results of the DA at each optimization iteration are shown. The DA quality improves with the iterations. The optimisation reduced the initial functional value $(J + R)$ of $1.7 \cdot 10^6$ to $1.2 \cdot 10^6$. At the last iteration ($it = 2$), a good match in the velocity field was obtained between the assimilated solution and the observation, especially in the high-velocity flow region. Nevertheless, a good similarity can also be appreciated within the aneurysm where the inflow jet and the vortex flow are reproduced in the assimilated solution with high fidelity with respect to 4D flow measurements. In the second row, the contour maps of the

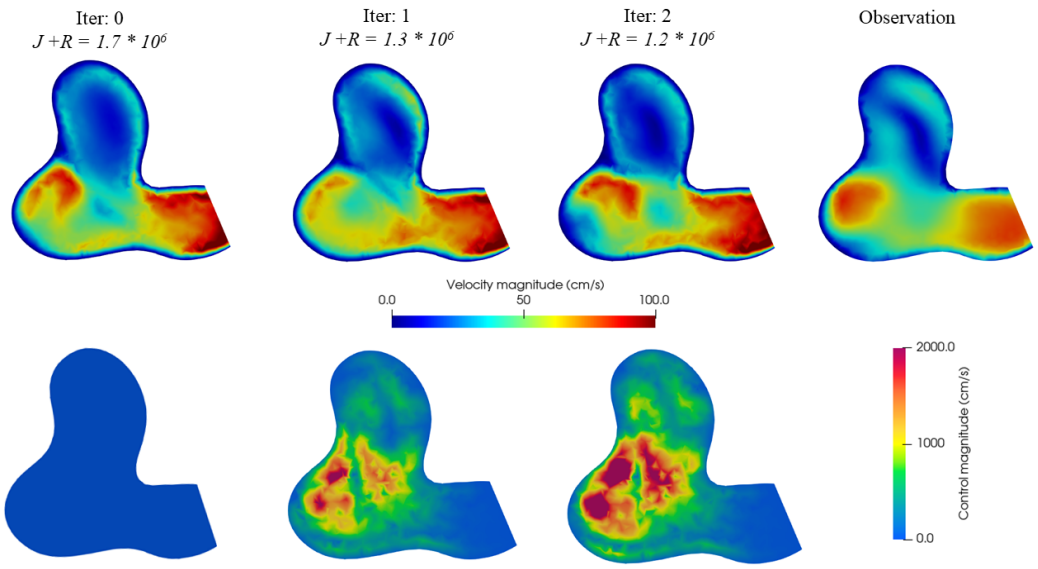

Figure 3.16: Data assimilation quality assessment over the optimization iterations. **First row:** Velocity magnitude contour maps of the assimilated solution at each optimization iteration against the velocity magnitude contour map for the observation. **Second row:** Control magnitude contour maps through the optimisation iterations.

control variable is shown on the same cross-sectional plane for each optimization iteration. As expected, the control variable is high in the region where the discrepancies between the solution and the observation are significant. The control ranges between 0 and 4000cm/s along the plane. Notably, in this case, the control variable ranged over a wider interval than in the 2D numerical experiments concerning the velocities that characterise the domain of interest.

The 3DVar here implemented concerns only the highest flow rate time instant of the cardiac cycle. As mentioned in Chapter 2, although steady BCs were assumed in the problem definition, the finite element solver was implemented as transient to add stability. In this way, the implemented 3DVar allows also improving the time resolution of the 4D flow. This idea is represented in Fig. 3.17. The figure pictures the last optimization iteration of 3DVar, where the assimilated velocity is basically computed for 10 time iterations (Navier-Stokes iterations) between the 9^{th} and 10^{th} time frame of the 4D flow. The 9^{th} time frame was used to initialise the velocity field. In this way, the Navier-Stokes solution at each temporal iteration would represent a prediction of the blood flow at a fraction t of the 4D flow temporal resolution τ. At $t = \tau$ the Navier-Stokes solution is the blood flow reconstruction from the 10^{th} time frame of the 4D flow.

The quality of the 3DVar solution was evaluated against the 4D flow based-CFD carried in

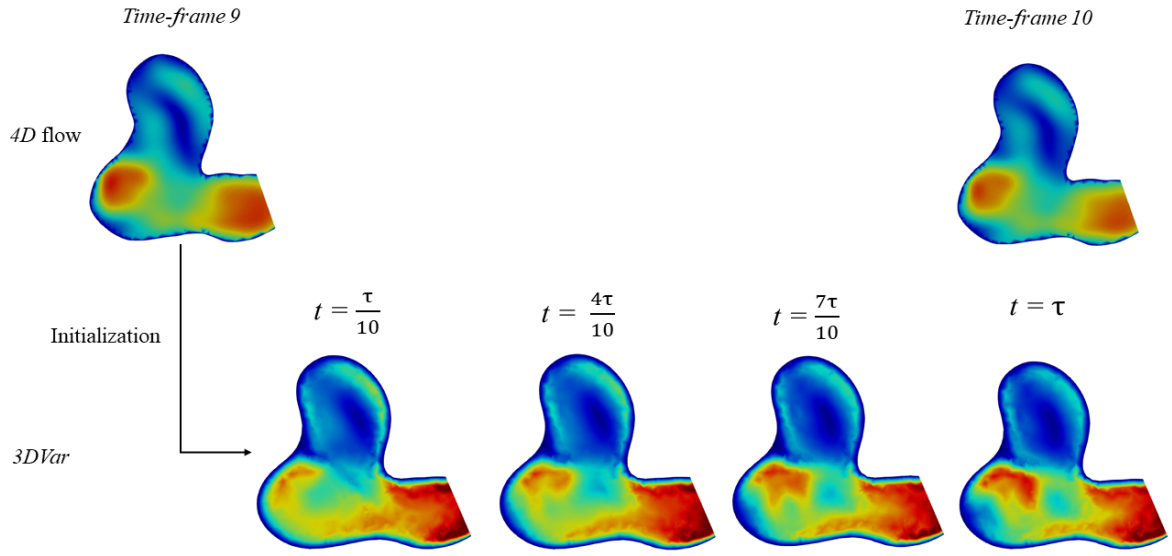

Figure 3.17: 4D flow temporal resolution improvement due to the 3DVar. τ is the 4D flow temporal resolution. The 3DVar is performed by solving a transient Navier-Stokes problem for $N = 10$ temporal iterations. In this way the assimilated solution is computed at $t = \frac{n\tau}{N}$ with $n = 1, ..., 10$.

SimVascular. The CFD simulation was carried out on the complete geometry with a finer mesh and assuming reliable outlet boundary conditions (3-WK elements were used) with respect to the 3DVar numerical model. In Fig. 3.18, a qualitative comparison of velocity field obtained with 4D flow, high-resolution CFD and 3DVar is reported at the highest flow rate time frame. As expected, the velocity contour maps (top row) for the high-resolution CFD looks smoother and well-defined. A good agreement can be appreciated between 3DVar and High-resolution CFD in both high and low flow rate regions. Colour-encoded velocity streamlines (bottom row) show vortex formation within the aneurysm region in 3DVar and High-resolution CFD following 4D flow. Notably, in 3DVar, the vortex shape is more consistent with the 4D flow since the vortex is narrower than High-resolution CFD. Overall, the 3DVar looks like a good compromise between 4D flow and High-resolution CFD in terms of resolution and agreement with the measurements. The RMSE of the velocity magnitude with respect to the 4D flow measurements reported in the Table 3.10, confirms the accuracy improvement of 3DVar with respect to the High-resolution CFD. In Fig. 3.19 a scatter plot shows the improvement of RMSE over the optimization iterations for the 3DVar. At the last optimisation iteration the RMSE for 3DVar is $\sim 5\%$ lower than RMSE for High-resolution CFD.

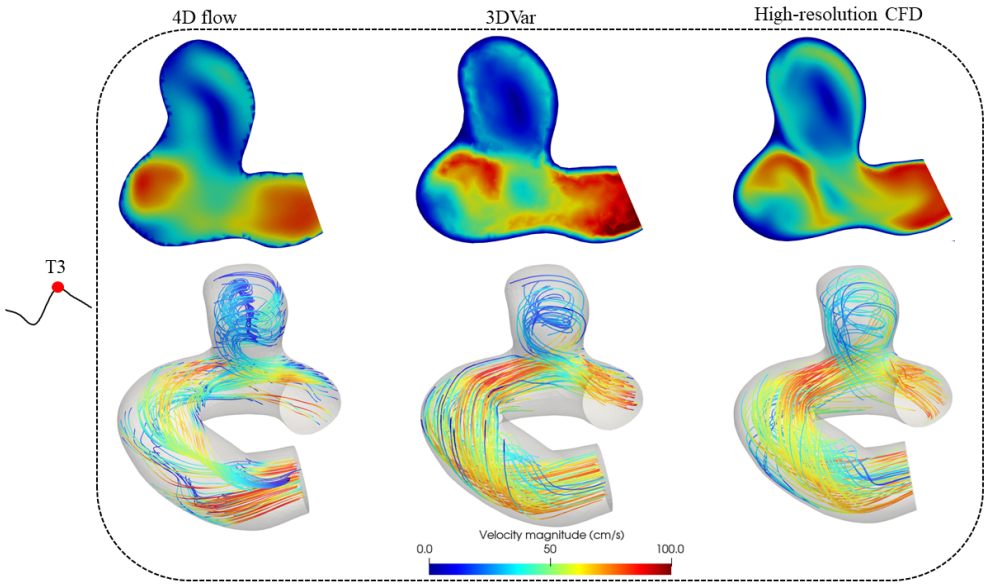

Figure 3.18: Qualitative comparison among 4D flow, 3DVar and High-resolution CFD at the highest flow rate time frame. **Top row:** Velocity contour map extracted from a cross-sectional plane of the aneurysm. **Bottom row:** Colour-encoded velocity streamlines over all the domain.

	3DVar	High-resolution CFD
RMSE [cm/s]	16.86	17.70

Table 3.10: RMSE of the velocity magnitude for 3DVar and High-resolution CFD against the observation (4D flow).

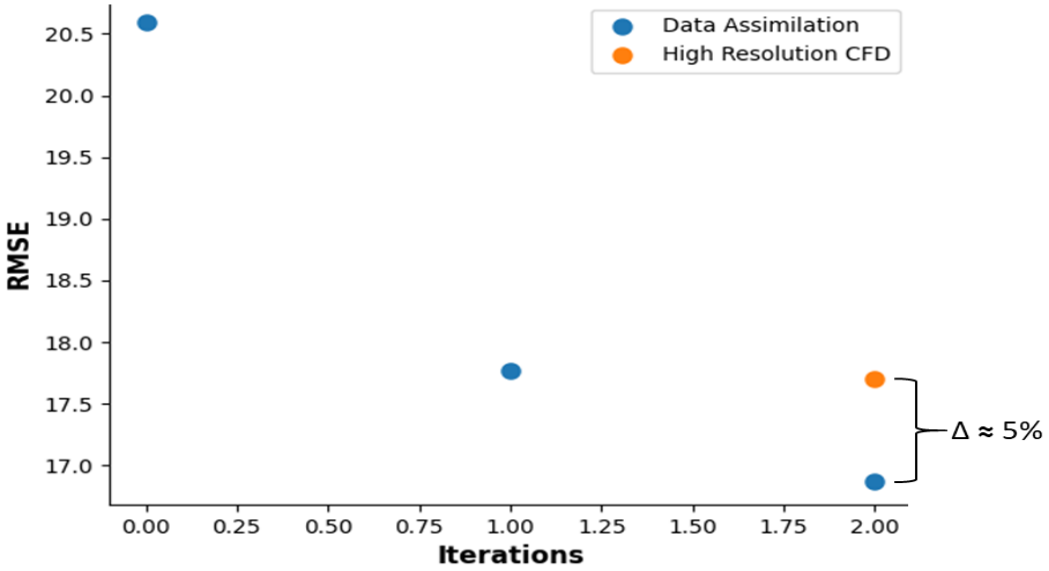

Figure 3.19: Scatter plot of RMSE of the velocity magnitude [cm/s] between 4D flow and 3DVar over the optimisation iterations. Comparison at the optimal point ($it = 2$) with the RMSE for High-resolution CFD.

3.2.4 WSS estimation with 3DVar

As illustrative example of 3DVar application in hemodynamics assessment for IAs, WSS were extracted from the assimilated solution and compared against SimVascular. A steady-state CFD simulation were carried out in SimVascular on the same mesh and applying the same BCs of the CFD simulation implemented in 3DVar (velocity profile extracted from 4D flow at peak flow in inlet, and zero pressure in outlet). WSS were computed by a custom filter in Paraview. In order to validate the WSS computation, the result from the built-in SimVascular function for WSS estimation were considered in the comparison, as shown in Fig. 3.20. The difference between the WSS magnitude from SimVascular (SV-WSS) and the custom paraview filter (P-WSS) are negligible, given a 95^{th} percentile of WSS discrepancy lower than $\sim$ 10%. By comparing P-WSS estimation, the 3DVar overestimates the WSS magnitude concerning the CFD simulation carried in SimVascular. As shown in Table 3.20 the overestimation is about 50% for the maximum WSS and 37% for the 95^{th} percentile. Nevertheless, it has to be noted that the 3DVar is affected by blood flow spatial and temporal information (4D flow measurements) acquired over a larger domain, which are not considered by the CFD simulation carried in SimVascular. As a metter of fact, the 3DVar WSS distribution look more similar to the WSS computed by the 4D flow based-CFD simulation at peak flow, reported in Fig. 3.9.

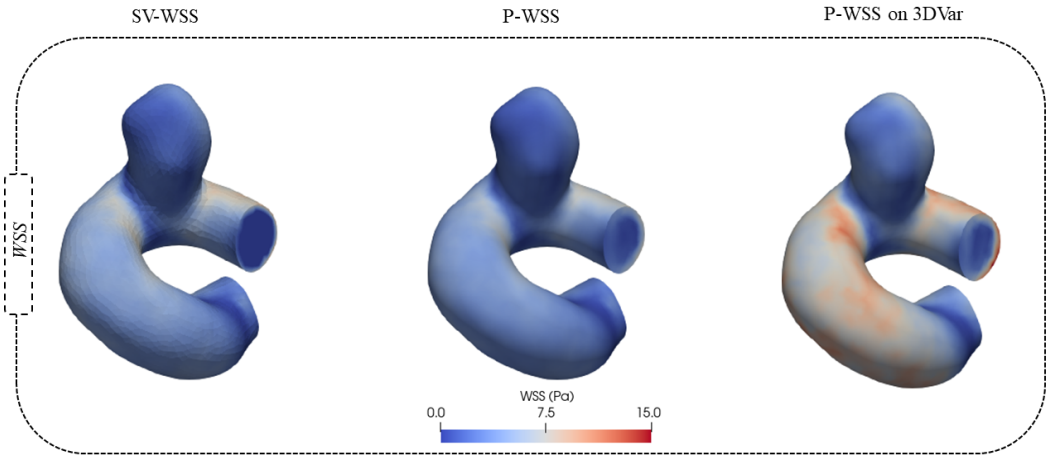

Figure 3.20: WSS contour maps computed by the Simvascular built-in fucuntion (SW-WSS) and paraview custom filter (P-WSS) for the CFD simulation carried in SimVascular anf the 3DVar.

	CFD	3D-Var
Maximum WSS [Pa]	8.39	17.09 (+50%)
95^{th} percentile WWS [Pa]	6.04	9.63 (+37%)

Table 3.11: Maximum and 95^{th} percentile of WSS magnitude computed by Paraview custom filter in CFD and 3D-Var with the percentage overestimation reported in brackets.

Chapter 4

Discussion and conclusions

IA risk stratification is crucial for aneurysm rupture prediction. Intra-aneurysmal hemodynamic assessment provides quantitative information about blood flow and its interaction with blood vessels. Blood flow assessment can be performed by numerical simulations, or by imaging techniques. Numerical models enable simulating blood flow within cardiac districts. Instead, 4D flow MRI is a non-invasive imaging technique that enables measurements of blood flow. However, both approaches still have limitations: numerical models depend on the hypothesis needed for the model, while 4D flow has a low spatiotemporal resolution and image quality is affected by noise.

Numerical models allow analyzing intra-aneurysmal hemodynamics in rigid domains with CFD or deformable domains with FSI analysis. However, the reliability of blood flow predictions in numerical models highly depends on the patient-specific geometry reconstruction, blood constitutive model and the inlet and outlet BCs. Reliable BCs are often represented by measurements of velocity and pressure. Currently, 4D flow is commonly used for the extraction of velocity information to set as BCs, given its low invasiveness and acceptable reliability. On the contrary, reliable pressure measurements are invasive and scarcely available, especially in some cardiac districts, such as cerebral arteries. To overcome the limitations of numerical models, and increase the accuracy of the blood flow predictions, a possible solution is to combine blood flow simulations with 4D flow measurements, employing DA. In this manner, DA would improve numerical simulations by including data-related effects and features otherwise complicated to model.

In this work, a heuristic Var DA approach was implemented and evaluated in reconstructing blood flow in an IA model from 4D flow measurements. Together 4D flow guided-CFD and FSI simulations were carried out on the same model. The main objective of this work was to

investigate whether DA in blood flow simulations can improve the accuracy of haemodynamic assessment by fully exploiting 4D flow measurements.

4.1 4D flow guided-CFD and FSI simulations

4.1.1 Validation against 4D flow measurements

CFD and FSI simulations proved to be a reliable method for reconstructing blood flow by a qualitative and quantitative comparison with 4D flow data. The time-averaged outflow rate was consistent with the 4D flow in both CFD and NonUniform-FSI, with a maximum difference of ~ 0.42L/min at the Outlet Small however justifiable by the numerical assumptions made for the simulations. The good agreement between the numerical results and 4D flow was further confirmed by the velocity colour maps extracted along planes across the aneurysm model. In accordance to [19], a good qualitative agreement was found in flow features within the aneurysm at peak flow, while at the lowest flow rate time frame 4D flow measurements appeared inconsistent due to the low velocity-to-noise ratios. Both CFD and NonUniform-FSI predicted the vortex formation inside the aneurysm where the velocity is generally low. The relative difference in velocity magnitude with the 4D flow, evaluated by the normalized RMSE, was variable among the planes and time points but overall remains relatively small in both numerical simulations. Notably, both CFD and NonUniform-FSI agreed with 4D flow measurements with a maximum accuracy of $\sim 85\%$ in velocity magnitude over all the cardiac cycle, higher than the maximum accuracy rate reported in [19] and [20] ($\sim 70\%$ and $\sim 75\%$, respectively). Nevertheless, it has to be noted the 4D flow employed in this work was postproccessed and de-noised following the correction strategies reported in [37] which enabled reliable measurements even in the small regions, such as the intracranial aneurysm, and only minimally affected by noise.

4.1.2 Impact of wall deformability on intracranial aneurysm hemodynamics

Analyzing outlet flow rates and velocity colour maps also allowed to highlight the impact of wall deformability on blood flow prediction. Moreover, the aneurysm wall thinning, accounted for in NonUniform-FSI, should improve the reliability of the blood flow evaluation inside the aneurysm. However, NonUniform-FSI does not seem to bring any further improvement in velocity field prediction. The outflow rate difference is minimal and

velocity magnitude distributions obtained with CFD and NonUniform-FSI showed only a minimal mismatch. The maximum difference of 5 cm/s for the velocity magnitude in a small region of the aneurysm is imperceptible given the wide velocity range which characterizes this anatomical districts.

On the other hand, the damping of blood flow due to wall deformability caused a decrease in the maximum pressure difference at the aneurysm surface and in the peak-to-peak pressure difference upstream and downstream the aneurysm. However, these discrepancies (6% for the maximum pressure difference and 1.4% for the peak-to-peak pressure difference) are relatively small. Unexpectedly, the aneurysm wall thinning hypothesis did not have a significant impact on the pressure distribution comparing Uniform- and NonUniform-FSI.

Nevertheless, the vessel wall displacement fields obtained in Uniform- and NonUniform-FSI were found significant and consistent with previous works. In [16], FSI analysis was carried out on an aneurysm model with linear elastic behaviour and the same wall thickness assumed herein. The maximum displacement magnitude at peak flow (0.035cm) reported in [16] is comparable with that one obtained in Uniform-FSI (0.042cm). As expected, in NonUniform-FSI, the displacement magnitude on the aneurysm wall doubled with respect to Uniform-FSI due to the aneurysm wall thinning assumption. The same result was obtained in [17] where a similar comparison was carried out assuming the same wall thinning as here. Anyway, in [17] the displacement field was $\sim 30\%$ lower concerning both Uniform and NonUniform-FSI. This discrepancy is probably due to the hyperelastic behaviour accounted for in modeling the aneurysm wall in [17]. Indeed, as stated in [16], with equal thickness, hyperelasticity led to lower aneurysm wall displacements concerning the linear elastic model. Contrastingly, in [16] a different velocity profile and distribution was obtained within the aneurysm comparing CFD and FSI results. This disagreement may be related to the different adopted FSI formulations. The CMM-FSI implemented in SimVascular solves the geometry problem related to the vessel motion differently from the Arbitrary Lagrangian-Eulerian (ALE) formulation adopted in [16]. In the CMM formulation the vessel wall is assumed as a thin membrane strongly coupled to the fluid boundary. This provides a lower computational cost with respect to ALE formulation but may lead to some inaccuracy in the velocity field prediction. However, to properly evaluate the hemodynamics differences introduces by the CMM-FSI with respect to ALE, a thorough sensitivity analysis should be performed, which was not among the aims of the study.

Another explanation for the low impact of the wall deformability on the blood flow prediction

inside the aneurysm could be related to the size and shape of the latter. This hypothesis is supported by the results obtained in [15]. In this work, FSI analysis with ALE formulation and CFD analysis were performed on four IA models with different sizes and shapes. Similar flow speed distribution was obtained at peak flow for the side-wall aneurysms in CFD and FSI analysis. This second hypothesis should be confirmed by analysing the hemodynamics in various types of IAs employing the CMM-FSI.

Overall, the CMM formulation may be valuable in predicting the impact of vessel wall deformability on the pressure distribution and in evaluating the displacements of the aneurysm wall during the cardiac cycle.

4.1.3 Intracranial aneurysm hemodynamics: WSS and OSI

Uniform- and NonUniform-FSI simulation results were excluded for the IA hemodynamics evaluation, given the low influence of wall deformability assumption on the predicted velocity field within the aneurysm. WSS and OSI are believed to play an important role in intracranial aneurysms initiation, growth and rupture [42]. WSS was found varying over the cardiac cycle. As expected, the bifurcation between the ICA and the ACA-MCA junction was a region affected by higher WSS. The bifurcation and the rapid variation of vessel diameters may lead to secondary flows which increase the shear stress on the vessel wall. The side-wall of the aneurysm protrudes upstream toward the aforementioned bifurcation on a region affected by high TAWSS which range between 15 to 25Pa. The WSS distribution along the aneurysm wall was found qualitatively and quantitatively consistent with [38], where Jou et al. analysed the WSS on twenty-six saccular IA models at the paraclinoid and superclinoid segments of ICA. The mean of the highest WSS found was $\sim 6\%$ lower than the maximum WSS found here. Similar WSS distribution was also found in [39] and [40], where Cerebral et al. analysed hemodynamics in 210 IAs through CFD. Assuming pulsatile flow condition the mean of the highest WSS found was equal to 27.7Pa in perfect accordance with the highest WSS found here.

On the aneurysm surface, WSS was found overall low concerning the proximal parent vessel for each considered time point. Only at the highest flow rate time instant, an increased WSS was visible on the left-posterior side of the aneurysm. This is the flow impingement region which accordingly to [82] is normally associated to increased WSS values and believed as the area where wall thinning begins during IA development. The wide variability in WSS distribution between the aneurysm sac and the proximal vessel was in accordance with the hypothesis

proposed by Meng et al. in [41], who associated high WSS to the initiation and growth of the aneurysm, whereas low WSS to the rupture. Accordingly, the high WSS acting on the segment upstream of the bifurcation may have initiated the aneurysm formation, ballooning the vessel. Then, the drastic reduction of blood flowing inside the vessel inflation caused a decrease of WSS. Unexpectedly the OSI values were found overall low along all the model. Only small regions were affected by OSI closed to 0.5 but distant from the aneurysm sac. The expected low WSS-high OSI relation, as reported in [41], was not found here.

4.2 2D and 3D variational DA

The novelty of the Var DA approach implemented here lies in its formulation. In several previous works [28, 29, 30], Var DA aimed at recovering the optimal inlet or outlet boundary conditions from the measurements. Contrastingly, in this work the data assimilation was carried out controlling a fictitious source term added to the Navier-Stokes formulation, which acted as a control parameter for the DA. The fictitious source term hence forced blood flow dynamics to follow a reference solution.

In the 2D numerical experiments Var DA was performed on a restriction of the domain to reduce the computational cost of the optimization procedure and verify the robustness of the algorithm by varying the size of the reference solution. For both *Hole* and *2D-Ane* the DA quality, measured by the misfit with the observation worsened for regularisation parameter $\alpha > 10^{-2}$. In accordance to [30], the regularisation term promotes smoothness on the control functions. For low α values, the effect of the control function was amplified, the optimisation converged in more iterations and significantly reduced the cost functional. Nevertheless, the accuracy of the reconstruction, measured by the RMSE of the velocity magnitude between the assimilated solution and the observations, worsened for $\alpha = 10^{-4}$, even if the minimisation of the functional was significant. This result was confirmed by the velocity magnitude colour maps where the the flow reconstruction introduced numerical artifacts in the velocity field, especially in *2D-Ane*. The location of the artifacts at the boundaries of χ suggests the risk of overfitting the observation when the Var DA is carried out on a restriction of the flow domain.

Another fascinating aspect highlighted by the 2D numerical experiments was the control distribution on the fluid domain. As expected, the control variable peaked in the regions where the CFD and the reference solution differed at the most. This finding confirms the role

of the control variable as an external source which weakly constrains the flow field to follow a reference solution.

3DVar was implemented for steady-state blood flow simulations and performed over the entire flow domain to reconstruct blood flow from 4D flow measurements. As suggested in [29], a better option would have been excluding the near-wall regions since they are usually more affected by error due to partial volume effects. Nevertheless, the 4D flow acquisition employed here was highly de-noised and the velocity was interpolated to zero at the wall following the correction strategies reported in [37]. In 3DVar, the optimisation algorithm implemented in the `dolphin-adjoint` library failed due to the drastically increased dimensionality compared to the 2D experiments. The optimisation algorithm was the same used by Funke et al. [30] in the 4DVar implemented for transient blood flow. However, the optimal control applied in this 3DVar formulation was dimensionally larger and, therefore, computationally more expensive in the optimisation procedure. Nevertheless, the ad-hoc gradient descent optimisation algorithm provided a sufficient functional minimisation even in only two optimisation iterations. This algorithm relies on a commonly used approach for finding a local minimum of a differentiable function. Contrastingly to the *adjoint* approach, here, the Navier-Stokes equations are solved at each iteration therefore greatly increasing the computational time. The main limitation of this implementation lies in the control variable update routine, since learning rate step lengths had to be adjusted manually for each iteration to guarantee convergence. Nevertheless, the good agreement found between the assimilated solution and the observations confirmed the accuracy of the implemented 3DVar formulation in reconstructing blood flow from 4D flow data. As already stated for the 2D experiments, the control variable acted mostly at the regions where the observation and the CFD solution differed at the most. The wider range of values in which the control variable varied compared to the 2D numerical experiments may be explained by the nature of the observations. Here, the 4D flow measurements were affected by low resolution, a factor which was not accounted in the synthetic reference solution applied in the 2D experiments.

Notably, the reconstructed flow features were found consistent with the observations and more detailed even within the aneurysm where the data is less accurate due to the low velocity-to-noise ratios. The approach enabled noise reduction and super-resolution in 4D flow measurements. Moreover, the peculiar 3DVar formulation implemented here allows also augmenting 4D flow temporal resolution. By designing the optimisation problem with a transient formulation of the Navier-Stokes equations, one can freely choose the number

of the Navier-Stokes iterations to arbitrarily augment the temporal resolution between two consecutive 4D flow time frames.

Additionally, the 3DVar here was limited only at the highest flow rate time frame. However, by extending the approach over all the 4D flow data-set, it could be possible to reconstruct blood flow dynamics for all the cardiac cycle.

4.3 3DVar and High-resolution CFD in recostructing IAs blood flow from 4D flow data

3DVar allowed obtaining a better agreement with 4D flow data than High-resolution CFD (4D flow based-CFD) within the region of interest even on a coarser mesh (700K vs 1.3M elements), quantified by a lower RMSE of the velocity magnitude (16.86 cm/s and 17.70 cm/s for 3DVar and High-resolution CFD, respectively). 4D flow-based numerical simulations are considered the gold standard for hemodynamics assessment due to the patient-specificity of the BCs. Nevertheless, 3DVar allowed for more consistent flow features and velocity magnitude prediction with 4D flow compared to High-resolution CFD. Therefore, 3DVar proved to be a valid method to increase numerical models accuracy in hemodynamic assessment in IA, exploiting entirely the 4D flow measurements. This makes 3DVar advantageous for blood flow prediction in those cardiac districts where reliable physical measurements to apply as BCs are scarcely available, such as cerebral arteries.

The illustrative example of WSS computation over the aneurysm surface showed a possible implication of the quality improvement in hemodynamics assessment brought by 3DVar. WSS were significantly overestimated with respect to a CFD simulation carried out on the same mesh and applying the same BCs of 3DVar. However, it is to be noted that in 3DVar the velocity field is affected by 4D flow measurements acquired over a larger domain, including the bifurcation downstream the aneurysm. The bifurcation inevitably affects the hemodynamics around the aneurysm. As a matter of fact, the WSS distribution obtained with 3DVar was similar with the 4D flow guided-CFD estimation at the peak flow, although in the latter case the WSS magnitude was larger. Nevertheless, the discrepancy in WSS may be justified by the different and more accurate velocity field accounted for in 3DVar. In order to confirm this statement, 3DVar and 4D flow guided-CFD should be performed over the same mesh for a mesh-indipendent WSS computation. Indeed, as known, mesh quality has a high impact on the WSS computation.

4.4 Conclusion

In conclusion, this work investigated the role of 4D flow based-CFD and FSI in assessing IA hemodynamics and proposed a heuristic 3D variational data assimilation approach to reconstruct the flow conditions in a real IA from 4D flow data.

CFD analysis is a well-established method to study the IA hemodynamics with a good level of reliability and enriches the aneurysm risk stratification by combining hemodynamics parameters with clinical data. FSI simulations allow to account for vessel-blood interaction enriching the analysis with quantitative information about the displacement of the vessel wall. Notably, in this thesis work, an ad-hoc python code was implemented to define variable vessel wall properties enabling the FSI implemented in SimVascular to account for pathological variation of the vessel wall stiffness or thickness. This allowed for investigating the effect of pathological wall thinning on blood flow within the aneurysm.

3DVar proved to be a valuable approach to fully exploit the available measurements, guaranteeing a better accuracy in blood flow prediction than 4D flow based-CFD analysis. This method is attractive in hemodynamics assessment of those vascular regions where models parameters, such as pressure estimations or vessel wall properties, are scarcely available, being dependent only on 4D flow acquisitions. Further investigations should be done to assess 3DVar efficacy in improving the accuracy of hemodynamics-related parameters estimation.

To the best of the author's knowledge, this is the first 3DVar formulation of this kind. It represents an effort toward an efficient merging of numerical modelling and 4D flow measurements, which will ultimately lead to more accurate risk stratification for vascular diseases such as IAs.

Bibliography

[1] Orlando Diaz and Leonardo Rangel-Castilla. Endovascular treatment of intracranial aneurysms. *Handbook of clinical neurology*, 136:1303–1309, 2016.

[2] Thorsten Steiner, Seppo Juvela, Andreas Unterberg, Carla Jung, Michael Forsting, and Gabriel Rinkel. European stroke organization guidelines for the management of intracranial aneurysms and subarachnoid haemorrhage. *Cerebrovascular Diseases*, 35(2):93–112, 2013.

[3] B. Gregory Thompson, Robert D. Brown, Sepideh Amin-Hanjani, Joseph P. Broderick, Kevin M. Cockroft, E. Sander Connolly, Gary R. Duckwiler, Catherine C. Harris, Virginia J. Howard, S. Claiborne (Clay) Johnston, Philip M. Meyers, Andrew Molyneux, Christopher S. Ogilvy, Andrew J. Ringer, and James Torner. Guidelines for the management of patients with unruptured intracranial aneurysms. *Stroke*, 46(8):2368–2400, 2015.

[4] Zhihui Duan, Yuanhui Li, Sheng Guan, Congmin Ma, Yuezhen Han, Xiangyang Ren, Liping Wei, Wenbo Li, Jiyu Lou, and Zhiyuan Yang. Morphological parameters and anatomical locations associated with rupture status of small intracranial aneurysms. *Scientific Reports (Nature Publisher Group)*, 8:1–7, 04 2018. Copyright - Copyright Nature Publishing Group Apr 2018; Ultimo aggiornamento - 2018-04-25.

[5] Michael Markl, Alex Frydrychowicz, Sebastian Kozerke, Mike Hope, and Oliver Wieben. 4d flow mri. *Journal of Magnetic Resonance Imaging*, 36(5):1015–1036, 2012.

[6] Susanne Schnell, Sameer A. Ansari, Parmede Vakil, Marie Wasielewski, Maria L. Carr, Michael C. Hurley, Bernard R. Bendok, Hunt Batjer, Timothy J. Carroll, James Carr, and Michael Markl. Three-dimensional hemodynamics in intracranial aneurysms: influence of size and morphology. *Journal of Magnetic Resonance Imaging*, 39(1):120–131, 2014.

[7] P. van Ooij, J. J. M. Zwanenburg, F. Visser, C. B. Majoie, E. vanBavel, J. Hendrikse, and A. J. Nederveen. Quantification and visualization of flow in the circle of willis: Time-resolved three-dimensional phase contrast mri at 7 t compared with 3 t. *Magnetic Resonance in Medicine*, 69(3):868–876, 2013.

[8] S.A. Ansari, S. Schnell, T. Carroll, P. Vakil, M.C. Hurley, C. Wu, J. Carr, B.R. Bendok, H. Batjer, and M. Markl. Intracranial 4d flow mri: Toward individualized assessment of arteriovenous malformation hemodynamics and treatment-induced changes. *American Journal of Neuroradiology*, 34(10):1922–1928, 2013.

[9] J.R. Cebral, F. Mut, J. Weir, and C.M. Putman. Association of hemodynamic characteristics and cerebral aneurysm rupture. *American Journal of Neuroradiology*, 32(2):264–270, 2011.

[10] Hamidreza Gharahi, Byron A Zambrano, David C Zhu, J Kevin DeMarco, and Seungik Baek. Computational fluid dynamic simulation of human carotid artery bifurcation based on anatomy and volumetric blood flow rate measured with magnetic resonance imaging. *International journal of advances in engineering sciences and applied mathematics*, 8(1):40—60, March 2016.

[11] Zijing Zeng, Michael J Durka, David F Kallmes, Yonghong Ding, and Anne M Robertson. Can aspect ratio be used to categorize intra-aneurysmal hemodynamics?–a study of elastase induced aneurysms in rabbit. *Journal of biomechanics*, 44(16):2809—2816, November 2011.

[12] G. Lu, L. Huang, X.L. Zhang, S.Z. Wang, Y. Hong, Z. Hu, and D.Y. Geng. Influence of hemodynamic factors on rupture of intracranial aneurysms: Patient-specific 3d mirror aneurysms model computational fluid dynamics simulation. *American Journal of Neuroradiology*, 32(7):1255–1261, 2011.

[13] Juan R. Cebral, Marcelo A. Castro, James E. Burgess, Richard S. Pergolizzi, Michael J. Sheridan, and Christopher M. Putman. Characterization of cerebral aneurysms for assessing risk of rupture by using patient-specific computational hemodynamics models. *American Journal of Neuroradiology*, 26(10):2550–2559, 2005.

[14] J.R. Cebral, F. Mut, J. Weir, and C.M. Putman. Association of hemodynamic characteristics and cerebral aneurysm rupture. *American Journal of Neuroradiology*, 32(2):264–270, 2011.

[15] Y. Bazilevs, M. C. Hsu, Y. Zhang, W. Wang, X. Liang, T. Kvamsdal, R. Brekken, and J. G. Isaksen. A fully-coupled fluid-structure interaction simulation of cerebral aneurysms. *Computational Mechanics*, 46:16, June 2010.

[16] Ryo Torii, Marie Oshima, Toshio Kobayashi, Kiyoshi Takagi, and Tayfun E. Tezduyar. Fluid-structure interaction modeling of a patient-specific cerebral aneurysm: Influence of structural modeling. *Computational Mechanics*, 43(1):151–159, December 2008.

[17] Ryo Torii, Marie Oshima, Toshio Kobayashi, Kiyoshi Takagi, and Tayfun E. Tezduyar. Influence of wall thickness on fluid–structure interaction computations of cerebral aneurysms. *International Journal for Numerical Methods in Biomedical Engineering*, 26(3-4):336–347, 2010.

[18] S Voß, S Glaßer, T Hoffmann, O Beuing, S Weigand, K Jachau, B Preim, D Thévenin, G Janiga, and P Berg. Fluid-structure simulations of a ruptured intracranial aneurysm: Constant versus patient-specific wall thickness. *Computational and mathematical methods in medicine*, 2016:9854539, 2016.

[19] P. van Ooij, J.J. Schneiders, H.A. Marquering, C.B. Majoie, E. van Bavel, and A.J. Nederveen. 3d cine phase-contrast mri at 3t in intracranial aneurysms compared with patient-specific computational fluid dynamics. *American Journal of Neuroradiology*, 34(9):1785–1791, 2013.

[20] Philipp Berg, Daniel Stucht, Gábor Janiga, Oliver Beuing, Oliver Speck, and Dominique Thévenin. Cerebral blood flow in a healthy circle of willis and two intracranial aneurysms: computational fluid dynamics versus four-dimensional phase-contrast magnetic resonance imaging. *Journal of biomechanical engineering*, 136(4), April 2014.

[21] Jeremy Szajer and Kevin Ho-Shon. A comparison of 4d flow mri-derived wall shear stress with computational fluid dynamics methods for intracranial aneurysms and carotid bifurcations — a review. *Magnetic Resonance Imaging*, 48:62–69, 2018.

[22] Uwe Köhler, Ian Marshall, Malcolm B. Robertson, Quan Long, X. Yun Xu, and Peter R. Hoskins. Mri measurement of wall shear stress vectors in bifurcation models and comparison with cfd predictions. *Journal of Magnetic Resonance Imaging*, 14(5):563–573, 2001.

[23] JONAS LANTZ, JOHAN RENNER, and MATTS KARLSSON. Wall shear stress in a subject specific human aorta — influence of fluid-structure interaction. *International Journal of Applied Mechanics*, 03(04):759–778, 2011.

[24] Jacques Blum, François-Xavier Le Dimet, and I. Michael Navon. Data assimilation for geophysical fluids. In Roger M. Temam and Joseph J. Tribbia, editors, *Special Volume: Computational Methods for the Atmosphere and the Oceans*, volume 14 of *Handbook of Numerical Analysis*, pages 385 – 441. Elsevier, 2009.

[25] Marta D'Elia and Alessandro Veneziani. Methods for assimilating blood velocity measures in hemodynamics simulations: Preliminary results. *Procedia Computer Science*, 1(1):1231–1239, 2010.

[26] M D'Elia, A Veneziani, JCF Pereira, and A Sequeira. A data assimilation technique for including noisy measurements of the velocity field into navier-stokes simulations. In *Proceedings of V European Conference on Computational Fluid Dynamics, ECCOMAS*, volume 18, page 43, 2010.

[27] Marta D'Elia, Mauro Perego, and Alessandro Veneziani. A variational data assimilation procedure for the incompressible navier-stokes equations in hemodynamics. *Journal of Scientific Computing*, 52(2):340–359, 2012.

[28] Jorge Tiago, Telma Guerra, and Adélia Sequeira. A velocity tracking approach for the data assimilation problem in blood flow simulations. *International journal for numerical methods in biomedical engineering*, 33(10):e2856, 2017.

[29] Taha S Koltukluoğlu and Pablo J Blanco. Boundary control in computational haemodynamics. *Journal of Fluid Mechanics*, 847:329–364, 2018.

[30] Simon Wolfgang Funke, Magne Nordaas, Øyvind Evju, Martin Sandve Alnæs, and Kent Andre Mardal. Variational data assimilation for transient blood flow simulations: Cerebral aneurysms as an illustrative example. *International journal for numerical methods in biomedical engineering*, 35(1):e3152, 2019.

[31] Editorial policy statement on numerical accuracy and experimental uncertainty. *Journal of Guidance, Control, and Dynamics*, 19(1):7–7, 1996.

[32] Amirhossein Arzani. Accounting for residence-time in blood rheology models: do we really need non-newtonian blood flow modelling in large arteries? *Journal of The Royal Society Interface*, 15(146):20180486, 2018.

[33] C Alberto Figueroa, Irene E Vignon-Clementel, Kenneth E Jansen, Thomas JR Hughes, and Charles A Taylor. A coupled momentum method for modeling blood flow in three-dimensional deformable arteries. *Computer methods in applied mechanics and engineering*, 195(41-43):5685–5706, 2006.

[34] S Pirola, Z Cheng, OA Jarral, DP O'Regan, JR Pepper, T Athanasiou, and XY Xu. On the choice of outlet boundary conditions for patient-specific analysis of aortic flow using computational fluid dynamics. *Journal of biomechanics*, 60:15–21, 2017.

[35] Anders Logg, Kent-Andre Mardal, and Garth Wells. *Automated solution of differential equations by the finite element method: The FEniCS book*, volume 84. Springer Science & Business Media, 2012.

[36] Patrick E Farrell, David A Ham, Simon W Funke, and Marie E Rognes. Automated derivation of the adjoint of high-level transient finite element programs. *SIAM Journal on Scientific Computing*, 35(4):C369–C393, 2013.

[37] Vitor Mendes Pereira, Olivier Brina, Benedicte M A Delattre, Rafik Ouared, Pierre Bouillot, Gorislav Erceg, Karl Schaller, Karl-Olof Lovblad, and Maria-Isabel Vargas. Assessment of intra-aneurysmal flow modification after flow diverter stent placement with four-dimensional flow mri: a feasibility study. *Journal of NeuroInterventional Surgery*, 7(12):913–919, 2015.

[38] C Alberto Figueroa et al. *A coupled-momentum method to model blood flow and vessel deformation in human arteries: applications in disease research and simulation-based medical planning*. PhD thesis, Stanford university Stanford, CA, 2006.

[39] J.R. Cebral, F. Mut, J. Weir, and C. Putman. Quantitative characterization of the hemodynamic environment in ruptured and unruptured brain aneurysms. *American Journal of Neuroradiology*, 32(1):145–151, 2011.

[40] Juan R Cebral, Mariano Vazquez, Daniel M Sforza, Guillaume Houzeaux, Satoshi Tateshima, Esteban Scrivano, Carlos Bleise, Pedro Lylyk, and Christopher M Putman.

Analysis of hemodynamics and wall mechanics at sites of cerebral aneurysm rupture. *Journal of NeuroInterventional Surgery*, 7(7):530–536, 2015.

[41] H. Meng, V.M. Tutino, J. Xiang, and A. Siddiqui. High wss or low wss? complex interactions of hemodynamics with intracranial aneurysm initiation, growth, and rupture: Toward a unifying hypothesis. *American Journal of Neuroradiology*, 35(7):1254–1262, 2014.

[42] Anil Can and Rose Du. Association of Hemodynamic Factors With Intracranial Aneurysm Formation and Rupture: Systematic Review and Meta-analysis. *Neurosurgery*, 78(4):510–520, 10 2015.

[43] Zhihui Duan, Yuanhui Li, Sheng Guan, Congmin Ma, Yuezhen Han, Xiangyang Ren, Liping Wei, Wenbo Li, Jiyu Lou, and Zhiyuan Yang. Morphological parameters and anatomical locations associated with rupture status of small intracranial aneurysms. *Scientific reports*, 8(1):6440, April 2018.

[44] Julie Rosner, Vamsi Reddy, and Forshing Lui. *Neuroanatomy, Circle of Willis*. StatPearls Publishing, Treasure Island (FL), 2020.

[45] Amar Krishnaswamy, Joshua P. Klein, and Samir R. Kapadia. Clinical cerebrovascular anatomy. *Catheterization and Cardiovascular Interventions*, 75(4):530–539, 2010.

[46] Gutierrez Jose Menshawi Khaled, Mohr Jay P. A functional perspective on the embryology and anatomy of the cerebral blood supply. *J Stroke*, 17(2):144–158, 2015.

[47] W P Sanders, P A Sorek, and B A Mehta. Fenestration of intracranial arteries with special attention to associated aneurysms and other anomalies. *American Journal of Neuroradiology*, 14(3):675–680, 1993.

[48] Amar Krishnaswamy, Joshua P. Klein, and Samir R. Kapadia. Clinical cerebrovascular anatomy. *Catheterization and Cardiovascular Interventions*, 75(4):530–539, 2010.

[49] Keun-Hwa Jung. New pathophysiological considerations on cerebral aneurysms. *Neurointervention*, 13(2):73, 2018.

[50] Michael B. Pritz. Cerebral aneurysm classification based on angioarchitecture. *Journal of Stroke and Cerebrovascular Diseases*, 20(2):162 – 167, 2011.

[51] Alexander Keedy. An overview of intracranial aneurysms. *McGill journal of medicine : MJM : an international forum for the advancement of medical sciences by students*, 9(2):141—146, July 2006.

[52] Kartik Jain. *Transition to Turbulence in Physiological Flows: Direct Numerical Simulation of Hemodynamics in Intracranial Aneurysms and Cerebrospinal Fluid Hydrodynamics in the Spinal Canal.* PhD thesis, Universitat Siegen, Germany, September 2016.

[53] Hiroshi Ujiie, Yoshinori Tamano, Kuri Sasaki, and Tomokatsu Hori. Is the aspect ratio a reliable index for predicting the rupture of a saccular aneurysm? *Neurosurgery*, 48(3):495–503, 2001.

[54] Rachel Kleinloog, Nikki de Mul, Bon H Verweij, Jan Andries Post, Gabriel J E Rinkel, and Ynte M Ruigrok. Risk Factors for Intracranial Aneurysm Rupture: A Systematic Review. *Neurosurgery*, 82(4):431–440, 05 2017.

[55] S.P. Ferns, C.B.L.M. Majoie, M. Sluzewski, and W.J. van Rooij. Late adverse events in coiled ruptured aneurysms with incomplete occlusion at 6-month angiographic follow-up. *American Journal of Neuroradiology*, 31(3):464–469, 2010.

[56] Andrew J. Ringer, Giuseppe Lanzino, Erol Veznedaroglu, Rafael Rodriguez, Robert A. Mericle, Elad I. Levy, Ricardo A. Hanel, Demetrius K. Lopes, and Alan S. Boulos. DOES ANGIOGRAPHIC SURVEILLANCE POSE A RISK IN THE MANAGEMENT OF COILED INTRACRANIAL ANEURYSMS? A MULTICENTER STUDY OF 2243 PATIENTS. *Neurosurgery*, 63(5):845–849, 11 2008.

[57] J. Pablo Villablanca, Neil Martin, Reza Jahan, Y. Pierre Gobin, John Frazee, Gary Duckwiler, John Bentson, Marcella Hardart, Domingos Coiteiro, James Sayre, and Fernando Vinuela. Volume-rendered helical computerized tomography angiography in the detection and characterization of intracranial aneurysms. *Journal of Neurosurgery*, 93(2):254 – 264, 01 Jan. 2000.

[58] Toshinori Hirai, Yukunori Korogi, Ken Ono, Yuka Murata, Kenji Suginohara, Toshio Omori, Shozaburo Uemura, and Mutsumasa Takahashi. Preoperative evaluation of intracranial aneurysms: Usefulness of intraarterial 3d ct angiography and conventional angiography with a combined unit—initial experience. *Radiology*, 220(2):499–505, 2001. PMID: 11477260.

[59] Ming-Hua Li, Ying-Sheng Cheng, Yong-Dong Li, Chun Fang, Shi-Wen Chen, Wu Wang, Ding-Jun Hu, and Hao-Wen Xu. Large-cohort comparison between three-dimensional time-of-flight magnetic resonance and rotational digital subtraction angiographies in intracranial aneurysm detection. *Stroke*, 40(9):3127–3129, 2009.

[60] Donald B. Plewes and Walter Kucharczyk. Physics of mri: A primer. *Journal of Magnetic Resonance Imaging*, 35(5):1038–1054, 2012.

[61] Norbert J. Pelc, Matt A. Bernstein, Ann Shimakawa, and Gary H. Glover. Encoding strategies for three-direction phase-contrast mr imaging of flow. *Journal of Magnetic Resonance Imaging*, 1(4):405–413, 1991.

[62] Hojin Ha, Guk Bae Kim, Jihoon Kweon, Sang Joon Lee, Young-Hak Kim, Deok Hee Lee, Dong Hyun Yang, and Namkug Kim. Hemodynamic measurement using four-dimensional phase-contrast mri: quantification of hemodynamic parameters and clinical applications. *Korean journal of radiology*, 17(4):445, 2016.

[63] Zoran Stankovic, Bradley D. Allen, Julio Garcia, Kelly B. Jarvis, and Michael Markl. 4d flow imaging with mri. *Cardiovascular Diagnosis and Therapy*, 4(2), 2014.

[64] S Ansari, S Schnell, P Vakil, M Hurley, B Bendok, H Batjer, T Carroll, J Carr, and M Markl. E-080 4d-flow mri quantifies hemodynamics in large and giant intracranial aneurysms. *Journal of NeuroInterventional Surgery*, 4(Suppl 1):A80–A81, 2012.

[65] S.R. Boddu, F.C. Tong, S. Dehkharghani, J.E. Dion, and A.M. Saindane. Contrast-enhanced time-resolved mra for follow-up of intracranial aneurysms treated with the pipeline embolization device. *American Journal of Neuroradiology*, 35(11):2112–2118, 2014.

[66] Vitor Mendes Pereira, Olivier Brina, Benedicte M A Delattre, Rafik Ouared, Pierre Bouillot, Gorislav Erceg, Karl Schaller, Karl-Olof Lovblad, and Maria-Isabel Vargas. Assessment of intra-aneurysmal flow modification after flow diverter stent placement with four-dimensional flow mri: a feasibility study. *Journal of NeuroInterventional Surgery*, 7(12):913–919, 2015.

[67] Susanne Schnell, Sameer A. Ansari, Can Wu, Julio Garcia, Ian G. Murphy, Ozair A. Rahman, Amir A. Rahsepar, Maria Aristova, Jeremy D. Collins, James C. Carr, and

Michael Markl. Accelerated dual-venc 4d flow mri for neurovascular applications. *Journal of Magnetic Resonance Imaging*, 46(1):102–114, 2017.

[68] Malebogo N. Ngoepe, Alejandro F. Frangi, James V. Byrne, and Yiannis Ventikos. Thrombosis in cerebral aneurysms and the computational modeling thereof: A review. *Frontiers in Physiology*, 9:306, 2018.

[69] Marc Kotowski, Olivier Naggara, Tim E Darsaut, Suzanne Nolet, Guylaine Gevry, Evgueni Kouznetsov, and Jean Raymond. Safety and occlusion rates of surgical treatment of unruptured intracranial aneurysms: a systematic review and meta-analysis of the literature from 1990 to 2011. *Journal of Neurology, Neurosurgery & Psychiatry*, 84(1):42–48, 2013.

[70] David O Wiebers. Unruptured intracranial aneurysms: natural history, clinical outcome, and risks of surgical and endovascular treatment. *The Lancet*, 362(9378):103 – 110, 2003.

[71] Dong H. Kim, Charles L. Haney, and Grace Van Ginhoven. Utility of outcome measures after treatment for intracranial aneurysms. *Stroke*, 36(4):792–796, 2005.

[72] Theodora W. M. Raaymakers, Gabriel J. E. Rinkel, Martien Limburg, and Ale Algra. Mortality and morbidity of surgery for unruptured intracranial aneurysms. *Stroke*, 29(8):1531–1538, 1998.

[73] Amer Alshekhlee, Sonal Mehta, Randall C. Edgell, Nirav Vora, Eli Feen, Afshin Mohammadi, Sushant P. Kale, and Salvador Cruz-Flores. Hospital mortality and complications of electively clipped or coiled unruptured intracranial aneurysm. *Stroke*, 41(7):1471–1476, 2010.

[74] II Barker, Fred G., Sepideh Amin-Hanjani, William E. Butler, Brian L. Hoh, James D. Rabinov, Johnny C. Pryor, Christopher S. Ogilvy, and Bob S. Carter. Age-dependent Differences in Short-term Outcome after Surgical or Endovascular Treatment of Unruptured Intracranial Aneurysms in the United States, 1996–2000. *Neurosurgery*, 54(1):18–30, 01 2004.

[75] Olivier N. Naggara, Phil M. White, François Guilbert, Daniel Roy, Alain Weill, and Jean Raymond. Endovascular treatment of intracranial unruptured aneurysms: Systematic review and meta-analysis of the literature on safety and efficacy. *Radiology*, 256(3):887–897, 2010. PMID: 20634431.

[76] Laurent Pierot, Laurent Spelle, and Fabien Vitry. Immediate clinical outcome of patients harboring unruptured intracranial aneurysms treated by endovascular approach. *Stroke*, 39(9):2497–2504, 2008.

[77] Shewaferaw S Shibeshi and William E Collins. The rheology of blood flow in a branched arterial system. *Applied rheology (Lappersdorf, Germany : Online)*, 15(6):398—405, 2005.

[78] Fernando Mut, Rainald Löhner, Aichi Chien, Satoshi Tateshima, Fernando Viñuela, Christopher Putman, and Juan R. Cebral. Computational hemodynamics framework for the analysis of cerebral aneurysms. *International Journal for Numerical Methods in Biomedical Engineering*, 27(6):822–839, 2011.

[79] Alberto Avolio, Azadeh Farnoush, Michael Morgan, and Yi Qian. Hemodynamic models of cerebral aneurysms for assessment of effect of vessel geometry on risk of rupture. *Annual International Conference of the IEEE Engineering in Medicine and Biology Society. IEEE Engineering in Medicine and Biology Society. Annual International Conference*, 2009:2351—2353, 2009.

[80] A Chien, MA Castro, S Tateshima, J Sayre, J Cebral, and F Viñuela. Quantitative hemodynamic analysis of brain aneurysms at different locations. *AJNR. American journal of neuroradiology*, 30(8):1507—1512, September 2009.

[81] Brittany Staarmann, Matthew Smith, and Charles J Prestigiacomo. Shear stress and aneurysms: a review. *Neurosurgical focus*, 47(1):E2, 2019.

[82] Tamer Hassan, Eugene V. Timofeev, Tsutomu Saito, Hiroaki Shimizu, Masayuki Ezura, Yasushi Matsumoto, Kazuyoshi Takayama, Teiji Tominaga, and Akira Takahashi. A proposed parent vessel geometry—based categorization of saccular intracranial aneurysms: computational flow dynamics analysis of the risk factors for lesion rupture. *Journal of Neurosurgery*, 103(4):662 – 680, 01 Jan. 2005.

[83] Keiji Fukazawa, Fujimaro Ishida, Yasuyuki Umeda, Yoichi Miura, Shinichi Shimosaka, Satoshi Matsushima, Waro Taki, and Hidenori Suzuki. Using computational fluid dynamics analysis to characterize local hemodynamic features of middle cerebral artery aneurysm rupture points. *World Neurosurgery*, 83(1):80 – 86, 2015.

[84] Kenichi Kono, Takeshi Fujimoto, Aki Shintani, and Tomoaki Terada. Hemodynamic Characteristics at the Rupture Site of Cerebral Aneurysms: A Case Study. *Neurosurgery*, 71(6):E1202–E1209, 08 2012.

[85] Ying Zhang, Linkai Jing, Jian Liu, Chuanhui Li, Jixing Fan, Shengzhang Wang, Haiyun Li, and Xinjian Yang. Clinical, morphological, and hemodynamic independent characteristic factors for rupture of posterior communicating artery aneurysms. *Journal of NeuroInterventional Surgery*, 8(8):808–812, 2016.

[86] Tomoaki Suzuki, Hiroyuki Takao, Takashi Suzuki, Yukinao Kambayashi, Mitsuyoshi Watanabe, Hiroki Sakamoto, Issei Kan, Kengo Nishimura, Shogo Kaku, Toshihiro Ishibashi, Satoshi Ikeuchi, Makoto Yamamoto, Yukihiko Fujii, and Yuichi Murayama. Determining the Presence of Thin-Walled Regions at High-Pressure Areas in Unruptured Cerebral Aneurysms by Using Computational Fluid Dynamics. *Neurosurgery*, 79(4):589–595, 10 2016.

[87] Tomoaki Suzuki, Hiroyuki Takao, Takashi Suzuki, Yukinao Kambayashi, Mitsuyoshi Watanabe, Hiroki Sakamoto, Issei Kan, Kengo Nishimura, Shogo Kaku, Toshihiro Ishibashi, Satoshi Ikeuchi, Makoto Yamamoto, Yukihiko Fujii, and Yuichi Murayama. Determining the Presence of Thin-Walled Regions at High-Pressure Areas in Unruptured Cerebral Aneurysms by Using Computational Fluid Dynamics. *Neurosurgery*, 79(4):589–595, 10 2016.

[88] Christian Doenitz, Karl-Michael Schebesch, Roland Zoephel, and Alexander Brawanski. A Mechanism for the Rapid Development of Intracranial Aneurysms: A Case Study. *Neurosurgery*, 67(5):1213–1221, 11 2010.

[89] Ireneusz Zbicinski, Natalia Veshkina, and Ludomir Stefańczyk. 4d model of hemodynamics in the abdominal aorta. *Bio-medical materials and engineering*, 26 Suppl 1:S257—64, 2015.

[90] Haruo Isoda, Yasuhide Ohkura, Takashi Kosugi, Masaya Hirano, Marcus T Alley, Roland Bammer, Norbert J Pelc, Hiroki Namba, and Harumi Sakahara. Comparison of hemodynamics of intracranial aneurysms between mr fluid dynamics using 3d cine phase-contrast mri and mr-based computational fluid dynamics. *Neuroradiology*, 52(10):913—920, October 2010.

[91] Loic Boussel, Vitaliy Rayz, Alastair Martin, Gabriel Acevedo-Bolton, Michael T. Lawton, Randall Higashida, Wade S. Smith, William L. Young, and David Saloner. Phase-contrast magnetic resonance imaging measurements in intracranial aneurysms in vivo of flow patterns, velocity fields, and wall shear stress: Comparison with computational fluid dynamics. *Magnetic Resonance in Medicine*, 61(2):409–417, 2009.

[92] Youmin Tang, Zheqi Shen, and Yanqiu Gao. *An introduction to ensemble-based data assimilation method in the Earth sciences.* InTech Oregon, 2016.

[93] Marta D'Elia, Lucia Mirabella, Tiziano Passerini, Mauro Perego, Marina Piccinelli, Christian Vergara, and Alessandro Veneziani. *Applications of variational data assimilation in computational hemodynamics*, pages 363–394. Springer Milan, Milano, 2012.

[94] Franziska Schulz, Christoph Roloff, Daniel Stucht, D. Thévenin, Oliver Speck, and Gábor Janiga. Improved flow prediction in intracranial aneurysms using data assimilation. pages 629–639, 01 2019.

[95] Franziska Gaidzik, Daniel Stucht, Christoph Roloff, Oliver Speck, Dominique Thévenin, and Gábor Janiga. Transient flow prediction in an idealized aneurysm geometry using data assimilation. *Computers in Biology and Medicine*, 115:103507, 2019.

[96] Ali Bakhshinejad, V Rayz, and Roshan M D'Souza. Reconstructing blood velocity profiles from noisy 4d-pcmr data using ensemble kalman filtering.

[97] Marta D'Elia and Alessandro Veneziani. Uncertainty quantification for data assimilation in a steady incompressible navier-stokes problem. *ESAIM: Mathematical Modelling and Numerical Analysis*, 47(4):1037–1057, 2013.

[98] Adam Updegrove, Nathan Wilson, Jameson Merkow, Hongzhi Lan, Alison Marsden, and Shawn Shadden. Simvascular: An open source pipeline for cardiovascular simulation. *Annals of Biomedical Engineering*, 45, 12 2016.

[99] Simona Hodis, Susheil Uthamaraj, Andrea L. Smith, Kendall D. Dennis, David F. Kallmes, and Dan Dragomir-Daescu. Grid convergence errors in hemodynamic solution of patient-specific cerebral aneurysms. *Journal of Biomechanics*, 45(16):2907 – 2913, 2012.

[100] Brent A. Craven, Eric G. Paterson, and Gary S. Settles. The fluid dynamics of canine olfaction: unique nasal airflow patterns as an explanation of macrosmia. *Journal of The Royal Society Interface*, 7(47):933–943, 2010.

[101] Philippe Reymond, Fabrice Merenda, Fabienne Perren, Daniel Rufenacht, and Nikos Stergiopulos. Validation of a one-dimensional model of the systemic arterial tree. *American Journal of Physiology-Heart and Circulatory Physiology*, 297(1):H208–H222, 2009.

[102] Nan Xiao, Jay D Humphrey, and C Alberto Figueroa. Multi-scale computational model of three-dimensional hemodynamics within a deformable full-body arterial network. *Journal of computational physics*, 244:22–40, 2013.

[103] A Ch Simon, ME Safar, JA Levenson, GM London, BI Levy, and NPh Chau. An evaluation of large arteries compliance in man. *American Journal of Physiology-Heart and Circulatory Physiology*, 237(5):H550–H554, 1979.

[104] Christian H Whiting and Kenneth E Jansen. A stabilized finite element method for the incompressible navier–stokes equations using a hierarchical basis. *International Journal for Numerical Methods in Fluids*, 35(1):93–116, 2001.

[105] Martin S Alnæs, Anders Logg, Kristian B Ølgaard, Marie E Rognes, and Garth N Wells. Unified form language: A domain-specific language for weak formulations of partial differential equations. *ACM Transactions on Mathematical Software (TOMS)*, 40(2):1–37, 2014.

[106] Michael Hinze, René Pinnau, Michael Ulbrich, and Stefan Ulbrich. *Optimization with PDE constraints*, volume 23. Springer Science & Business Media, 2008.

[107] Fredi Tröltzsch. *Optimal control of partial differential equations: theory, methods, and applications*, volume 112. American Mathematical Soc., 2010.

[108] Andrew M Bradley. Pde-constrained optimization and the adjoint method. 2019. *URL https://cs. stanford. edu/˜ ambrad/adjoint_ tutorial. pdf.*

[109] Jorge Nocedal and Stephen Wright. *Numerical optimization.* Springer Science & Business Media, 2006.

[110] L-D Jou, Deok Hee Lee, Hesham Morsi, and Michel E Mawad. Wall shear stress on ruptured and unruptured intracranial aneurysms at the internal carotid artery. *American Journal of Neuroradiology*, 29(9):1761–1767, 2008.

List of Figures

List of Tables